AN EXACT AND CONSISTENT ADJOINT METHOD FOR HIGH-FIDELITY DISCRETIZATION OF THE COMPRESSIBLE FLOW EQUATIONS

BY

RAMANATHAN VISHNAMPET GANAPATHI SUBRAMANIAN

DISSERTATION

Submitted in partial fulfillment of the requirements
for the degree of Doctor of Philosophy in Theoretical and Applied Mechanics
in the Graduate College of the
University of Illinois at Urbana-Champaign, 2015

Urbana, Illinois

Doctoral Committee:

Professor Jonathan B. Freund, Chair and Director of Research
Associate Professor Daniel J. Bodony, Co-Chair and Co-Director of Research
Associate Professor Luke Olson
Assistant Professor Andreas Klöckner

Abstract

Methods and computing hardware advances have enabled accurate predictions of complex compressible turbulence phenomena, such as the generation of jet noise that motivates the present effort. However, limited understanding of underlying physical mechanisms restricts the utility of such predictions since they do not, by themselves, indicate a route to design improvement. Gradient-based optimization using adjoints can circumvent the flow complexity to guide designs. Such methods have enabled sensitivity analysis and active control of turbulence at engineering flow conditions by providing gradient information at computational cost comparable to that of simulating the flow. They accelerate convergence of numerical design optimization algorithms, though this is predicated on the availability of an accurate gradient of the discretized flow equations. This is challenging to obtain, since both the chaotic character of the turbulence and the typical use of discretizations near their resolution limits in order to efficiently represent its smaller scales will amplify any approximation errors made in the adjoint formulation. Formulating a practical *exact* adjoint that avoids such errors is especially challenging if it is to be compatible with state-of-the-art simulation methods used for the turbulent flow itself. Automatic differentiation (AD) can provide code to calculate a nominally exact adjoint, but existing general-purpose AD codes are inefficient to the point of being prohibitive for large-scale turbulence simulations.

We analyze the compressible flow equations as discretized using the same high-order workhorse methods used for many high-fidelity compressible turbulence simulations, and formulate a practical space–time discrete-adjoint method without changing the basic discretization. A key step is the definition of a particular discrete analog of the continuous norm that defines our cost functional; our selection leads directly to an efficient Runge–Kutta-like scheme, with finite-difference spatial operators for the adjoint system. Its computational cost only modestly exceeds that of the flow equations. We confirm that its accuracy is limited only by computing precision, and we demonstrate it on the aeroacoustic control of a mixing layer with a challengingly broad range of turbulence scales. For comparison, the error from a corresponding discretization of the continuous-adjoint equations is quantified to potentially explain its limited success in past efforts to control jet noise. The differences are illuminating: the continuous-adjoint is shown to suffer from exponential

error growth in (reverse) time even for the best-resolved largest turbulence scales.

Though the gradient from our *fully* discrete adjoint is formally exact, it does include sensitivity to numerical solutions that are only an artifact of the discretization. These are typically saw-tooth type features, such as seen in under-resolved numerical simulations. Since these have no physical analog, for physical analysis or design of realistic actuators, such solutions are in a sense spurious. This has been addressed without sacrificing accuracy by redesigning the basic discretization to be dual-consistent, for which the discrete-adjoint is consistent with the adjoint of the continuous system, and thus, free from spurious numerical sensitivity modes. We extend our exact discrete-adjoint to a spatially dual-consistent discretization of the compressible flow equations and demonstrate its practical application for aeroacoustic control of a Mach 1.3 turbulent jet. The formulation admits a broad class of finite-difference schemes that satisfy a summation by-parts rule, and extends to multi-block curvilinear grids for efficient handling of complex geometries. The formulation is developed for several boundary conditions commonly used in simulation of free-shear and wall-bounded flows. In addition, the proposed discretization leads to superconvergent approximations of functionals, and can be tailored to achieve global conservation up to arbitrary orders of accuracy. We again confirm that the sensitivity gradient for turbulent jet noise computed using our dual-consistent method is only limited by computing precision.

Acknowledgements

Contents

List of Abbreviations

AD   Automatic Differentiation

CFD   Computational Fluid Dynamics

CFL   Courant–Friedrichs–Lewy

dB   Decibels

DNS   Direct Numerical Simulation

FWH   Ffowcs–Williams–Hawkings

IBVP   Initial Boundary Value Problem

LES   Large-Eddy Simulation

LODI   Locally One-Dimensional Inviscid

ODE   Ordinary Differential Equation

PDE   Partial Differential Equation

RANS   Reynolds-Averaged Navier–Stokes

RHS   Right-Hand-Side

RK4   Fourth-order Runge–Kutta

SAT   Simultaneous Approximation Term

SBP   Summation-By-Parts

SPL   Sound Pressure Level

SST   Shear-Stress Transport

List of Symbols

Greek Symbols

α — Scalar factor that multiplies the control forcing, determined for maximum reduction in cost functional along a particular search direction

$\alpha_{\min}$ — The value of α that minimizes the cost functional along a particular search direction, see (2.4)

$\beta^{n,s}$ — Coefficients of a quadrature scheme in time used to define the inner product of fully discrete vectors, see (3.17)

γ — Ratio of specific heats, which we assume constant ($\gamma = 1.4$) in this study

Γ — Control region, or the support of W_Γ, where the control forcing is applied

δ_{ij} — Kronecker delta symbol, in Einstein notation, see (2.8)

$\mathbf{\Delta}_i^\pm$ — An $N^3 \times N^3$ diagonal matrix, whose only non-zero entries on the diagonal correspond to the grid points on the $B_i^\pm$ boundary surface (for a semidiscrete vector $\vec{f} = \text{proj}\,[f\,(\boldsymbol{\xi})]$, the sum of the elements of $\mathbf{\Delta}_i^\pm \vec{f}$ is a consistent approximation of the surface integral of $f\,(\boldsymbol{\xi})$ on $B_i^\pm$), see (3.5)

ϵ — Machine epsilon, represents the precision of floating-point arithmetic, see (2.23)

ϵ_{ijk} — Levi-Civita symbol, in Einstein notation, see (2.3)

κ — Thermal conductivity

λ — Second coefficient of viscosity

μ — Dynamic viscosity

μ_B — Bulk viscosity, which we assume to be 0.6μ in this study

ξ_i — Computational coordinate vector, in Einstein notation, see Figure 2.1

Ξ_i — Mapping function that transforms the physical coordinate vector $\mathbf{x}$ to the computational coordinate ξ_i, see Figure 2.1

ρ — Density

σ — Non-negative scalar factor that multiplies an SAT, determined from stability and dual-consistency requirements, see (5.5), (5.9), (5.16) and (5.21)

$\sigma_{\text{diss.}}$ — Non-negative scalar factor that multiplies the artificial dissipation term added to the semi-discrete form of the governing equations, and controls the amount of dissipation, see (3.7)

σ_{sponge}	Non-negative scalar factor that multiplies the damping term, see (5.7)
τ_{ij}	Stress tensor, in Einstein notation
ω_i	Vorticity vector, in Einstein notation, see (4.1)
Ω	Target region, or the support of W_Ω, where the objective functional is measured

Roman Symbols

a	Speed of sound
$\mathbf{A}_i$	Semi-discrete form of $\mathcal{A}_i$
$\mathcal{A}_i$	Operator that yields the first partial Jacobian of the Cartesian form of fluxes along the x_i-direction with respect to a vector of state variables on which it acts, see (2.13) and (A.4)
$B_i^\pm$	One of the six boundary faces of the unit cube computational domain $\mathbb{D} = (0,1)^3$, whose outward normal is along the $\pm\xi_i$-direction, see (2.4)
$\mathbf{B}_{ij}$	Semi-discrete form of $\mathcal{B}_{ij}$
$\mathcal{B}_{ij}$	Operator that yields the first partial Jacobian of the Cartesian form of fluxes along the x_i-direction with respect to the first partial derivative along the ξ_j-direction of a vector of state variables on which it acts, see (2.13) and (A.4)
C^0	Set of all continuous functions
C_p	Specific heat at constant pressure
C_v	Specific heat at constant volume
$\mathbf{C}$	Semi-discrete form of $\mathcal{C}$
$\mathcal{C}$	Operator that yields the first partial Jacobian of the primitive variables corresponding to the vector of state variables on which it acts, see (2.13) and (A.4)
D	Nozzle diameter
$\hat{D}$	An $N \times N$ banded matrix whose elements correspond to the coefficients of a first-derivative approximation, see (3.2)
$\hat{\mathbf{D}}_i$	Discrete operator that approximates a partial first-derivative with respect to the ξ_i-direction (in three dimensions, a block-banded $N^3 \times N^3$ matrix, where N^3 is the number of points in the computational grid), see (3.2)
$\hat{\mathbf{D}}_i^{(s)}$	A minimal stencil-width discrete approximation of a partial first-derivative with respect to the ξ_i-direction [54]
$\widehat{\mathbf{DI}}_i$	Discrete dissipation operator for the ξ_i-direction, see (3.7)
$\mathbb{D}$	Computational domain, which we assume to be the open unit cube $(0,1)^3$ for a single-block problem
$\mathbb{D}_p$	Physical domain
$\partial\mathbb{D}$	Boundary of the computational domain

$\partial\mathbb{D}_p$	Boundary of the physical domain
$\overline{\mathbb{D}}$	Closure of the computational domain, which we assume to be the closed unit cube $[0,1]^3$ for a single-block problem
$\overline{\mathbb{D}}_p$	Closure of the physical domain
E	Specific energy (the sum of kinetic energy and specific enthalpy)
$E_i^{\pm}$	An $N_i \times N_i$ matrix with a single non-zero entry 1 at the $(1,1)$ position for E_i^- or the (N_i, N_i) position for E_i^+
$\mathcal{E}$	Gradient error, see (2.22)
f	Vector of space–time functions that force the right-hand-side of the compressible flow equations (unless noted otherwise), which we assume to be a model for a plasma actuator in this study, see (2.17)
F	Cartesian form of the vector of fluxes corresponding to the conserved variables, see (2.7)
$\mathcal{F}$	Operator that acts on a vector of state variables and yields the corresponding fluxes, see (2.11)
F	Semi-discrete form of $\mathcal{F}$, see (3.12)
$\vec{g}_\Omega$	A semi-discrete vector, defined such that $-\vec{W}_\Omega \circ \vec{g}_\Omega = \frac{\delta \mathsf{J}}{\delta \vec{Q}}$ (appears as a target forcing term on the right-hand-side of the adjoint compressible flow equations), see (4.14)
$\mathcal{G}$	Operator that acts on a vector of adjoint variables and yields the corresponding gradient of the objective functional, see (4.10)
$\tilde{\mathsf{G}}$	Fully discrete form of $\mathcal{G}$
h	Specific enthalpy, $h = E + p/\rho$
H	Heavyside function
H^k	For k non-negative, the space of all L^2-functions whose weak derivatives up to order k are also L^2-functions
I_m	For m a positive integer, the $m \times m$ identity matrix
J	Jacobian of the transformation from physical coordinates to computational coordinates, see (2.1)
$\hat{\mathbf{J}}$	A diagonal matrix whose diagonal elements are the semi-discrete approximations of the Jacobian J at the grid points
$\mathcal{J}$	Operator that acts on a vector of state variables and yields the value of the objective functional, or cost functional, see (2.14)
J	Semi-discrete form of $\mathcal{J}$
k	Wavenumber, see Figure 3.1
k^*	Modified wavenumber, see Figure 3.1
$\hat{\mathbf{k}}$	Unit vector that identifies the direction along which the force exerted by the fluid on a solid body is measured, used to quantify drag/lift forces, see (2.16)
$\mathcal{K}_V$	Operator that acts on a vector of state variables and yields the integrand in the volume contribution to the objective functional, see (2.14)

$\mathcal{K}_S$	Operator that acts on a vector of state variables and yields the integrand in the surface contribution to the objective functional, see (2.14)
K_V, K_S	Semi-discrete forms of $\mathcal{K}_V$ and $\mathcal{K}_S$, respectively
$L^\star$	Dimensional reference length used for non-dimensionalization
$\mathcal{L}$	The operator Lagrangian for the constrained optimization problem for $\mathcal{J}[Q]$ subject to the constraint $\mathcal{M}[Q, f] = 0$
M_{ij}	Normalized metric tensor, in Einstein notation, see (2.2)
$\hat{\mathrm{M}}_{ij}$	Unit normal vector to the $B_i^\pm$ surface, in Einstein notation (with j dummy index)
$\tilde{\mathrm{M}}_i$	Area of a surface element on $B_i^\pm$
$\tilde{\mathbf{M}}_i$	A diagonal matrix whose diagonal elements are the semi-discrete approximations of $\tilde{\mathrm{M}}_i$ at the grid points
$\mathbf{M}_{ij}$	A diagonal matrix whose diagonal elements are the semi-discrete approximations of M_{ij} at the grid points
$\mathcal{M}$	Operator that acts on a vector of state variables and a vector of space–time control functions, and yields the value of the corresponding residual of the forced compressible flow equations, see (2.19)
M, $\tilde{\mathsf{M}}$	Semi-discrete and fully discrete forms of $\mathcal{M}$, respectively, see (3.15) and (3.18)
n	Exponent of temperature in the power law for viscosity, which we assume to be constant ($n = 0.666$) in this study, see (2.9)
N_c	Interval at which the vector of state variables are stored in disk, and retrieved when solving the adjoint equations, see Section 4.5
N_i	Number of grid points along the ξ_i-direction for a single-block problem (to demonstrate some theoretical results, we assume $N_1 = N_2 = N_3 = N$ for simplicity of formulation)
N_t	Number of timesteps
$\mathbb{N}$	Set of natural numbers
$\mathcal{N}$	Operator that acts on a vector of state variables and yields the corresponding residual of the unforced compressible flow equations, see (2.19)
$\tilde{\mathsf{N}}$	Fully discrete form of $\mathcal{N}$, see (3.18)
p	Static pressure
$\bar{p}$	Mean pressure about which acoustic pressure fluctuations are computed, see (2.15)
$\hat{P}$	The norm matrix corresponding to an SBP scheme, or an $N \times N$ symmetric positive-definite matrix, whose elements correpond to the coefficients of a quadrature rule, see (3.3)
$\hat{\mathbf{P}}$	A symmetric positive-definite matrix that defines an inner product in V_h, which we assume to be a diagonal matrix in this study, see (3.1)
Pr	Prandtl number, see (2.8)
q_i	Heat flux vector, in Einstein notation
Q	Vector of conserved state variables

$Q^\dagger$ Vector of adjoint variables, with components in three dimensions, denoted $\begin{bmatrix} Q_1^\dagger & Q_2^\dagger & Q_3^\dagger & Q_4^\dagger & Q_5^\dagger \end{bmatrix}^{\mathrm{T}}$, see Definition 4.1

$\vec{Q}^0$ Semi-discrete approximation of the conserved variables at $t = t_0$

R Specific gas constant, $R = C_p - C_v$

$\mathbb{R}$ Set of real numbers

$\mathbb{R}_0^+$ Set of non-negative real numbers

$\mathcal{R}$ Operator that acts on a vector of state variables and yields the corresponding right-hand-side of the unforced compressible flow equations, see (2.11)

$\mathcal{R}^\dagger$ Operator that acts on a vector of state variables and a vector of adjoint variables and yields the negative right-hand-side of the adjoint compressible flow equations, specific to the choice of objective functional $\mathcal{J}[Q]$, see Definition 4.1

$\vec{\mathsf{R}}$ Semi-discrete form of $\mathcal{R}$, see (3.12)

$\vec{\mathsf{R}}_{\mathrm{SAT}}$ SATs added to the RHS of the semi-discrete form of the governing equations to weakly enforce boundary conditions, see (3.13)

$\vec{\mathsf{R}}_{\mathrm{SAT},i}^\pm$ The SAT corresponding to the boundary surface $B_i^\pm$, see (3.13)

Re   Reynolds number, see (2.8)

S State space (formally, in three dimensions, the space of all quintuples whose elements are L^2-functions over the field of non-negative reals (time) and the open unit cube (space), such that their weak partial first-derivative with respect to time and weak partial second-derivatives with respect to space exist in L^2).

$\mathbf{S}$ Transpose of the Fréchet derivative of $\vec{\mathsf{R}}\left[\vec{Q}\right]$ with respect to $\vec{Q}$

$\mathbf{S}_{\mathrm{SAT},i}^\pm$ Fréchet derivative of $\vec{\mathsf{R}}_{\mathrm{SAT},i}^\pm\left[\vec{Q}\right]$ with respect to $\vec{Q}$, where $\mathbf{J}\mathbf{P}^{-1}\vec{\mathsf{R}}_{\mathrm{SAT},i}^\pm\left[\vec{Q}\right]$ is the SAT that enforces the boundary condition for $\boldsymbol{\xi} \in B_i^\pm$

t Time

Δt Constant time step size used to integrate the semi-discrete form of the governing equations in time

t_0 Beginning of the control time horizon, see (2.17)

t_1 End of the control time horizon, see (2.17)

T Static temperature

u_i Primitive velocity, in Einstein notation

$\hat{u}_i$ Component of primitive velocity along the outward normal to the surface $B_i^\pm$

U Subspace of S whose elements satisfy the linearized boundary conditions

U_j Jet velocity at nozzle-exit

V Space of all L^2-functions over the space–time field

V_h Space of all semi-discrete vectors, or the N^3-th Cartesian power of the space of all L^2-functions over the field of non-negative reals (time), where N^3 is the number of points in the computational grid

W_Γ	In three dimensions, a quintuple whose elements correspond to the space–time mollifying support functions that provide compact support over a control region (in space), and a control horizon (in time), for the control forcing term in the governing equations, see (2.17)
W_Ω	Scalar-valued space–time mollifying support function that provides compact support over a target region (in space), and a control horizon (in time), for the volume contribution to the objective functional, see (2.14)
$W_{\Omega'}$	Scalar-valued space–time mollifying support function that provides compact support over a target region (in space), and a control horizon (in time), for the surface contribution to the objective functional, see (2.14)
x_i	Physical coordinate vector, in Einstein notation, see Figure 2.1
X_i	Mapping function that transforms the computational coordinate vector $\boldsymbol{\xi}$ to the physical coordinate x_i, see Figure 2.1
$\tilde{x}_i^\perp$	Distance from the boundary $B_i^\pm$ to a grid point located in a sponge zone adjacent to it, measured along the curve perpendicular to the isosurfaces of ξ_i and normalized so that $0 \le \tilde{x}_i^\perp \le 1$ across the sponge layer, see (5.7)
$\vec{Y}$	Penalty vector operator used in the construction of an SAT for enforcing the impermeable wall and isothermal wall boundary conditions, see (5.9) and (5.16)

Subscripts and Superscripts

$\star$	Dimensional quantity
∞	Reference state, usually the ambient state
b	Conserved state or adjoint variable that satisfies the corresponding boundary conditions on $\boldsymbol{\xi} \in \partial\mathbb{D}$ (but may not necessarily solve the corresdponding PDE)
int.	Interface condition (e.g., $\vec{Q}^{\text{int.}}$ denotes the semi-discrete vector of conserved state variables at which the eigenvalues of the first partial Jacobian of the inviscid fluxes with respect to it are evaluated, or the Roe-average of the "left" and "right" states), see (5.21)
I	Inviscid contribution
j	Nozzle-exit condition
L	"Left" computational block in a multi-block grid consisting of two non-overlapping blocks, see Figure 5.1
n, s	For n positive integer and $s = 1, 2, 3, 4$ for the RK4 scheme, the approximation of a semi-discrete vector at time $t = t^n + c_s \Delta t$, where $c_1 = c_2 = 1/2$ and $c_3 = c_4 = 1$
R	"Right" computational block in a multi-block grid consisting of two non-overlapping blocks, see Figure 5.1
t	Target solution that supplies boundary data for inflow/outflow boundaries
V	Viscous contribution
w	Wall condition

Mathematical Symbols

∘   Elementwise multiplication, or Hadamard product

⊗   Kronecker product

δ Differential, or first variation operator (identical to the Fréchet derivative in this study which only considers Banach spaces), see (2.12)

diag   Operator that yields a diagonal matrix whose diagonal is the vector on which it acts

dom   Domain of an operator

proj   Operator that acts on a continuous function of space and yields a semi-discrete vector whose elements represent the semi-discrete approximation of the function at the corresponding grid points

Chapter 1

Introduction

Predictive numerical simulations compute a quantity of interest, say a functional that depends on the flow solution, but do not by themselves provide any sensitivity information. Control parameters or design variables that influence the quantity of interest do so through the equations governing the flow. If there are more than a handful of independent parameters, the brute-force one-at-a-time approach to sensitivity analysis based on repeated predictions becomes prohibitively computationally expensive. Adjoint-based methods provide the sensitivity gradient of a functional with respect to an arbitrarily large number of control parameters, incurring only marginally more computational cost than a single predictive simulation [33]. Their applications in computational fluid dynamics include optimal flow control [6, 90, 37], aerodynamic shape design [33, 51], adaptive grid refinement [3], uncertainty quantification [48, 86], history matching [47], and stability and global mode analysis [32, 49, 18]. Our specific efforts are directed towards control optimization of turbulent aeroacoustic flows, and our demonstration simulations are motivated by this application, which we discuss in some detail.

The control of sound generation by turbulence provides a particularly challenging target application due to its complexity and the relative subtlety of its noise-generation mechanisms. In aeroacoustic simulations, the computational challenge of representing a range of turbulence scales simultaneously with relatively low-amplitude fluctuations is well documented [15, 85]. Without a reduced model of noise generation mechanisms to provide guidance, predictions by themselves do not indicate routes to design improvement. Adjoint-based optimization methods used in conjunction with predictive simulations have been proposed and demonstrated to circumvent this complexity by providing gradient information that can be harnessed to achieve noise reductions [23]. In essence, the adjoint carries sensitivity information with respect to an arbitrarily large number of control parameters, which enables the optimization of noise-controlling actuation or geometries. Building on efforts in aerodynamic optimization [33] and incompressible turbulence control [6], Wei and Freund [90] achieved 11 dB noise reduction of far-field sound of a direct numerical simulation (DNS) of a two-dimensional compressible shear layer with control applied near a nominal splitter plate.

1.1 Comparison of Adjoint Methods

In the continuous-adjoint approach, the adjoint equations are derived using the extended Green's identity after linearizing the partial differential equations (PDEs) and boundary conditions [43]. The flow and adjoint equations are then *independently* discretized with no guarantee that the duality relationship continues to hold for their discrete counterparts [2]. This duality condition is mathematically defined in Definition 5.1. The incompatibility can degrade the accuracy of the sensitivity gradient, which has been extensively analyzed [83]. In the discrete-adjoint approach, the linearized PDEs and boundary conditions are first *discretized* and then linearized, such that they are formally representable as a matrix. The discrete-adjoint equations are obtained from the conjugate transpose of this matrix. A practical method that does not necessitate storing this matrix explicitly ensues from the fact that its sparsity structure for the particular discretization employed is known beforehand. Thus, the discrete-adjoint approach is tied to a particular discretization of the PDE, boundary conditions and functional, but provides the *exact* sensitivity of the discrete functional up to floating-point induced roundoff errors.

Though the continuous-adjoint approach has been used extensively for optimal flow control, it has not been so remarkably successful for turbulent flows. For aeroacoustic control of a DNS turbulent mixing layer, Vishnampet et al. [83] observed $2.2\times$ more reduction using a space–time discrete-adjoint method compared to the continuous-adjoint approach. When a non-local turbulence model is employed, approximation errors in discretizing the true continuous-adjoint system further deteriorates its usefulness in providing an accurate sensitivity gradient. Using an approximate adjoint based on the unfiltered continuous PDE, Kim et al. [37] reduced the noise from a Mach 1.3 large-eddy simulation (LES) turbulent jet by 3.5 dB, a relatively modest amount given the flexibility of their actuation. It is not possible in this case to decouple the limits of control from numerical imprecision. Similarly, with an SST k-ω turbulence model, Carnarius et al. [13] showed that the continuous-adjoint based gradient leads to a 10% over-prediction of the minimum drag coefficient for flow over a rotating cylinder.

For the chaotic Lorenz system, Lea et al. [44] showed that the adjoint-based gradient suffers from cumulative growth when the cost functional is a time-averaged quantity over an interval longer than the predictability time scales of the system. This is expected to be an important factor for the turbulent flow we consider, both because turbulence is chaotic and because efficient simulations usually employ resolutions close to the limits of the discretization. Thus, the resulting truncation errors will thus be relatively large to start with, even before they amplify via the chaotic character of the system. In such situations, the discrete-adjoint method is expected to significantly accelerate and improve optimization. Developing a practical discrete-adjoint method, in the sense that it does not require operation counts or memory much

beyond direct discretization of the continuous-adjoint, and demonstrating it on a challenging large-scale turbulent flow simulation are our goals. An inherent limitation of conventional continuous- and discrete-adjoint based formulations is their inability to overcome the chaos of turbulence indefinitely. Fortunately, they can be useful for finite-time-horizon control, and means of reformulating the overall problem to overcome this limitation is a subject of ongoing investigation [86].

Despite the relative success of the discrete-adjoint approach for minimization problems, it is not the natural choice in applications such as functional error estimation, which require the adjoint solution to be well-behaved and non-oscillatory [57]. In general, the discrete-adjoint equation admits solutions with spurious numerical waves corresponding to the highest wavenumber supported by the grid, which have been attributed to the sensitivity corresponding to computational modes supported by the discretization of the flow equations [72]. Further, these spurious waves are retained in the sensitivity gradient in optimization problems, and consequently affect the optimal actuator forcing suggested by the discrete-adjoint approach, making it an impractical tool for designing real actuators.

1.2 Dual Consistency

The limitations of the continuous- and discrete-adjoint approaches can be overcome, and their advantages simultaneously leveraged, by using a dual-consistent discretization of the flow equations. A dual-consistent discretization is one for which the discrete-adjoint equations are also a consistent approximation of the continuous-adjoint equations. The importance of dual-consistency seems to have first been analyzed by Harriman et al. [27] in conjunction with optimal convergence rates of linear functionals using the discontinuous Galerkin finite-element method. It was later extended to a class of finite-difference discretizations using operators that satisfy a summation-by-parts (SBP) rule in conjunction with weakly enforced boundary conditions using simultaneous approximation terms (SATs) [29].

There is an extensive body of literature on SBP–SAT schemes [41, 75, 53, 77, 34, 19, 79, 78, 59], which are attractive mainly because they lead to accurate and provably stable discretizations. Thus, the selection of SATs for enforcing specific boundary conditions is based on consistency and stability. While consistency is easily demonstrated, stability requires the existence of an energy estimate for the combined semi-discrete problem. An equivalence class of consistent and stable SATs have been proposed for various physical boundary conditions, including subsonic/supersonic inflows and outflows [79], and isothermal and adiabatic no-slip walls [78], as well as for enforcing conservation conditions at a non-physical C^0-boundary between multiple adjoining blocks in semi-structured grids commonly employed for discretizing complex geometries. Here, we

discuss a third important criteria — dual-consistency, which requires that the adjoint of the semi-discrete problem including the SAT be consistent with the continuous-adjoint boundary conditions. Specifically, we address whether there exist dual-consistent SATs within the set of consistent and stable SATs. For example, Svärd et al. [79] constructed an SAT for enforcing an inflow/outflow condition with two free parameters σ^I and σ^V, and derived the stability condition: $\sigma^I \geq \frac{1}{2}$ and $\sigma^V = 1$. In the inviscid limit, Hicken and Zingg [29] showed that for $\sigma^I = 1$, the SAT also becomes dual-consistent.

When used in conjunction with SBP schemes, dual-consistent SATs lead to a dual-consistent spatial discretization of the flow equations, which have two important consequences. First, their discrete-adjoint is free from spurious numerical sensitivities and are high-order accurate solutions of the continuous-adjoint equations. Second, they lead to superconvergent functionals [29]. This is an attractive property for a finite-difference discretization since it guarantees approximate global conservation up to the order of accuracy of the interior scheme.

1.3   Accomplishments

This section summarizes the two principal contributions of this dissertation. A key feature of both is their application to turbulence simulation, and include as examples DNS of a mixing layer and high-fidelity LES of a Mach 1.3 turbulent jet, respectively.

1.3.1   Practical space–time exact adjoint formulation

We formulate an exact space–time adjoint formulation that is practical in that it incurs a computational cost comparable to the flow equations or a direct discretization of the continuous-adjoint. Our formulation is compatible with the same high-order finite-difference schemes that are the "workhorse" methods for a wide range of compressible flow simulations, including turbulent free-shear flows [24, 62, 39], boundary layer flows [92], and combustion [28]. These schemes are not locally conservative, but are attractive and effective for the class of flows we consider, particularly because of their resolution. We show that an exact adjoint is surprisingly important for accurately predicting the sensitivity at all turbulence scales, and that our formulation is computationally efficient and extensible. To do this, we make some key advances that facilitate implementation for such discretizations. This is an important step beyond the algorithms that have been developed to do this for aerodynamic simulations.

For example, Rumpfkeil and Zingg [68] derived the discrete-adjoint equation for unsteady flows governed by the Euler equations integrated using implicit Euler and second-order backward difference (BDF2) meth-

ods; Yamaleev et al. [91] formulated a discrete-adjoint method for optimization using the three-dimensional Reynolds-averaged Navier–Stokes (RANS) equations on dynamic unstructured grids; Wang et al. [84] derived the discrete-adjoint equation for the two-dimensional compressible Euler equations with high-order discontinuous Galerkin discretization and an implicit fourth-order Runge–Kutta scheme; Roth and Ulbrich [67] developed a discrete-adjoint approach based on the sparse forward mode of automatic differentiation for a shape optimization problem incorporating various turbulence models; and Nielsen and Diskin [58] tested the accuracy of the unsteady discrete-adjoint for the incompressible Navier–Stokes equations discretized on composite grids using a complex-variable approach and demonstrated its utility for shape optimization of a wind turbine geometry.

None of the discretizations used in these examples are commonly used for aeroacoustic predictions of compressible turbulence because their resolution is typically deemed to be inadequate. The motivation for choosing discretization schemes in these examples has been to facilitate a straightforward derivation of the discrete-adjoint; we instead employ the same high-resolution numerics commonly used for aeroacoustic and compressible turbulence simulations. de Pando et al. [17] outlined an algorithm for efficiently evaluating the semi-discrete-adjoint operator from a modular implementation of a high-order nonlinear flow solver. While this modular approach is attractive, there is a lost opportunity for combining operations in the adjoint evaluation which we exploit to save on computational cost. We shall also see that our approach requires even fewer modifications to the code than their formulation. Moreover, our formulation can provide a gradient that is compatible with the space–time discrete equations at no additional computational cost. Its accuracy is therefore not limited by either spatial or temporal resolution. The implementation is built directly from operations already available for solving the flow equations with important but remarkably few changes required to the algorithm.

Though it is well known that tools are available for automatic differentiation of discrete systems [25, 50], these tools have rarely been used in flow simulations because they do not yield code with sufficient efficiency for use with large-scale simulations. Moreover, the underlying linear systems can be large and can become stiff or otherwise ill-conditioned on stretched grids or in the presence of complex source terms [20]. A fully discrete adjoint method has not yet been reported for this class of high-resolution schemes, perhaps due to their formidable complexity. The simplifications we identify are essential for its practical implementation.

We verify that our fully discrete adjoint method provides an exact (aside from finite-precision errors) gradient of the cost functional for the sound radiated by a compressible turbulent mixing layer.

1.3.2 Dual-consistent high-fidelity discretization

We design a spatially dual-consistent discretization of the viscous compressible flow equations, in a manner that will be useful for high-fidelity simulation of compressible turbulent flows on multi-block meshes for complex flow domains. We do this while retaining the generality of our approach for a broad class of explicit finite-difference operators that satisfy an SBP rule. Such operators have been constructed for arbitrary orders of accuracy and are proven to work well for the class of flows we wish to study [19]. The dual-consistent formulation we develop here for the same workhorse high-order methods often used in high-fidelity flow and turbulence simulations constitutes an important advance of our work.

By combining a spatially dual-consistent approach with a fully discrete adjoint method for multi-stage explicit time integration, we obtain adjoint-based sensitivities that are compatible with the space–time discrete forward model, without contamination from the numerical or spurious spatial sensitivity modes supported by traditional discrete-adjoint approaches [72, 13]. We demonstrate practical application of our formulation for turbulence by determining the adjoint-based sensitivity of the noise radiated by a Mach 1.3 turbulent jet with respect to a thermal actuation, modeled for simplicity as a source term with compact support in the jet's initial shear layers. We confirm that the proposed dual-consistent discretization is an accurate model for the jet by validating turbulence statistics and far-field sound spectra with experiment. Further, we verify that its adjoint provides the exact sensitivity gradient of the aeroacoustic cost functional up to finite-precision errors. Implications for controllability of turbulent noise and limitations of adjoint-based methods for sensitivity analysis of time-averaged functionals in chaotic turbulence are discussed.

Chapter 2

Predictive Model

This chapter describes the predictive model, which consists of an initial boundary value problem (IBVP) for density, momentum and energy, and integral expressions for the objective functional in terms of these variables. The predictive model yields an estimate of the (scalar-valued) objective functional as output, with initial and boundary conditions as input. Examples of objective functionals presented here include aeroacoustic noise and drag/lift forces. The predictive model is discussed as implemented in the numerical solver. Later chapters that describe specific applications will include some minor variations of the model presented here. Discretization of the predictive model is discussed in Chapter 3. Boundary conditions and their dual-consistent implementation are discussed separately in Chapter 5.

2.1   Computational Domain

We take the physical domain $\mathbb{D}_p$ to be a non-empty bounded open subset of the three-dimensional[*] Euclidean space $\mathbb{R}^3$. Many flows of interest, particularly in aeroacoustics, are best modeled by domains with infinite extent. However, for practical implementations, we use a truncated physical domain, which introduces artificial boundaries. The infinite extent of the physical domain can be effectively simulated by padding the artificial computational boundaries with a sponge layer, where a damping term is added to the right-hand-side (RHS) of the governing equations that drives the solution towards a known target state [22]. Section 5.1 describes this in more detail. We assume that $\mathbb{D}_p$ contains no internal holes. This assumption merely simplifies the formulation and can be relaxed without significant difficulty. Further, we assume that $\overline{\mathbb{D}}_p = \mathbb{D}_p \cup \partial \mathbb{D}_p$ is diffeomorphic to the unit cube $\overline{\mathbb{D}}$, where $\mathbb{D} = (0,1)^3$, and $\overline{\mathbb{D}}_p$ and $\overline{\mathbb{D}}$ denote the closures of $\mathbb{D}_p$ and $\mathbb{D}$, respectively. We refer to $\mathbb{D}$ as the computational domain. The formulation is later extended to include physical domains that violate this property, but can be written as the union of multiple disjoint non-empty bounded open subsets of $\mathbb{R}^3$ (blocks) such that their closures are each diffeomorphic to $\overline{\mathbb{D}} = [0,1]^3$. Our analysis for the "single-block" problem presented here is integral to the formulation for the "multi-block"

---

[*]Throughout the formulation, we consider a three-dimensional physical domain; the formulation is easily extendable to one- and two-dimensional problems.
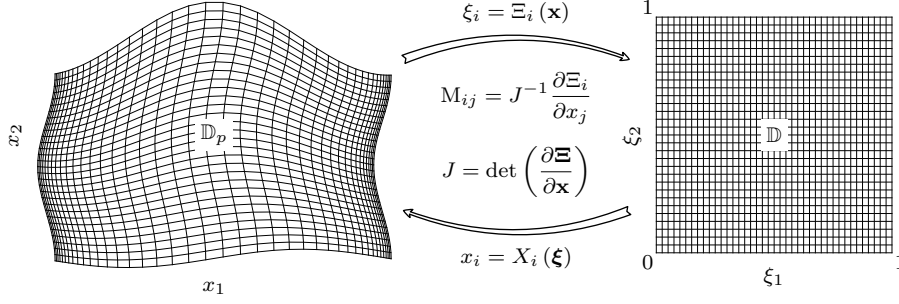
Figure 2.1: Example of a diffeomorphic transformation between a two-dimensional curvilinear physical domain and a unit square.

case discussed in Section 5.4.

The transformation between physical coordinates $\mathbf{x} = (x_1, x_2, x_3)$ and computational coordinates $\boldsymbol{\xi} = (\xi_1, \xi_2, \xi_3)$ is written as $\xi_i = \Xi_i(\mathbf{x})$ with inverse $x_i = X_i(\boldsymbol{\xi})$, for $i = 1, 2, 3$ (see Figure 2.1). The Jacobian matrix $\frac{\partial \Xi}{\partial \mathbf{x}}$ is assumed to be positive-definite. Thus, the Jacobian

$$J \equiv \det\left(\frac{\partial \Xi}{\partial \mathbf{x}}\right) > 0, \ \forall \mathbf{x} \in \mathbb{D}_p. \tag{2.1}$$

We define normalized metrics

$$\mathrm{M}_{ij} = J^{-1}\frac{\partial \Xi_i}{\partial x_j}. \tag{2.2}$$

If closed-form expressions for $X_i(\boldsymbol{\xi})$ are available, the metrics may be determined using the transformation identity, which gives:

$$\mathrm{M}_{ij} = \frac{1}{2}\epsilon_{jmn}\epsilon_{ipq}\frac{\partial X_m}{\partial \xi_p}\frac{\partial X_n}{\partial \xi_q}. \tag{2.3}$$

In the absence of closed-form expressions for $X_i(\boldsymbol{\xi})$, the metrics are evaluated numerically as discussed in Section 3.3.

The boundary of the computational domain can be split as $\partial \mathbb{D} = \bigcup_{i=1}^{3}\left(B_i^- \cup B_i^+\right)$, where

$$B_1^- = \{\boldsymbol{\xi} : \xi_1 = 0, \ 0 \le \xi_2, \xi_3 \le 1\}, \qquad B_1^+ = \{\boldsymbol{\xi} : \xi_1 = 1, \ 0 \le \xi_2, \xi_3 \le 1\}$$

$$B_2^- = \{\boldsymbol{\xi} : \xi_2 = 0, \ 0 \le \xi_1, \xi_3 \le 1\}, \qquad B_2^+ = \{\boldsymbol{\xi} : \xi_2 = 1, \ 0 \le \xi_1, \xi_3 \le 1\}$$

$$B_3^- = \{\boldsymbol{\xi} : \xi_3 = 0, \ 0 \le \xi_1, \xi_2 \le 1\}, \qquad B_3^+ = \{\boldsymbol{\xi} : \xi_3 = 1, \ 0 \le \xi_1, \xi_2 \le 1\}. \tag{2.4}$$

Based on this definition, the boundary surfaces are not disjoint. A consequence of this is that penalty terms for enforcing boundary conditions weakly with support on, say, B_1^- and B_2^-, are added for $\boldsymbol{\xi} \in B_1^- \cap B_2^-$.

8

The unit normal vector to the surface $B_\alpha^\pm$ is $\hat{M}_{\alpha i} = M_{\alpha i}/\tilde{M}_\alpha$, where $\tilde{M}_\alpha = \sqrt{M_{\alpha i} M_{\alpha i}}$, for $\alpha = 1, 2, 3$ (no summation is implied for Greek indices, repeated or otherwise).

Let $V = H^0\left(\mathbb{R}_0^+\right) \times H^0\left(\overline{\mathbb{D}}\right)$ be the space of L^2-functions from $[0, \infty) \times \overline{\mathbb{D}}$ to $\mathbb{R}$. For m field variables, $m \in \mathbb{N}$, V^m admits the inner product

$$\langle f, g \rangle = \int_{t=0}^{\infty} \int_{\boldsymbol{\xi} \in \mathbb{D}} f^{\mathrm{T}}\left(\boldsymbol{\xi}, t\right) g\left(\boldsymbol{\xi}, t\right) \frac{1}{J\left(\boldsymbol{\xi}\right)} d^3 \boldsymbol{\xi} dt, \quad f, g \in V^m, \tag{2.5}$$

and a corresponding norm $\|f\| = \sqrt{\langle f, f \rangle}$. Equipped with this inner product, V is a Hilbert space. For the compressible flow equations, we will analyze and manipulate the state variable as a vector field $Q \in V^5$, where $Q = \begin{bmatrix} \rho & \rho u_1 & \rho u_2 & \rho u_3 & \rho E \end{bmatrix}^{\mathrm{T}}$ is the non-dimensional state vector.

2.2 Governing Equations

The equations governing three-dimensional compressible viscous flow of an ideal gas are expressed as conservation laws for the state variable

$$Q^\star = \begin{bmatrix} \rho^\star & \rho^\star u_1^\star & \rho^\star u_2^\star & \rho^\star u_3^\star & \rho^\star E^\star \end{bmatrix}^{\mathrm{T}},$$

where $\rho^\star E^\star = \rho^\star C_v^\star T^\star + \frac{1}{2}\rho^\star u_i^\star u_i^\star$ is the total energy, and the superscript $\star$ indicates a dimensional quantity. The equation of state is $p^\star = \rho^\star R^\star T^\star$, where $R^\star = (\gamma - 1) C_v^\star$ is the specific gas constant and the ratio of specific heats $\gamma = 1.4$. For a Newtonian fluid obeying Fourier's law of heat conduction,

$$\tau_{ij}^\star = \mu^\star \left(\frac{\partial u_i^\star}{\partial x_j^\star} + \frac{\partial u_j^\star}{\partial x_i^\star} \right) + \lambda^\star \frac{\partial u_k^\star}{\partial x_k^\star} \delta_{ij}, \quad \text{and} \quad q_i^\star = -\kappa^\star \frac{\partial T^\star}{\partial x_i^\star}.$$

Variables are non-dimensionalized using a reference length $L^\star$ and reference scales denoted by the subscript ∞. The non-dimensional variables are

$$x_i = \frac{x_i^\star}{L^\star}, \qquad t = \frac{t^\star}{L^\star/a_\infty^\star}, \qquad u_i = \frac{u_i^\star}{a_\infty^\star},$$

$$\rho = \frac{\rho^\star}{\rho_\infty^\star}, \qquad p = \frac{p^\star}{\rho_\infty^\star a_\infty^{\star 2}}, \qquad T = \frac{T^\star}{a_\infty^{\star 2}/C_{p\infty}^\star},$$

$$\mu = \frac{\mu^\star}{\mu_\infty^\star}, \qquad \lambda = \frac{\lambda^\star}{\mu_\infty^\star}, \qquad \kappa = \frac{\kappa^\star}{\mu_\infty^\star},$$

$$E = \frac{E^\star}{a_\infty^{\star 2}}, \qquad \tau_{ij} = \frac{\tau_{ij}^\star}{\mu_\infty^\star a_\infty^\star/L^\star}, \qquad q_i = \frac{q_i^\star}{\frac{\mu_\infty^\star a_\infty^{\star 2}}{\mathrm{Pr} L^\star}}.$$

9

With no control action yet included, the transformed non-dimensional governing equations are

$$\frac{\partial Q}{\partial t} + J \frac{\partial}{\partial \xi_i} \left[\mathrm{M}_{ij} \left(F_j^I - F_j^V \right) \right] = 0, \ \boldsymbol{\xi} \in \mathbb{D}, \ t > 0, \tag{2.6}$$

where

$$F_i^I = \begin{bmatrix} \rho u_i \\ \rho u_1 u_i + p \delta_{i1} \\ \rho u_2 u_i + p \delta_{i2} \\ \rho u_3 u_i + p \delta_{i3} \\ u_i \left(\rho E + p \right) \end{bmatrix} \quad \text{and} \quad F_i^V = \begin{bmatrix} 0 \\ \tau_{1i} \\ \tau_{2i} \\ \tau_{3i} \\ u_j \tau_{ji} - q_i \end{bmatrix} \tag{2.7}$$

are the inviscid and viscous contributions to the fluxes, respectively and M_{ij} are the normalized metrics defined in (2.2). The non-dimensional stress tensor and heat flux are:

$$\tau_{ij} = \frac{\mu}{\mathrm{Re}} \left(\frac{\partial u_i}{\partial x_j} + \frac{\partial u_j}{\partial x_i} \right) + \frac{\lambda}{\mathrm{Re}} \frac{\partial u_k}{\partial x_k} \delta_{ij} \quad \text{and} \quad q_i = -\frac{\mu}{\mathrm{RePr}} \frac{\partial T}{\partial x_i}, \tag{2.8}$$

where viscosity is modeled as a power law

$$\mu = \left[\left(\gamma - 1 \right) T \right]^n, \tag{2.9}$$

with $n = 0.666$ as a model for air. The second coefficient of vicosity $\lambda = \mu_B - \frac{2}{3}\mu$, where $\mu_B = 0.6\mu$ is chosen as a model for bulk viscosity of air [37]. The Reynolds number is $\mathrm{Re} = \frac{\rho_\infty^\star a_\infty^\star L^\star}{\mu_\infty^\star}$ and the Prandtl number is $\mathrm{Pr} = \frac{\mu^\star C_p^\star}{\kappa^\star}$ (assumed constant), where $\kappa^\star$ is the thermal conductivity.

Following Wei and Freund [90], the left-hand side of (2.6) is written using a compact operator notation

$$\mathcal{N}\left[Q\right]\left(\boldsymbol{\xi}, t\right) = \frac{\partial Q}{\partial t} - \mathcal{R}\left[Q\right]\left(\boldsymbol{\xi}, t\right), \tag{2.10}$$

where

$$\mathcal{R}\left[Q\right]\left(\boldsymbol{\xi}, t\right) = -J\left(\boldsymbol{\xi}\right) \frac{\partial}{\partial \xi_i} \left[\mathrm{M}_{ij}\left(\boldsymbol{\xi}\right) \left\{ \mathcal{F}_j^I\left[Q\right]\left(\boldsymbol{\xi}, t\right) - \mathcal{F}_j^V\left[Q\right]\left(\boldsymbol{\xi}, t\right) \right\} \right]. \tag{2.11}$$

$\mathcal{N}\left[Q\right]$, $\mathcal{R}\left[Q\right]$, $\mathcal{F}_i^I\left[Q\right]$, and $\mathcal{F}_i^V\left[Q\right]$ are vector field-valued operators. We will use the compact form $\mathcal{N}\left[Q\right]$ to denote a vector-field-valued operator $\mathcal{N}\left[Q\right]\left(\boldsymbol{\xi}, t\right)$ wherever this more compact notation is unambiguous. $\mathcal{R}\left[Q\right]$ is a nonlinear operator that maps the state space S to V^5, where $S = \left[H^1\left(\mathbb{R}^+\right) \times H^2\left(\mathbb{D}\right) \right]^5$. In order to formulate the continuous-adjoint equations in Chapter 4, we will require the Fréchet derivative of $\mathcal{R}\left[Q\right]$,

which is obtained in the usual way by linearizing (2.11):

$$\delta \mathcal{R}\left[Q;\delta Q\right] \equiv \mathcal{R}\left[Q + \delta Q\right] - \mathcal{R}\left[Q\right], \quad \|\delta Q\| \ll 1. \tag{2.12}$$

The derivation of $\delta \mathcal{R}\left[Q;\delta Q\right]$ is included in Appendix A; we only compactly represent the final result here:

$$\delta \mathcal{R}\left[Q;\delta Q\right] = -J\frac{\partial}{\partial \xi_i}\left\{\mathcal{A}_i\left[Q\right]\delta Q - \mathcal{B}_{ij}\left[Q\right]\frac{\partial}{\partial \xi_j}\left(\mathcal{C}\left[Q\right]\delta Q\right)\right\}, \tag{2.13}$$

where $\mathcal{A}_i\left[Q\right] = \mathcal{A}_i^I\left[Q\right] - \mathcal{A}_i^V\left[Q\right]$, for $i = 1, 2, 3$, and $\mathcal{A}_i^I\left[Q\right]$, $\mathcal{A}_i^V\left[Q\right]$, $\mathcal{B}_{ij}\left[Q\right]$ and $\mathcal{C}\left[Q\right]$ are tensor-field-valued operators defined in (A.4).

2.3   Objective Functional and Control Action

We consider a specific form of the objective functional $\mathcal{J}\left[Q\right] : S \to \mathbb{R}$ that can be expressed as

$$\mathcal{J}\left[Q\right] = \int_{t=0}^{\infty}\int_{\boldsymbol{\xi}\in\mathbb{D}}\mathcal{K}_V\left[Q\right]W_\Omega\frac{1}{J}d^3\boldsymbol{\xi}dt + \int_{t=0}^{\infty}\int_{\partial\mathbb{D}}\mathcal{K}_S\left[Q\right]W_{\Omega'}d^2\boldsymbol{\xi}dt, \tag{2.14}$$

where at least one of $\mathcal{K}_V\left[Q\right]\left(\boldsymbol{\xi}, t\right)$ or $\mathcal{K}_S\left[Q\right]\left(\boldsymbol{\xi}, t\right)$ is a non-trivial scalar-field-valued operator and $\mathcal{K}_V\left[Q\right]$ is not a function of the differentiation operators $\frac{\partial}{\partial \xi_i}$ for $i = 1, 2, 3$. $W_\Omega\left(\boldsymbol{\xi}, t\right)$ and $W_{\Omega'}\left(\boldsymbol{\xi}, t\right)$ are mollifying compact support functions that define a (possibly non-stationary) target region of interest $\Omega\left(t\right)\cup\Omega'\left(t\right) \subseteq \overline{\mathbb{D}}$. In this work, we only consider stationary target regions and all of our examples of $\mathcal{J}\left[Q\right]$ are such that only one of $\mathcal{K}_V\left[Q\right]$ or $\mathcal{K}_S\left[Q\right]$ is non-trivial. Further, we design mollifying support functions with a factor $H\left(t_0\right) - H\left(t_1\right)$, where $t_1 > t_0$ and $H\left(x\right)$ is the Heavyside function. This restricts the measurement of $\mathcal{J}\left[Q\right]$ to a finite control time horizon $[t_0, t_1]$. We also define the *instantaneous* objective functional

$$\mathcal{I}\left[Q\right]\left(t\right) = \int_{\mathbb{D}}\mathcal{K}_V\left[Q\right]W_\Omega\frac{1}{J}d^3\boldsymbol{\xi} + \int_{\partial\mathbb{D}}\mathcal{K}_S\left[Q\right]W_{\Omega'}d^2\boldsymbol{\xi}.$$

We consider two examples of objective functionals that are useful for our target applications:

1. **Aeroacoustic noise**

   For our noise-suppression demonstrations, we use the acoustic intensity

   $$\mathcal{K}_V\left[Q\right]\left(\boldsymbol{\xi}, t\right) = \left|p\left(\boldsymbol{\xi}, t\right) - \overline{p}\left(\boldsymbol{\xi}\right)\right|^2, \quad \mathcal{K}_S\left[Q\right]\left(\boldsymbol{\xi}, t\right) = 0, \tag{2.15}$$

   where $p\left(\boldsymbol{\xi}, t\right)$ is the instantaneous pressure field and $\overline{p}\left(\boldsymbol{\xi}\right)$ is the time-averaged mean pressure field.

In addition, we ensure that Ω is chosen sufficiently far away from the nominal acoustic source region, where the pressure fluctuations are nonlinear and hydrodynamic.

2. **Drag force**

   For simplicity, we consider here a solid body whose boundary is aligned with a computational boundary surface $B_\alpha^\pm$ for $\alpha = 1, 2, 3$ under the transformation described in Section 2.1. For instance, consider an O-grid where one of the computational boundaries coincides with the boundary of a cylindrical solid body. The time-averaged force exerted by the fluid on the solid body due to hydrodynamic pressure along a fixed direction with unit vector $\hat{\mathbf{k}}$ is proportional to $\mathcal{J}[Q]$ defined according to (2.14) with

$$\mathcal{K}_V[Q](\boldsymbol{\xi}, t) = 0, \quad \mathcal{K}_S[Q](\boldsymbol{\xi}, t) = -[p(\boldsymbol{\xi}, t) - p_\infty] \mathrm{M}_{\alpha i} \hat{k}_i, \tag{2.16}$$

   where $\mathrm{M}_{\alpha i} d^2 \boldsymbol{\xi}$ represents the components of the infinitesimal area vector on the surface $B_\alpha^\pm$. Drag and lift forces may be quantified in this manner by choosing the unit vector $\hat{\mathbf{k}}$ appropriately.

Using (2.14), we can calculate a baseline value of the objective functional as the result of a predictive simulation that solves (2.6) for $Q(\boldsymbol{\xi}, t)$. In optimal control theory, the objective is to minimize $\mathcal{J}[Q]$ using a control action, assumed here to be a body force added to the right-hand side of (2.6):

$$\frac{\partial Q}{\partial t} = \mathcal{R}[Q] + W_\Gamma(\boldsymbol{\xi}) \circ f(\boldsymbol{\xi}, t), \ \boldsymbol{\xi} \in \mathbb{D}, \ t_0 \leq t \leq t_1, \tag{2.17}$$

where $W_\Gamma(\boldsymbol{\xi})$ is a (vector-valued) mollifying compact support that defines a control region $\Gamma \subseteq \mathbb{D}$ in which the control forcing term is active, and $\circ$ denotes the elementwise product. This choice for modeling the control action is flexible, since its space–time discretized representation consists of as many independent control parameters as the number of grid points contained in Γ times the number of sub-steps involved in marching through the control time horizon $[t_0, t_1]$. The motivation behind choosing such a control is two-fold:

1. It serves as a model for an array of plasma actuators, which act as momentum and heat sources and can be designed to provide flexible actuation [69].

2. It gives an estimate of the maximal reduction of the objective functional that is possible through active control (subject to the fidelity of our predictive model), which provides a benchmark for designing real actuators with relatively limited flexibility.

The forced governing equations are compactly written as

$$\mathcal{M}[Q, f] = 0, \tag{2.18}$$

12

where

$$\mathcal{M}[Q, f] \equiv \mathcal{N}[Q] - W_\Gamma \circ f \qquad (2.19)$$

is called the *forward* or *primal* operator and $\mathcal{N}[Q]$ is defined in (2.10). The control forcing function $f(\boldsymbol{\xi}, t)$ alters the value of the objective functional by changing the flow solution $Q(\boldsymbol{\xi}, t)$ of (2.18). We denote

$$\mathcal{J}_f[Q] = \mathcal{J}[Q : \mathcal{M}[Q, f] = 0, \boldsymbol{\xi} \in \mathbb{D}, t_0 \leq t \leq t_1].$$

2.4 Accuracy of the Adjoint-based Gradient

The total variation of the objective functional is

$$\delta\mathcal{J}[Q, f; \delta f] = \mathcal{J}_{f+\delta f}[Q] - \mathcal{J}_f[Q], \ \forall \delta f \in V^5.$$

The adjoint solution, denoted as $Q^\dagger(\boldsymbol{\xi}, t)$, provides a sensitivity gradient $\mathcal{G}[Q^\dagger](\boldsymbol{\xi}, t)$ — the Fréchet derivative of $\mathcal{J}_f[Q]$ — the precise formulation for which is provided in Chapter 4. Solving (2.17) with $f^{(0)}(\boldsymbol{\xi}, t) = 0$ provides a baseline solution $Q^{(0)}(\boldsymbol{\xi}, t)$. In our target applications, the sensitivity gradient sets the initial search direction along which better controls $f(\boldsymbol{\xi}, t)$ are sought by determining an $\alpha_{\min}$ such that

$$f^{(1)}(\boldsymbol{\xi}, t) = f^{(0)}(\boldsymbol{\xi}, t) - \alpha_{\min}\mathcal{G}\left[Q^{\dagger(0)}\right](\boldsymbol{\xi}, t), \ \alpha_{\min} \in \mathbb{R}_0^+, \qquad (2.20)$$

minimizes $\mathcal{J}_{f^{(1)}}[Q]$. As discussed in Chapter 1, it is understood that adjoint formulations potentially have inherent inconsistencies that limits their accuracy. To quantify these errors in order to assess the quality of gradient predictions and validate our discrete-adjoint implementation, we compare the adjoint-based sensitivity with a finite-difference derived estimate of the gradient. To measure these errors, we consider the variation in the control forcing, which is thus related to the gradient as

$$\delta f(\boldsymbol{\xi}, t) \equiv f(\boldsymbol{\xi}, t) - f^{(0)}(\boldsymbol{\xi}, t) = -\alpha\mathcal{G}\left[Q^{\dagger(0)}\right](\boldsymbol{\xi}, t),$$

where $\alpha \in \mathbb{R}_0^+$ is a distance measure in the control space. Expanding the cost functional using a Taylor series, we obtain

$$\mathcal{J}_{f+\delta f}[Q] = \mathcal{J}_f\left[Q^{(0)}\right] + \left\langle \mathcal{G}\left[Q^{\dagger(0)}\right], \delta f \right\rangle + \mathcal{O}\left(\|\delta f\|^2\right),$$

13

or equivalently,

$$\mathcal{J}_{f+\delta f}[Q] - \mathcal{J}_f\left[Q^{(0)}\right] = -\alpha\left\|\mathcal{G}\left[Q^{\dagger(0)}\right]\right\|^2 + \mathcal{O}\left(\alpha^2\right). \tag{2.21}$$

This leads to an error measure

$$\mathcal{E} = \left|\frac{\mathcal{J}_{f+\delta f}[Q] - \mathcal{J}_f\left[Q^{(0)}\right]}{\alpha} + \left\|\mathcal{G}\left[Q^{\dagger(0)}\right]\right\|^2\right|, \tag{2.22}$$

where $\mathcal{J}$ and $\mathcal{G}$ are computed by solving the *discretized* forward and adjoint equations. Therefore,

$$\mathcal{E} = \mathcal{O}\left(\alpha\right) + \mathcal{O}\left(\frac{1}{N_i^a}, \Delta t^b\right) + \mathcal{O}\left(\epsilon^c, N_i^d, \frac{1}{\Delta t^e}\right), \tag{2.23}$$

where N_i is the number of grid points used to discretize the computational domain along the ξ_i-direction, Δt is the time step size (assumed constant), and ϵ represents precision of floating-point operations (machine epsilon), which takes into account the effect of roundoff errors in finite-precision floating-point arithmetic. In (2.23):

1. $\mathcal{O}\left(\alpha\right)$ is the error due to a first-order finite-difference approximation of the gradient embodied in (2.22),

2. $\mathcal{O}\left(\frac{1}{N_i^a}, \Delta t^b\right)$, $a, b > 0$ is due to numerical discretization reflecting the order of accuracy of the numerical differentiation and quadrature schemes used to obtain the solutions $Q(\boldsymbol{\xi}, t)$ and $Q^\dagger(\boldsymbol{\xi}, t)$, and the objective functional (2.14), and

3. $\mathcal{O}\left(\epsilon^c, N_i^d, \frac{1}{\Delta t^e}\right)$, $c, d, e > 0$, is an upper bound for the accumulation of roundoff errors due to the finite-precision arithmetic employed when solving the discretized forward and adjoint equations.

In general, it is not possible to anticipate how these errors accumulate for a turbulent flow, which is our primary target application, or which of the terms on the RHS of (2.23) will dominate. This is important to understand since it directly affects the utility of the adjoint solution in providing an approximate gradient. Since turbulence is well understood to be chaotic, even having the nominally exact adjoint in its discrete formulation does not guarantee its utility for any control objective due to the effect of finite-precision arithmetic and how it can be amplified by the chaos. Nadarajah and Jameson [56] used an alternate error measure based on a complex-step derivative of the objective functional. We do not use this approach since it is computationally three times more expensive than the finite-difference approach, and its advantages over the current approach do not adequately justify the added computational cost for turbulence simulations.

Chapter 3

Discretization

In this chapter, we introduce the discretization of the predictive model. We will also use the same numerical schemes for approximating spatial and temporal derivatives in the continuous-adjoint equations, although this is not a requirement. On the other hand, the discrete-adjoint equations are inherently tied to the numerical schemes employed in the discretization of the predictive model. Therefore, it is important to address the discretization first before formulating the discrete-exact adjoint in Chapter 4. We will use the term "semi-discrete" to refer to the form of the governing equations after spatial discretization has been applied, which produces a system of ODEs in time. Likewise, we use "fully discrete" to refer to the algebraic system of equations obtained from spatial *and* temporal discretization.

3.1   Summation-by-parts Operators

Recall the definition of V from Section 2.1. We consider a computational grid $\{0, h, 2h, \ldots, (N-1)\,h\}^3$, where $h = \frac{1}{N-1}$, which maps each element of V to $V_h = \left[H^0\left(\mathbb{R}_0^+\right)\right]^{N^3}$. We denote this mapping as $\vec{f}(t) = \mathrm{proj}\left[f\left(\boldsymbol{\xi}, t\right)\right]$, where $f \in V^m$ is a vector-valued function of space and time, and $\vec{f} \in V_h^m$ is the corresponding semi-discrete vector. We have taken the number of grid points in all directions to be equal to simplify the discussion. Let $\hat{\mathbf{P}}$ be a symmetric positive-definite matrix. For $m \in \mathbb{N}$, V_h^m admits the inner product

$$\left\langle \vec{f}, \vec{g} \right\rangle_{\hat{\mathbf{P}}} = \int_{t=0}^{\infty} \vec{f}^{\mathrm{T}}(t) \left\{ I_m \otimes \left(\hat{\mathbf{J}}^{-1}\hat{\mathbf{P}} \right) \right\} \vec{g}(t)\, dt, \quad \vec{f}, \vec{g} \in V_h^m, \tag{3.1}$$

where $\hat{\mathbf{J}} = \mathrm{diag}\left(\vec{J} \right)$, I_m is the $m \times m$ identity matrix, and $\otimes$ is the Kronecker product [82].

Let $\hat{\mathbf{D}}_i$ be a finite-difference operator that approximates a partial first-derivative with respect to the computational coordinate ξ_i. In one dimension, $\hat{\mathbf{D}}_i$ is a banded matrix. In two dimensions, we assume that $\hat{\mathbf{D}}_1$ is a block-diagonal matrix with $N_2 \times N_2$ blocks, such that each block is an $N_1 \times N_1$ banded matrix, resulting in a total of $N_1 N_2 \times N_1 N_2$ entries. Likewise, $\hat{\mathbf{D}}_2$ is block-banded with $N_2 \times N_2$ blocks where each block is an $N_1 \times N_1$ diagonal matrix. In three dimensions, the sparsity structure of $\hat{\mathbf{D}}_i$ is even more

complicated. To describe this using a straightforward formula, we use the Kronecker product, to write

$$\hat{\mathbf{D}}_1 = \hat{D} \otimes I_N \otimes I_N$$

$$\hat{\mathbf{D}}_2 = I_N \otimes \hat{D} \otimes I_N$$

$$\hat{\mathbf{D}}_3 = I_N \otimes I_N \otimes \hat{D}, \tag{3.2}$$

where $\hat{D} \in \mathbb{R}^{N \times N}$ satisfies the SBP rule [41, 75]:

$$\hat{P}\hat{D} + \left(\hat{P}\hat{D}\right)^{\mathrm{T}} = \mathrm{diag} \begin{bmatrix} -1 & 0 & \dots & 0 & 1 \end{bmatrix}^{\mathrm{T}}, \tag{3.3}$$

with $\hat{P} \in \mathbb{R}^{N \times N}$ a symmetric positive-definite matrix. We emphasize that the Kronecker product is merely a mathematical tool to facilitate certain proofs involving the operators $\hat{\mathbf{D}}_i$ in three dimensions. For practical implementation, the matrices $\hat{\mathbf{D}}_i$ are not actually formed, i.e., all the non-zero entries of $\hat{\mathbf{D}}_i$ are never simultaneously stored in memory. Instead, the operation $\hat{\mathbf{D}}_1 \vec{f}$, for example, is implemented as if it were a one-dimensional matrix-vector product along the ξ_1-direction, within a loop that iterates through the elements of $\vec{f}$ in the ξ_2- and ξ_3-directions. In (3.3), $\hat{P}$ defines a quadrature rule and is called the norm matrix [30]. Naturally, we use $\hat{\mathbf{P}} = \hat{P} \otimes \hat{P} \otimes \hat{P}$ to define the inner product (3.1).

We only consider a diagonal norm $\hat{P}$, since this preserves the SBP property under a coordinate transformation for arbitrary orders of accuracy [77]. Diagonal-norm SBP operators consist of $2s$-order accurate centered-difference stencils at interior points and s-order accurate biased stencils near boundaries. The global accuracy with respect to the norm defined by $\hat{P}$ is $s+1$. The operator is unique for $s = 2$, has one free parameter for $s = 3$, and three free parameters for $s = 4$. For $s = 4$ we use the coefficients derived by Diener et al. [19], which are optimized to have minimum largest eigenvalue of the amplification matrix. The SBP operators for $s = 2, 3, 4$ used in this paper are refered to as the SBP 2–4, 3–6, and 4–8 schemes, respectively. Figure 3.1 shows a plot of the modified wavenumber of the interior stencil corresponding to these operators.

In three dimensions, the SBP property leads to

$$\hat{\mathbf{P}}\hat{\mathbf{D}}_i + \left(\hat{\mathbf{P}}\hat{\mathbf{D}}_i\right)^{\mathrm{T}} = \hat{\mathbf{\Delta}}_i, \tag{3.4}$$
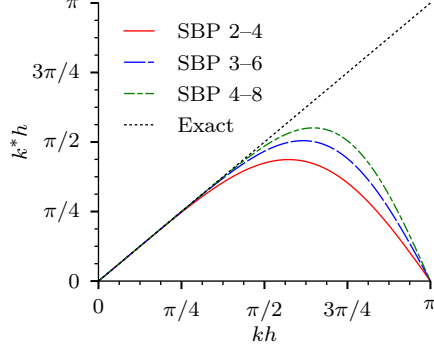
Figure 3.1: Modified wavenumber $k^*h = 2\sum_j a_j \sin(jkh)$ of the interior stencil corresponding to the SBP 2–4, 3–6, and 4–8 schemes.

with $\hat{\boldsymbol{\Delta}}_i = \hat{\boldsymbol{\Delta}}_i^- - \hat{\boldsymbol{\Delta}}_i^+$ for $i = 1, 2, 3$,

$$\hat{\boldsymbol{\Delta}}_1^\pm = E^\pm \otimes \hat{P} \otimes \hat{P}$$
$$\hat{\boldsymbol{\Delta}}_2^\pm = \hat{P} \otimes E^\pm \otimes \hat{P}$$
$$\hat{\boldsymbol{\Delta}}_3^\pm = \hat{P} \otimes \hat{P} \otimes E^\pm, \tag{3.5}$$

$E^+ = \mathrm{diag} \begin{bmatrix} 1 & 0 & \dots & 0 \end{bmatrix}^\mathrm{T} \in \mathbb{R}^{N \times N}$ and $E^- = \mathrm{diag} \begin{bmatrix} 1 & 0 & \dots & 0 \end{bmatrix}^\mathrm{T} \in \mathbb{R}^{N \times N}$. Thus, when $\hat{\mathbf{P}}^{-1}\hat{\boldsymbol{\Delta}}_\alpha^\pm$ multiplies a semi-discrete vector $\vec{f} \in V_h$, it zeros out the components of $\vec{f}$ corresponding to nodes that are not located on the computational surface $B_\alpha^\pm$, and scales the remaining components by $1/\hat{P}_{11}$, where $\hat{P}_{11}$ is the first entry on the diagonal of $\hat{P}$.

Lemma 3.1. *Let $f \in \left[H^0\left(\mathbb{R}_0^+\right) \times H^1\left(\overline{\mathbb{D}}\right) \right]^m$ and $\vec{f} = \mathrm{proj}\,(f)$. If $\hat{\mathbf{D}}_i$ is an SBP operator defined according to (3.2), where D consists of $2s$-order accurate interior stencils, then*

$$\left\| \left(I_m \otimes \hat{\mathbf{D}}_i \right) \vec{f} - \mathrm{proj}\left(\frac{\partial f}{\partial \xi_i} \right) \right\|_\infty = \mathcal{O}\left(h^s\right). \tag{3.6}$$

We denote $\mathbf{D}_i^{(m)} = I_m \otimes \hat{\mathbf{D}}_i$, $\mathbf{P}^{(m)} = I_m \otimes \hat{\mathbf{P}}$, etc., and simply write $\mathbf{D}_i$, $\mathbf{P}$, etc., whenever the value of m can be infered from the semi-discrete vector it multiplies. Further, if $\hat{\mathbf{P}} = \hat{P} \otimes \hat{P} \otimes \hat{P}$, in (3.1), then (3.1) is a $2s$-order accurate approximation of (2.5).

Proof. Eqn. (3.6) follows from the definition of $\hat{\mathbf{D}}_i$. The proof for $\hat{\mathbf{P}}$ as a $2s$-order accurate quadrature scheme is due to Hicken and Zingg [30]. $\qquad \square$

3.2 Artificial Dissipation

Second and mixed derivatives are discretized using repeated first-derivative SBP operators defined in (3.2), resulting in a wide-stencil approximation. This necessitates the use of artificial dissipation, since the wide-stencil approximation does not damp the highest wavenumber supported by the grid. An attractive approach for doing this, which is generally succesful [45] is the application of low pass filters, which damp in effect only the high wavenumbers of the solution to maintain stability. However, these are incompatible with the dual-consistent formulation to be developed in Chapter 5. Mattsson et al. [54] proposed dissipation operators of the form $\widehat{\mathbf{DI}}_\alpha = -\hat{\mathbf{P}}^{-1} \left(\hat{\mathbf{D}}_\alpha^{(s)} \right)^{\mathrm{T}} \hat{\mathbf{B}} \hat{\mathbf{D}}_\alpha^{(s)}$, where

$$\hat{\mathbf{D}}_1^{(s)} = \hat{D}^{(s)} \otimes I_N \otimes I_N$$

$$\hat{\mathbf{D}}_2^{(s)} = I_N \otimes \hat{D}^{(s)} \otimes I_N$$

$$\hat{\mathbf{D}}_3^{(s)} = I_N \otimes I_N \otimes \hat{D}^{(s)},$$

$\hat{D}^{(s)} \in \mathbb{R}^{N \times N}$ is a minimal stencil-width approximation of a partial s-th derivative, and $\hat{\mathbf{B}}$ is a positive semi-definite matrix, assumed to be the identity matrix in the diagonal-norm case. With this choice, we obtain a "composite" operator of the form $-\hat{\mathbf{P}}^{-1} \left(\hat{\mathbf{D}}_\alpha^{(s)} \right)^{\mathrm{T}} \hat{\mathbf{D}}_\alpha^{(s)}$ that is formally $2s$-order accurate at interior points and s-order accurate near boundaries, and which can be applied in the usual manner of explicit finite-difference schemes. The resulting interior stencils are $2s+1$ points wide and are identical to a selective filter whose coefficients are determined for maximum formal order of accuracy [9]. Such schemes have been optimized to make their damping function more selective, and used successfully for predicting the sound generated by a Mach 0.9 jet with $\mathrm{Re}_D = \rho_j U_j D / \mu_j$ up to 4×10^5 [10]. Bogey and Bailly [11] compared this LES approach with a dynamic Smagorinsky model, and showed that selective filtering is better suited for aeroacoutstic simulations since its contribution to the energy dissipation at large scales of the flow, which are primarily responsible for sound generation, is relatively small. However, they noted that this dissipation still exceeds dissipation due to physical viscosity, particularly at smaller resolved scales. Here, we will address this concern for our jet simulation, to be discussed in detail in Chapter 8 in two ways.

First, for our simulations with non-uniform curvilinear meshes we allow the filtering strength to vary spatially by taking $\hat{\mathbf{B}} = \sigma_{\mathrm{diss.}} \tilde{\mathbf{M}}_\alpha$:

$$\widehat{\mathbf{DI}}_\alpha = \sigma_{\mathrm{diss.}} \hat{\mathbf{P}}^{-1} \left(\hat{\mathbf{D}}_\alpha^{(s)} \right)^{\mathrm{T}} \tilde{\mathbf{M}}_\alpha \hat{\mathbf{D}}_\alpha^{(s)}, \tag{3.7}$$

where $\tilde{\mathbf{M}}_\alpha = \mathrm{diag} \left(\mathrm{proj} \left(\tilde{\mathrm{M}}_\alpha \right) \right)$ and $\tilde{\mathrm{M}}_\alpha$ is the area of an infinitesimal surface element whose normal is along

the ξ_α-direction. $\sigma_{\text{diss.}}$ is a positive constant that affords further control over the dissipation strength. Since $\tilde{M}_\alpha > 0$ by definition, this ensures that $\hat{B}$ is positive-definite. For instance, $\tilde{M}_3$ which corresponds to the streamwise direction for our jet simulation, varies from about 3×10^{-5} near the end of the potential core to about 2×10^{-1} at the far-field boundaries, or about four orders of magnitude. Second, our computational grid uses minimum mesh spacings that are an order of magnitude smaller than the values corresponding to the LES of Bogey and Bailly [10]. In fact, the minimum mesh spacings for the current simulation are comparable to the values used for a DNS of a Mach 1.92 jet at $\text{Re}_D = 2000$ [24]. This is expected to increase the filtering cutoff frequency, which is inversely proportional to the minimum mesh spacing.

Another subtle, but important, difference between the proposed artificial dissipation and the selective filtering approach of Bogey and Bailly [9] is the manner in which they are implemented. The dissipation operators satisfy

$$\hat{P}\widehat{DI}_\alpha = \left(\hat{P}\widehat{DI}_\alpha\right)^{\mathrm{T}},\tag{3.8}$$

which makes them self-adjoint under the inner product defined by (3.1). This facilitates crafting a dual-consistent discretization. They are implemented using the projection method [61], and appear on the RHS of the semi-discrete approximation of the governing equations. This ensures that the addition of artificial dissipation does not violate provable stability and dual-consistency of our discretization. The operator on either side of the equality sign in (3.8) is an approximation of $\sigma_{\text{diss.}}\frac{\partial^s}{\partial \xi_\alpha^s}\left(\tilde{M}_\alpha \frac{\partial^s}{\partial \xi_\alpha^s}\right)$, for $\alpha = 1, 2, 3$. Thus, the dissipation term along the ξ_α-direction behaves like an artificial viscosity based on a $2s$-order derivative, with a local diffusion coefficient that depends on the local grid resolution.

3.3   Discretization of Transformation Metrics

Recall the transformation between physical and computational coordinates described in Section 2.1. In Cartesian coordinates, the non-dimensional governing equations (without any control action) are

$$\frac{\partial Q}{\partial t} + \frac{\partial}{\partial x_i}\left(F_i^I - F_i^V\right) = 0,\ \mathbf{x} \in \mathbb{D}_p,\ t > 0,$$

where F_i^I and F_i^V are the inviscid and viscous contributions to the fluxes defined in (2.7). Transforming to computational coordinates yields

$$\frac{\partial Q}{\partial t} + J\frac{\partial}{\partial \xi_i}\left[M_{ij}\left(F_j^I - F_j^V\right)\right] = J\frac{\partial M_{ij}}{\partial \xi_i}\left(F_j^I - F_j^V\right),\ \boldsymbol{\xi} \in \mathbb{D},\ t > 0.\tag{3.9}$$

If closed-form expressions are available for $X_i(\boldsymbol{\xi})$ for $i = 1, 2, 3$, then from (2.3)

$$\frac{\partial \mathrm{M}_{ij}}{\partial \xi_i} = 0, \ j = 1, 2, 3, \tag{3.10}$$

which leads to the transformed equations (2.6). In the absence of closed-form expressions for $X_i(\boldsymbol{\xi})$, care must be taken in discretizing the metrics M_{ij} because violation of the identity (3.10) leads to a grid-dependent forcing term in (3.9), which usually causes numerical instability. Thomas and Lombard [81] modified the analytical form (2.3) so that the metrics satisfy (3.10) when evaluated discretely. Their modification can be expressed using the discrete derivative operators defined in (3.2) as:

$$\vec{\mathrm{M}}_{ij} = \frac{1}{4} \epsilon_{jmn} \epsilon_{ipq} \left[\hat{\mathbf{D}}_q \left(\vec{x}_n \circ \hat{\mathbf{D}}_p \vec{x}_m \right) + \hat{\mathbf{D}}_p \left(\vec{x}_m \circ \hat{\mathbf{D}}_q \vec{x}_n \right) \right], \tag{3.11}$$

where $\vec{\mathrm{M}}_{ij}$ are the semi-discrete vectors corresponding to the metrics $\mathrm{M}_{ij}(\boldsymbol{\xi})$, $\vec{x}_i$ are the semi-discrete vectors corresponding to the physical grid coordinates, and $\circ$ is the Hadamard product. It can be easily shown that (3.11) is a consistent approximation of (2.3). Further, it can be shown using (3.2) and the properties of the Kronecker product, that for $1 \leq i, j \leq 3$, the operators $\hat{\mathbf{D}}_i$ and $\hat{\mathbf{D}}_j$ commute. This leads to a semi-discrete equivalent of (3.10):

$$\hat{\mathbf{D}}_i \vec{\mathrm{M}}_{ij} = 0, \ j = 1, 2, 3.$$

3.4 Spatial Discretization

The semi-discrete approximation of (2.11) is written as

$$\vec{\mathsf{R}} \left[\vec{Q} \right] = -\mathbf{J} \mathbf{D}_i \mathbf{M}_{ij} \left(\vec{\mathsf{F}}_j^I \left[\vec{Q} \right] - \vec{\mathsf{F}}_j^V \left[\vec{Q} \right] \right) + \mathbf{J} \sum_i \mathbf{D} \mathbf{I}_i \vec{Q} + \vec{\mathsf{R}}_{\mathrm{SAT}} \left[\vec{Q} \right], \tag{3.12}$$

for $\vec{Q} \in V_h^5$, where $\mathbf{M}_{ij} = I_5 \otimes \mathrm{diag} \left(\vec{\mathrm{M}}_{ij} \right)$, and

$$\vec{\mathsf{R}}_{\mathrm{SAT}} \left[\vec{Q} \right] = \mathbf{J} \mathbf{P}^{-1} \sum_{i=1}^{3} \left(\vec{\mathsf{R}}_{\mathrm{SAT},i}^{-} \left[\vec{Q} \right] + \vec{\mathsf{R}}_{\mathrm{SAT},i}^{+} \left[\vec{Q} \right] \right) \tag{3.13}$$

is a simultaneous approximation term (SAT) that enforces the boundary conditions in a weak sense. The specific forms of the SATs used for enforcing various types of boundary conditions are discussed in Chapter 5. In (3.12), $\vec{\mathsf{R}} \left[\vec{Q} \right] (t) : V_h^5 \to V_h^5$, etc.

When linearizing $\mathcal{R}[Q]$ in (A.3) in Appendix A, we have deliberately avoided using the product rule of

differentiation, which is not satisfied by our discrete derivative operators. This allows us to reuse the result derived there for the semi-discrete RHS operator, and write

$$\delta \vec{\mathsf{R}} \left[\vec{Q}; \delta \vec{Q}\right] = -\mathbf{J}\mathbf{D}_i \left(\mathbf{A}_i \left[\vec{Q}\right] \delta \vec{Q} - \mathbf{B}_{ij} \left[\vec{Q}\right] \mathbf{D}_j \mathbf{C} \left[\vec{Q}\right] \delta \vec{Q}\right)$$
$$+ \mathbf{J} \sum_i \mathbf{D}\mathbf{I}_i \delta \vec{Q} + \delta \vec{\mathsf{R}}_{\mathrm{SAT}} \left[\vec{Q}; \delta \vec{Q}\right], \tag{3.14}$$

where

$$\delta \vec{\mathsf{R}}_{\mathrm{SAT}} \left[\vec{Q}; \delta \vec{Q}\right] = \mathbf{J}\mathbf{P}^{-1} \sum_{i=1}^{3} \left(\mathbf{S}_{\mathrm{SAT},i}^{-} \left[\vec{Q}\right] + \mathbf{S}_{\mathrm{SAT},i}^{+} \left[\vec{Q}\right]\right) \delta \vec{Q},$$

and $\mathbf{S}_{\mathrm{SAT},i}^{\pm} \left[\vec{Q}\right] \delta \vec{Q} \equiv \delta \vec{\mathsf{R}}_{\mathrm{SAT},i}^{\pm} \left[\vec{Q}; \delta \vec{Q}\right]$ for $\vec{Q}, \delta \vec{Q} \in V_h^5$. In (3.14), $\mathbf{A}_i \left[\vec{Q}\right]$, $\mathbf{B}_{ij} \left[\vec{Q}\right]$ and $\mathbf{C} \left[\vec{Q}\right]$ are projections of the tensor-field-valued operators $\mathcal{A}_i [Q]$, $\mathcal{B}_{ij} [Q]$ and $\mathcal{C} [Q]$ in (2.13) from V^5 onto V_h^5.

3.5 Temporal Discretization

Our approach for formulating the fully discrete adjoint equations in Chapter 4 remains generic to the broad class of popular high-order explicit multi-stage methods. As an example, we consider here a standard fourth-order Runge–Kutta (RK4) scheme. The semi-discrete approximation of the governing equations is

$$\vec{\mathsf{M}} \left[\vec{Q}, \vec{f}\right] (t) \equiv \frac{d\vec{Q}}{dt} - \vec{\mathsf{R}} \left[\vec{Q}\right] (t) - \vec{W}_\Gamma \circ \vec{f}(t) = 0, \ t_0 \le t \le t_1. \tag{3.15}$$

where $\vec{\mathsf{R}} \left[\vec{Q}\right]$ is defined in (3.12). We take the initial condition $\vec{Q}(t_0) = \vec{Q}^0$. Let $t^n = t_0 + \Delta t (n-1)$ for $n = 1, 2, \ldots, N_t + 1$, where $\Delta t = (t_1 - t_0)/N_t$ is the time step size (assumed to be uniform for convenience of presentation), and N_t is the number of time steps. Integrating (3.15) using the seemingly most common RK4 scheme leads to the following system of algebraic equations:

$$\vec{\mathsf{M}}^{n,1} = \frac{2\vec{Q}^{n,1} - 2\vec{Q}^{n-1,4}}{\Delta t} - \vec{\mathsf{R}}^{n-1,4} - \vec{W}_\Gamma \circ \vec{f}^{n,1}$$
$$\vec{\mathsf{M}}^{n,2} = \frac{2\vec{Q}^{n,2} - 2\vec{Q}^{n-1,4}}{\Delta t} - \vec{\mathsf{R}}^{n,1} - \vec{W}_\Gamma \circ \vec{f}^{n,2}$$
$$\vec{\mathsf{M}}^{n,3} = \frac{2\vec{Q}^{n,3} - 2\vec{Q}^{n-1,4}}{\Delta t} - \vec{\mathsf{R}}^{n,2} - \vec{W}_\Gamma \circ \vec{f}^{n,3}$$
$$\vec{\mathsf{M}}^{n,4} = \frac{6\vec{Q}^{n,4} + 2\vec{Q}^{n-1,4} - 2\vec{Q}^{n,1} - 4\vec{Q}^{n,2} - 2\vec{Q}^{n,3}}{\Delta t} - \vec{\mathsf{R}}^{n,3} - \vec{W}_\Gamma \circ \vec{f}^{n,4}, \tag{3.16}$$

each stage of which has a single unknown semi-discrete vector $\vec{Q}^{n,s}$, which can be solved for in the usual way for explicit RK schemes given the $\vec{\mathsf{M}} \left[\vec{Q}, \vec{f}\right] = 0$ condition of (3.15). This particular form is useful for

21

our objectives. In (3.16), $\vec{Q}^{0,4}$ is the known initial state $\vec{Q}^0$ with $\vec{\mathsf{R}}^{0,4} = \vec{\mathsf{R}}\left[\vec{Q}^0\right](t_0)$. For $n > 1$, $\vec{Q}^{n-1,4}$ is the numerical approximation of $\vec{Q}(t^n)$, and the sub-step values are $\vec{Q}^{n,s}$ for $n = 1, 2, \ldots, N_t$ and $s = 1, 2, 3$. $\vec{\mathsf{R}}^{n,s}$ denotes $\vec{\mathsf{R}}\left[\vec{Q}^{n,s}\right](t_n + c_s\Delta t)$, where $c_1 = c_2 = 1/2$ and $c_3 = c_4 = 1$.

To derive the fully discrete analog of (2.5), we introduce the notation $\tilde{f}$ for a vector with components $\vec{f}^{1,1}, \ldots, \vec{f}^{N_t,4}$. In total, $\tilde{f}$ consists of $20N^3N_t$ elements for a three-dimensional problem with 5 state variables and our choice of a 4-stage time-integration scheme. Thus, for $\tilde{f}, \tilde{g} \in \mathbb{R}^{20N^3N_t}$, we define the inner product

$$\left\langle \tilde{f}, \tilde{g} \right\rangle_{\hat{\mathbf{P}}} = \sum_{n=1}^{N_t} \sum_{s=1}^{4} \beta^{n,s} \Delta t \left(\vec{f}^{n,s}\right)^{\mathrm{T}} \left\{ I_5 \otimes \left(\hat{\mathbf{J}}^{-1}\hat{\mathbf{P}}\right) \right\} \vec{g}^{n,s}, \tag{3.17}$$

and the corresponding norm $\left\|\tilde{f}\right\|_{\hat{\mathbf{P}}}^2 = \left\langle \tilde{f}, \tilde{f} \right\rangle_{\hat{\mathbf{P}}}$. The values of $\beta^{n,s}$ are derived in Section 4.4 such that (3.17) defines a positive-definite inner product and is a consistent approximation of (2.5). The final result is $\beta^{n,1} = \beta^{n,4} = 1/6$ and $\beta^{n,2} = \beta^{n,3} = 1/3$ for $n = 1, 2, \ldots, N_t$. In general, this choice would lead to an $\mathcal{O}(\Delta t)$ integration scheme in time, which would obviously not be favorable if used simply as such, but as used it provides the exact adjoint. It is obviously different than application of a time-reversed analoge of the same time-forward Runge–Kutta scheme.

We emphasize that the notation $\tilde{f}$ for a fully discrete vector is simply a mathematical tool to express the algebraic equations resulting from spatial and temporal discretization of the predicive model IBVP. In practice, the numerical solver does not store all components of $\tilde{f}$ simultaneously in memory. The fully discretized governing equations have been written in the form (3.16), but are solved for in the usual manner of explicit multi-stage time marching schemes. We later show how the fully discrete adjoint equations can also be written in the same way. With this notation, the fully discretized equations can be compactly expressed as

$$\tilde{\mathsf{M}}\left[\tilde{Q}, \tilde{f}\right] \equiv \tilde{\mathsf{N}}\left[\tilde{Q}\right] - \tilde{W}_\Gamma \circ \tilde{f} = 0. \tag{3.18}$$

Chapter 4

Adjoint Formulations

This chapter describes in detail the adjoint formulations corresponding to the continuous, semi-discrete and fully discrete flow equations. A fully discrete adjoint is derived using the RK4 scheme as an example for integrating the semi-discrete flow equations. The approach for the continuous and semi-discrete adjoint formulations is similar, with the main difference arising due to the following property.

Property 4.1. Let U be the subspace of S whose elements satisfy the linearized boundary conditions. We restrict the domain of $\delta\mathcal{R}\left[Q;\delta Q\right]$ to $\left[H^1\left(\mathbb{R}_0^+\right)\times H^2\left(\overline{\mathbb{D}}\right)\right]^5\times U$. Then, $\delta\mathcal{R}\left[Q;\delta Q\right]:\mathrm{dom}\left(\delta\mathcal{R}\right)\to V^5$ is a densely defined unbounded operator. On the other hand, $\delta\vec{\mathsf{R}}\left[\vec{Q};\delta\vec{Q}\right]$ is local in time, and is essentially a bounded linear operator defined on $\mathbb{R}^{5N^3}\times\mathbb{R}^{5N^3}$ at each $t\in[0,\infty)$.

A consequence of this property is that while the semi-discrete adjoint operator is always well-defined for the system of ODEs obtained after spatial discretization of the equations governing the flow, the continuous-adjoint operator may not be defined for some choices of functionals. For example, consider the functional

$$\mathcal{J}\left[Q\right]=\int_{t=0}^{\infty}\int_{\boldsymbol{x}\in\mathbb{D}_p}\frac{\partial^2\omega_i}{\partial x_i^2}W_{\Omega}d^3\boldsymbol{x}dt, \tag{4.1}$$

which represents the vorticity diffusion integrated over a target region of interest. There is no continuous-adjoint equation corresponding to this functional.

4.1 Continuous-adjoint Formulation

Definition 4.1. For a functional $\mathcal{J}\left[Q\right]$ defined according to (2.14), the continuous-adjoint operator is $\mathcal{R}^\dagger\left[Q,Q^\dagger\right]:\mathrm{dom}\left(\mathcal{R}^\dagger\right)\to V^5$, where

$$\mathrm{dom}\left(\mathcal{R}^\dagger\right)=\Big\{(Q,Q^*)\in\left[H^1\left(\mathbb{R}_0^+\right)\times H^2\left(\overline{\mathbb{D}}\right)\right]^5\times V^5:$$

$$\text{there exists } \mathcal{R}^*\left[Q,Q^*\right]\in V^5 \text{ so that}$$

$$\left\langle\mathcal{R}^*\left[Q,Q^*\right],\delta Q\right\rangle=\left\langle Q^*,\delta\mathcal{R}\left[Q;\delta Q\right]\right\rangle+\delta\mathcal{J}\left[Q;\delta Q\right],\ \forall\delta Q\in U\Big\}. \tag{4.2}$$

If such an $\mathcal{R}^*[Q, Q^*]$ exists, then it is unique and we define

$$\mathcal{R}^\dagger [Q, Q^\dagger] := \mathcal{R}^* [Q, Q^\dagger], \ \forall Q^\dagger \in \text{dom} \left(\mathcal{R}^\dagger \right).$$

$Q^\dagger$ is called the adjoint variable.

This definition automatically restricts the domain of the continuous-adjoint operator to a subspace of $\left[H^1 \left(\mathbb{R}_0^+ \right) \times H^2 \left(\overline{\mathbb{D}} \right) \right]^5$ in which the continuous-adjoint boundary conditions are satisfied. Expanding the inner product in (4.2) using (2.5), integrating by parts, and using the definition of $\mathcal{J}[Q]$ from (2.14), we obtain the following condition for the existence of $\mathcal{R}^*[Q, Q^*]$:

$$Q^{*\text{T}} \left(\mathcal{A}_\alpha [Q] \, \delta Q - \mathcal{B}_{\alpha i} [Q] \, \frac{\partial}{\partial \xi_i} \left(\mathcal{C} [Q] \, \delta Q \right) \right)$$
$$+ \left(\frac{\partial Q^*}{\partial \xi_i} \right)^\text{T} \mathcal{B}_{i\alpha} [Q] \, \mathcal{C} [Q] \, \delta Q = \pm \delta \mathcal{K}_S [Q; \delta Q], \ \boldsymbol{\xi} \in B_\alpha^\pm, \ t \geq 0, \tag{4.3}$$

where $\mathcal{A}_\alpha [Q]$, $\mathcal{B}_{\alpha i} [Q]$ and $\mathcal{C} [Q]$ are defined in (A.4). The continuous-adjoint operator is

$$\mathcal{R}^\dagger [Q, Q^\dagger] = J \left\{ \mathcal{A}_i^\text{T} [Q] \, \frac{\partial Q^\dagger}{\partial \xi_i} + \mathcal{C}^\text{T} [Q] \, \frac{\partial}{\partial \xi_j} \left(\mathcal{B}_{ij}^\text{T} [Q] \, \frac{\partial Q^\dagger}{\partial \xi_i} \right) \right\} + \left(\frac{\delta \mathcal{K}_V}{\delta Q} [Q] \right)^\text{T}, \tag{4.4}$$

where $\frac{\delta \mathcal{K}_V}{\delta Q} [Q]$ is the Fréchet derivative of $\mathcal{K}_V [Q]$ defined implicitly using

$$\delta \mathcal{K}_V [Q; \delta Q] = \frac{\delta \mathcal{K}_V}{\delta Q} [Q] \, \delta Q.$$

The choice of the quantity of interest $\mathcal{J}[Q]$ is key to the existence of the continuous-adjoint operator. Boundary conditions for $Q^\dagger$ are obtained by substituting the corresponding flow boundary conditions for Q into (4.3). A detailed discussion and the specific procedures used to implement these are given in Chapter 5. In Table 4.1, we summarize the minimal set of boundary conditions for $Q^\dagger$ obtained when $\mathcal{K}_S [Q] = 0$, such that the quantity of interest can be expressed as a volume integral over the computational domain. Under this assumption, $\delta \mathcal{R} [Q; \delta Q]$ and $\mathcal{R}^\dagger [Q, Q^\dagger]$ satisfy a generalized Green's identity, and it can be easily verified that the surface term becomes identically zero due to (4.3). The boundary conditions for $Q^\dagger$ are homogeneous, and the non-trivial forcing term $\frac{\delta \mathcal{K}_V}{\delta Q} [Q]$ triggers the unsteady evolution of the adjoint field. An example that we consider in some detail measures radiated noise as

$$\mathcal{J}[Q] = \int_{t=0}^\infty \int_{\boldsymbol{\xi} \in \mathbb{D}} [p(\boldsymbol{\xi}, t) - \overline{p}(\boldsymbol{\xi})]^2 \, W_\Omega (\boldsymbol{\xi}, t) \, \frac{1}{J(\boldsymbol{\xi})} d^3 \boldsymbol{\xi} dt,$$

24

Boundary type	Flow boundary condition $\boldsymbol{\xi} \in B_\alpha^\pm,\ t \geq 0$	Adjoint boundary conditions $\boldsymbol{\xi} \in B_\alpha^\pm,\ t \geq 0$
Impermeable wall	$\hat{u}_\alpha \equiv \sum_{i=1}^3 \hat{\mathrm{M}}_{\alpha i} u_i = 0$	$\sum_{i=1}^3 \hat{\mathrm{M}}_{\alpha i} Q_{i+1}^\dagger = 0$
Isothermal no-slip wall	$u_1 = u_2 = u_3 = T = 0$	$Q_2^\dagger = Q_3^\dagger = Q_4^\dagger = Q_5^\dagger = 0$
Inflow/outflow	$\mathcal{A}_\alpha^{I\mp}\left[Q_t\right]\left(Q - Q_t\right)$ $-\mathrm{M}_{\alpha i}\left(\mathcal{F}_i^V\left[Q\right] - \mathcal{F}_i^V\left[Q_t\right]\right) = 0$	$\left(\mathcal{A}_\alpha^{I\pm}\left[Q_t\right]\right)^\mathrm{T} Q^\dagger$ $+\mathcal{C}^\mathrm{T}\left[Q\right]\mathcal{B}_{i\alpha}^\mathrm{T}\left[Q\right]\frac{\partial Q^\dagger}{\partial \xi_i} = 0$

Table 4.1: Physical boundary conditions and corresponding continuous-adjoint boundary conditions for a functional of the form (2.14) with $\mathcal{K}_S\left[Q\right] = 0$.

where $\bar{p}\left(\boldsymbol{\xi}\right)$ is the time-averaged mean pressure, and $W_\Omega\left(\boldsymbol{\xi},t\right)$ has support in a target region where the acoustic intensity is of interest $\Omega \subseteq \mathbb{D}$ over a time horizon $0 \leq t_0 \leq t \leq t_1$. In this case, the forcing term is

$$\left(\frac{\delta \mathcal{K}_V}{\delta Q}\left[Q\right]\right)^\mathrm{T} = 2\left[p\left(\boldsymbol{\xi},t\right) - \bar{p}\left(\boldsymbol{\xi}\right)\right] \begin{bmatrix} \frac{\gamma-1}{2} u_i u_i \\ -\left(\gamma - 1\right) u_1 \\ -\left(\gamma - 1\right) u_2 \\ -\left(\gamma - 1\right) u_3 \\ \gamma - 1 \end{bmatrix} W_\Omega\left(\boldsymbol{\xi},t\right).$$

On the other hand, if $\mathcal{K}_V\left[Q\right] = 0$, the forcing term vanishes and the boundary conditions for $Q^\dagger$ are inhomogeneous due to a non-trivial $\mathcal{K}_S\left[Q\right]$. We will consider two examples of such a functional with application to wall-bounded flows.

First, we look at pressure-induced force exterted by the flow on a boundary surface $B_\alpha^\pm$ projected along a fixed vector $\mathbf{k}$:

$$\mathcal{J}\left[Q\right] = -\int_{t=t_0}^{t_1}\int_{B_\alpha^\pm}\left[p\left(\boldsymbol{\xi},t\right) - p_\infty\right] k_i \mathrm{M}_{\alpha i} d^2\boldsymbol{\xi} dt, \tag{4.5}$$

where $B_\alpha^\pm$ is defined in (2.4). Drag and lift forces can be measured in this way, for example, by choosing $\mathbf{k}$ to be oriented along and normal to an ambient flow direction, respectively. If $B_\alpha^\pm$ is an impenetrable wall and we drop the viscous terms in (4.3), this leads to a single boundary condition

$$\sum_{i=1}^3 \hat{\mathrm{M}}_{\alpha i} Q_{i+1}^\dagger = \mp \sum_{i=1}^3 \hat{\mathrm{M}}_{\alpha i} \hat{k}_i,\ \boldsymbol{\xi} \in B_\alpha^\pm,\ t_0 \leq t \leq t_1. \tag{4.6}$$

If $B_\alpha^\pm$ is a no-slip wall, there are no boundary conditions for $Q^\dagger$ that satisfy (4.3). Hence, the continuous-adjoint operator is not defined for this choice of flow boundary conditions and functional.

Next, we examine viscous drag measured on $B_\alpha^\pm$ projected along the $\mathbf{k}$ direction:

$$\mathcal{J}[Q] = \int_{t=t_0}^{t_1} \int_{B_\alpha^\pm} \tau_{ij} k_i \mathrm{M}_{\alpha j} d^2 \boldsymbol{\xi} dt. \tag{4.7}$$

If $B_\alpha^\pm$ is a no-slip wall, the continuous-adjoint operator is defined iff $k_i \mathrm{M}_{\alpha i} = 0$. For this choice of $\mathbf{k}$, the continuous-adjoint boundary conditions are

$$Q_{i+1}^\dagger = \mp k_i, \text{ and } Q_5^\dagger = 0. \tag{4.8}$$

4.2   Optimal Control Theory

As a specific example of the application of our adjoint formulations, we consider the optimization of a control that minimizes a functional, such as (2.14). To do this, we pose the problem as a constrained minimization of the objective functional $\mathcal{J}[Q]$ by determining vector fields $Q(\boldsymbol{\xi}, t)$ and $f(\boldsymbol{\xi}, t)$ such that $\mathcal{M}[Q, f] = 0$, the constraint that enforces adherence to the governing equations. This is most easily formulated using Lagrange multipliers. We define the Lagrangian

$$\mathcal{L}[Q, Q^\dagger, f] = \mathcal{J}[Q] - \langle Q^\dagger, \mathcal{M}[Q, f] \rangle, \ \forall Q, Q^\dagger, f \in \left[H^1\left(\mathbb{R}_0^+\right) \times H^2\left(\overline{\mathbb{D}}\right)\right]^5$$

where the adjoint variable $Q^\dagger(\boldsymbol{\xi}, t)$ serves as the Lagrange multiplier, and the inner product is defined in (2.5). The extrema of the Lagrangian are obtained by setting its partial variations with respect to the independent variables $Q(\boldsymbol{\xi}, t)$, $f(\boldsymbol{\xi}, t)$ and $Q^\dagger(\boldsymbol{\xi}, t)$ to zero. This leads to the system of equations

$$\delta \mathcal{L}_Q \left[Q, Q^\dagger, f; \delta Q\right] \equiv \delta \mathcal{J}[Q] - \left\langle Q^\dagger, \delta \mathcal{N}[Q; \delta Q]\right\rangle = 0 \tag{4.9a}$$

$$\delta \mathcal{L}_{Q^\dagger} \left[Q, Q^\dagger, f; \delta Q^\dagger\right] \equiv -\left\langle \mathcal{M}[Q, f], \delta Q^\dagger\right\rangle = 0 \tag{4.9b}$$

$$\delta \mathcal{L}_f \left[Q, Q^\dagger, f; \delta f\right] \equiv \left\langle W_\Gamma \circ Q^\dagger, \delta f\right\rangle = 0, \tag{4.9c}$$

where (4.9b) and (4.9a) are the weak forms of the forward and adjoint equations, respectively, and (4.9c) is the condition that the gradient becomes identically zero at the extrema of the Lagrangian. This can be seen by linearizing (2.10) and using Definition 4.1 in (4.9a). The usual procedure for solving (4.9) involves first solving the forward equations for $Q(\boldsymbol{\xi}, t)$ using an initial guess $f^{(0)}(\boldsymbol{\xi}, t)$, then solving the adjoint equations for $Q^\dagger(\boldsymbol{\xi}, t)$ using as adjoint coefficients, the forward solution $Q^{(0)}(\boldsymbol{\xi}, t)$ obtained, followed by an iterative procedure to converge the residual of (4.9c) to zero by progressively improving the guess $f^{(n)}(\boldsymbol{\xi}, t)$ for $n > 0$.

We define the sensitivity gradient

$$\mathcal{G}\left[Q^\dagger\right](\boldsymbol{\xi},t) = W_\Gamma(\boldsymbol{\xi},t) \circ Q^\dagger(\boldsymbol{\xi},t).$$ (4.10)

Thus, converging the residual of (4.9c) to zero is equivalent to converging the norm of the sensitivity gradient $\left\|\mathcal{G}\left[Q^\dagger\right]\right\|$ to zero.

In our demonstration simulations, we use the Fletcher-Reeves-Polak-Ribiere conjugate gradient algorithm along with Brent's algorithm to optimize the control $f(\boldsymbol{\xi},t)$ [64]. During each iteration of the optimization, the conjugate gradient algorithm identifies a direction along which a line search is performed to determine the local minimum of $\mathcal{J}[Q]$ along that direction. Brent's algorithm accelerates this procedure. For the first iteration, the direction of line search is chosen along the negative gradient direction.

4.3   Semi-discrete Adjoint Formulation

Definition 4.2. The semi-discrete adjoint operator is defined using

$$\left\langle \vec{\mathsf{R}}^\dagger\left[\vec{Q},\vec{Q}^\dagger\right], \delta\vec{Q} \right\rangle_{\mathbf{P}} = \left\langle \vec{Q}^\dagger, \delta\vec{\mathsf{R}}\left[\vec{Q};\delta\vec{Q}\right] \right\rangle_{\mathbf{P}} + \delta\mathsf{J}\left[\vec{Q};\delta\vec{Q}\right],$$ (4.11)

where the inner product is defined in (3.1).

Using (3.14), (2.14) and (4.11), we get

$$\begin{aligned}
\vec{\mathsf{R}}^\dagger\left[\vec{Q},\vec{Q}^\dagger\right] = {} & \mathbf{J}\mathbf{A}_i^{\mathrm{T}}\left[\vec{Q}\right]\mathbf{D}_i\vec{Q}^\dagger + \mathbf{J}\mathbf{C}^{\mathrm{T}}\left[\vec{Q}\right]\mathbf{D}_j\mathbf{B}_{ij}^{\mathrm{T}}\left[\vec{Q}\right]\mathbf{D}_i\vec{Q}^\dagger \\
& + \mathbf{J}\sum_i \mathbf{D}\mathbf{I}_i\vec{Q}^\dagger + \vec{\mathsf{R}}_{\mathrm{SAT}}^\dagger\left[\vec{Q},\vec{Q}^\dagger\right] + \frac{\delta\mathsf{K}_V}{\delta\vec{Q}}\left[\vec{Q}\right],
\end{aligned}$$ (4.12)

where

$$\begin{aligned}
\vec{\mathsf{R}}_{\mathrm{SAT}}^\dagger\left[\vec{Q},\vec{Q}^\dagger\right] = {} & \mathbf{J}\mathbf{P}^{-1}\sum_{\alpha=1}^3 \left\{ \left(\mathbf{S}_{\mathrm{SAT},\alpha}^+\left[\vec{Q}\right] + \mathbf{S}_{\mathrm{SAT},\alpha}^-\left[\vec{Q}\right]\right)^{\mathrm{T}}\vec{Q}^\dagger \right. \\
& + \left(\mathbf{A}_\alpha^V\left[\vec{Q}\right] + \mathbf{B}_{\alpha i}\left[\vec{Q}\right]\mathbf{D}_i\mathbf{C}\left[\vec{Q}\right]\right)^{\mathrm{T}}\boldsymbol{\Delta}_\alpha\vec{Q}^\dagger \\
& - \boldsymbol{\Delta}_\alpha\left(\mathbf{A}_\alpha^I\left[\vec{Q}\right]\right)^{\mathrm{T}}\vec{Q}^\dagger - \boldsymbol{\Delta}_\alpha\mathbf{C}^{\mathrm{T}}\left[\vec{Q}\right]\mathbf{B}_{i\alpha}^{\mathrm{T}}\left[\vec{Q}\right]\mathbf{D}_i\vec{Q}^\dagger \\
& \left. + \left(\boldsymbol{\Delta}_\alpha^+ + \boldsymbol{\Delta}_\alpha^-\right)\frac{\delta\mathsf{K}_S}{\delta\vec{Q}}\left[\vec{Q}\right] \right\}.
\end{aligned}$$ (4.13)

We remark that $\vec{\mathsf{R}}_{\mathrm{SAT}}^\dagger\left[\vec{Q},\vec{Q}^\dagger\right]$ was not independently constructed as a penalty term to enforce the continuous-

adjoint boundary conditions. Rather, it is obtained automatically as the result of Definition 4.2. It is therefore, important to assess whether $\vec{\mathsf{R}}^{\dagger}_{\mathrm{SAT}}\left[\vec{Q},\vec{Q}^{\dagger}\right]$ is consistent with the continuous-adjoint boundary conditions. This forms the topic of Chapter 5.

4.4   Fully Discrete Adjoint Formulation

Recall the definition of the fully discrete inner product (3.17). As an example, we will demonstrate the formulation of a fully discrete adjoint using the RK4 scheme for integrating (3.15). To start with, we write (3.16) compactly as

$$\tilde{\mathsf{M}}\left[\tilde{Q},\tilde{f}\right] \equiv \tilde{\mathsf{N}}\left[\tilde{Q}\right] - \tilde{W}_{\Gamma} \circ \tilde{f} = 0.$$

The corresponding fully discrete adjoint equations are

$$\tilde{\mathsf{M}}^{\dagger}\left[\tilde{Q},\tilde{Q}^{\dagger},\tilde{g}_{\Omega}\right] \equiv \tilde{\mathsf{N}}^{\dagger}\left[\tilde{Q},\tilde{Q}^{\dagger}\right] - \tilde{W}_{\Omega} \circ \tilde{g}_{\Omega} = 0, \tag{4.14}$$

which are obtained using

$$\left\langle \tilde{Q}^{\dagger}, \delta\tilde{\mathsf{N}}\left[\tilde{Q},\delta\tilde{Q}\right]\right\rangle_{\mathbf{P}} = \left\langle \tilde{\mathsf{N}}^{\dagger}\left[\tilde{Q},\tilde{Q}^{\dagger}\right], \delta\tilde{Q}\right\rangle_{\mathbf{P}}. \tag{4.15}$$

The gradient of the objective functional is

$$\tilde{\mathsf{G}}\left[\tilde{Q}^{\dagger}\right] = \tilde{W}_{\Gamma} \circ \tilde{Q}^{\dagger}. \tag{4.16}$$

Using (3.16) and (3.17), we get

$$\vec{\mathsf{M}}^{\dagger n,4} = \frac{6\beta^{n,4}\vec{Q}^{\dagger n,4} + 2\beta^{n+1,4}\vec{Q}^{\dagger n+1,4} - \beta^{n+1,3}\vec{Q}^{\dagger n+1,3} - 2\beta^{n+1,2}\vec{Q}^{\dagger n+1,2} - 2\beta^{n+1,1}\vec{Q}^{\dagger n+1,1}}{\beta^{n,4}\Delta t}$$

$$- \frac{\beta^{n+1,1}}{\beta^{n,4}}\mathbf{P}^{-1}\mathbf{S}^{n,4}\mathbf{P}\vec{Q}^{\dagger n+1,1} - \vec{W}^{n,4}_{\Omega} \circ \vec{g}^{n,4}_{\Omega}$$

$$\vec{\mathsf{M}}^{\dagger n,3} = \frac{\beta^{n,3}\vec{Q}^{\dagger n,3} - 2\beta^{n,4}\vec{Q}^{\dagger n,4}}{\beta^{n,3}\Delta t} - \frac{\beta^{n,4}}{\beta^{n,3}}\mathbf{P}^{-1}\mathbf{S}^{n,3}\mathbf{P}\vec{Q}^{\dagger n,4} - \vec{W}^{n,3}_{\Omega} \circ \vec{g}^{n,3}_{\Omega}$$

$$\vec{\mathsf{M}}^{\dagger n,2} = \frac{2\beta^{n,2}\vec{Q}^{\dagger n,2} - 4\beta^{n,4}\vec{Q}^{\dagger n,4}}{\beta^{n,2}\Delta t} - \frac{\beta^{n,3}}{\beta^{n,2}}\mathbf{P}^{-1}\mathbf{S}^{n,2}\mathbf{P}\vec{Q}^{\dagger n,3} - \vec{W}^{n,2}_{\Omega} \circ \vec{g}^{n,2}_{\Omega}$$

$$\vec{\mathsf{M}}^{\dagger n,1} = \frac{2\beta^{n,1}\vec{Q}^{\dagger n,1} - 2\beta^{n,4}\vec{Q}^{\dagger n,4}}{\beta^{n,1}\Delta t} - \frac{\beta^{n,2}}{\beta^{n,1}}\mathbf{P}^{-1}\mathbf{S}^{n,1}\mathbf{P}\vec{Q}^{\dagger n,2} - \vec{W}^{n,1}_{\Omega} \circ \vec{g}^{n,1}_{\Omega} \tag{4.17}$$

for $n = 1, \ldots, N_t - 1$, where $\mathbf{S}^{n,s}$ is a matrix operator defined implicitly using

$$\delta\vec{\mathsf{R}}^{n,s} = \left(\mathbf{S}\left[\vec{Q}^{n,s}\right]\right)^{\mathrm{T}}\delta\vec{Q}^{n,s}. \tag{4.18}$$

For $n = N_t$, (4.17) holds except for the final sub-step of the final timestep $\vec{Q}^{\dagger N_t, 4} = (\Delta t / 6) \, \vec{W}_\Omega^{N_t, 4} \circ \vec{g}_\Omega^{N_t, 4}$. In (4.17), $\mathbf{S}\left[\vec{Q}^{n,s}\right]$ is the adjoint coefficient matrix and can be determined from (3.14). The superscripts on the adjoint coefficient matrix in (4.17) indicate that it is evaluated at the physical time at the end of the time-reversed sub-step, which is not restrictive since it only depends on the state variable available from the forward simulation. Hence, it is known at all times $t_0 \le t \le t_1$, though it may pose a data management challenge in practice.

As formulated, the coefficients $\beta^{n,s}$ provide a family of adjoint equations per the norm based on (3.17). However, to be useful for the control problem that we have formulated (or any corresponding objective), the fully discrete inner product (3.17) should provide a consistent approximation of an objective functional such as (2.14) with inner product such as (2.5). Note that in applications where it is more suitable to choose a discrete cost functional, this step is unnecessary. For our aeroacoustic demonstrations, the control and target mollifying support functions W_Γ and W_Ω, respectively, defined in Section 2.3, and their derivatives in time are chosen to be zero at the start and end of the control interval. Hence, we choose $\beta^{1,s} = \beta^{2,s} = \ldots = \beta^{N_t, s}$ while retaining enough flexibility to craft a fully discrete inner product (3.17) that is formally at least an $\mathcal{O}(\Delta t)$ approximation of the continuous inner product (2.5), but for the essentially homogeneous end conditions imposed by the specific W_Γ and W_Ω chosen for our demonstrations, its accuracy is effectively the same as pseudo-spectral integratrion. With this assumption, for the fully discrete norm to be consistent, $\sum_{s=1}^{4} \beta^{n,s} = 1$. Additionally, we require $\beta^{n,s} > 0$ to retain positive-definiteness.

Within the subset of discrete-adjoint time-marching schemes that satisfy the constraints imposed on the coefficients $\beta^{n,s}$, there is only one choice that is leads to an $\mathcal{O}(\Delta t)$ accurate quadrature rule: $\beta^{n,1} = \beta^{n,4} = 1/6$ and $\beta^{n,2} = \beta^{n,3} = 1/3$. The resulting fully discrete-adjoint time-marching scheme is

$$\vec{\mathsf{M}}^{\dagger n, 4} = \frac{6\vec{Q}^{\dagger n,4} + 2\vec{Q}^{\dagger n+1,4} - 2\vec{Q}^{\dagger n+1,3} - 4\vec{Q}^{\dagger n+1,2} - 2\vec{Q}^{\dagger n+1,1}}{\Delta t}$$

$$- \boxed{\mathbf{P}^{-1}\mathbf{S}^{n,4}\mathbf{P}} \, \vec{Q}^{\dagger n+1,1} - \vec{W}_\Omega^{n,4} \circ \vec{g}_\Omega^{n,4}$$

$$\vec{\mathsf{M}}^{\dagger n,3} = \frac{2\vec{Q}^{\dagger n,3} - 2\vec{Q}^{\dagger n,4}}{\Delta t} - \boxed{\mathbf{P}^{-1}\mathbf{S}^{n,3}\mathbf{P}} \, \vec{Q}^{\dagger n,4} - \boxed{2}\,\vec{W}_\Omega^{n,3} \circ \vec{g}_\Omega^{n,3}$$

$$\vec{\mathsf{M}}^{\dagger n,2} = \frac{2\vec{Q}^{\dagger n,2} - 2\vec{Q}^{\dagger n,4}}{\Delta t} - \boxed{\mathbf{P}^{-1}\mathbf{S}^{n,2}\mathbf{P}} \, \vec{Q}^{\dagger n,3} - \vec{W}_\Omega^{n,2} \circ \vec{g}_\Omega^{n,2}$$

$$\vec{\mathsf{M}}^{\dagger n,1} = \frac{\vec{Q}^{\dagger n,1} - \vec{Q}^{\dagger n,4}}{\Delta t} - \boxed{\mathbf{P}^{-1}\mathbf{S}^{n,1}\mathbf{P}} \, \vec{Q}^{\dagger n,2} - \boxed{\frac{1}{2}}\,\vec{W}_\Omega^{n,1} \circ \vec{g}_\Omega^{n,1} \tag{4.19}$$

for $n = 1, \ldots, N_t$ except $\vec{Q}^{\dagger N_t, 4} = \boxed{(\Delta t / 6) \, \vec{W}_\Omega^{N_t, 4} \circ \vec{g}_\Omega^{N_t, 4}}$.

Some terms are boxed in (4.19) to emphasize the difference from approximating the time derivative

in (3.15) with the RK4 method directly,

$$\vec{\mathsf{M}}^{\dagger n,4} = \frac{6\vec{Q}^{\dagger n,4} + 2\vec{Q}^{\dagger n+1,4} - 2\vec{Q}^{\dagger n+1,3} - 4\vec{Q}^{\dagger n+1,2} - 2\vec{Q}^{\dagger n+1,1}}{\Delta t}$$
$$- \mathbf{S}^{n+1,1}\vec{Q}^{\dagger n+1,1} - \vec{W}_\Omega^{n,4} \circ \vec{g}_\Omega^{n,4}$$
$$\vec{\mathsf{M}}^{\dagger n,3} = \frac{2\vec{Q}^{\dagger n,3} - 2\vec{Q}^{\dagger n,4}}{\Delta t} - \mathbf{S}^{n,4}\vec{Q}^{\dagger n,4} - \vec{W}_\Omega^{n,3} \circ \vec{g}_\Omega^{n,3}$$
$$\vec{\mathsf{M}}^{\dagger n,2} = \frac{2\vec{Q}^{\dagger n,2} - 2\vec{Q}^{\dagger n,4}}{\Delta t} - \mathbf{S}^{n,3}\vec{Q}^{\dagger n,3} - \vec{W}_\Omega^{n,2} \circ \vec{g}_\Omega^{n,2}$$
$$\vec{\mathsf{M}}^{\dagger n,1} = \frac{\vec{Q}^{\dagger n,1} - \vec{Q}^{\dagger n,4}}{\Delta t} - \mathbf{S}^{n,2}\vec{Q}^{\dagger n,2} - \vec{W}_\Omega^{n,1} \circ \vec{g}_\Omega^{n,1} \tag{4.20}$$

for $n = 1, \ldots, N_t$ except $\vec{Q}^{\dagger N_t,4} = 0$. Our choice of the coefficients $\beta^{n,s}$ in (4.17) facilitates a straightforward implementation, requiring only these changes from an RK4 discretization of the continuous-adjoint equations. This similarity is a key advance of our formulation. We anticipate that these differences can be eliminated by using an SBP time integration scheme [59]. All SBP time integration schemes are implicit schemes, and their efficient practical implementation poses additional challenges including potentially significant memory overhead, and designing effective preconditioners that are parallelizable.

4.5   Checkpointing

A practical matter when implementing an adjoint solver involves data management. The conserved variables appear in the adjoint equations as coefficients and must be stored when the forward problem is solved. For large problem sizes, some sort of checkpointing approach is necessary to provide sufficient storage space [26]. The explicit formulation for the flow state coefficients at the sub-steps is a key result; there is no such specification in the continuous adjoint formulation. The RK4 scheme (for example) does not provide a fourth-order estimate of the state at fractional sub-steps such as $t_{n+1/2}$. In this case, a consistent approach is to regard the stored values as available data points and interpolate to obtain the sub-step values of the state variable. For our demonstrations, when solving the continuous-adjoint equations, $\vec{Q}(t_n)$, $\vec{Q}(t_n + \Delta t)$, $\frac{d\vec{Q}}{dt}(t_n)$, and $\frac{d\vec{Q}}{dt}(t_n + \Delta t)$ are interpolated with cubic Hermite polynomials.

For solving the discrete-adjoint equations (4.19), we use a uniform checkpointing approach. In this approach, we choose a fixed checkpointing interval or frequency, say N_c timesteps, at which the conserved variables are written to disk during the forward simulation. During the adjoint simulation, the conserved variables at time $t = t_{n-N_c}$ are read from disk, and used as initial condition to integrate the forward equations from $t = t_{n-N_c}$ to $t = t_n$, with all intermediate sub-step values stored in memory. The adjoint

equations are then integrated in reverse time from $t = t_n$ to $t = t_{n-N_c}$ by computing the adjoint coefficients from the conserved variables that are available in memory. In this way, the adjoint simulation proceeds backwards in time up to $t = t_0$. Thus, our checkpointing strategy effectively involves repeating the same operations involved in solving the forward equations, during the adjoint simulation. Additional care is required in situations where random numbers are generated during the forward simulation, for example, to generate disturbances at an inflow. Our strategy is to generate pseudo-random numbers using a seed value, and ensure that the same seed value is used again when re-solving the forward equations during the checkpointing procedure.

An advantage of this checkpointing approach is that it involves the least possible number of re-evaluations of the primal RHS, which is typically relatively more expensive than a single read-write operation of a semi-discrete vector $\vec{Q}^{n,s}$ from memory. The numerical solver used for our demonstration simulations is designed for scalability and is based on a distributed memory model, so that the number of elements of $\vec{Q}^{n,s}$ that are locally owned by a single process for $n = 1, 2, \ldots, N_c$ and $s = 1, 2, 3, 4$ typically fits in the L1 cache, further reducing the overhead of a read-write operation from memory. On the other hand, evaluating the primal RHS involves communication of data corresponding to ghost or halo points between all neighboring processes, which is an expensive operation. In situations where evaluating the primal RHS is relatively less expensive, or the total available disk storage is low, Griewank and Corliss [26] proposed an optimal checkpointing schedule that may be more suitable. Wang et al. [88] proposed a dynamic checkpointing algorithm which is applicable in situations where the total number of time steps is not known beforehand.

There is a tradeoff in the choice of N_c, the frequency at which the conserved variables are written to disk during the forward simulation. Writing a semi-discrete vector $\vec{Q}^{n,s}$ to disk is an expensive operation and frequently writing the conserved variables to disk requires more storage, both of which suggest that choosing a larger value of N_c is more efficient. However, a large value of N_c may cause frequent cache misses when the intermediate sub-steps are read from memory during the adjoint simulation. Due to lack of proper guidance in optimizing the value of N_c for specific computing architectures, we set its value for individual simulations based on experience.

Chapter 5

Boundary Conditions and Dual Consistency

In this chapter, we consider the selection of dual-consistent SATs for enforcing boundary conditions. First, we provide a formal definition of dual-consistency.

Definition 5.1. The semi-discrete approximation (3.12) is called strongly dual-consistent up to order $q \in \mathbb{N}$ iff

$$\left\| \vec{\mathsf{R}}^\dagger \left[\vec{Q}_b, \vec{Q}_b^\dagger \right] - \text{proj} \left(\mathcal{R}^\dagger \left[Q_b, Q_b^\dagger \right] \right) \right\|_\infty = \mathcal{O}\left(h^q \right), \tag{5.1}$$

for all $Q_b, Q_b^\dagger \in \left[H^1 \left(\mathbb{R}_0^+ \right) \times H^2 \left(\overline{\mathbb{D}} \right) \right]^5$ such that $Q_b \left(\boldsymbol{\xi}, t \right)$ and $Q_b^\dagger \left(\boldsymbol{\xi}, t \right)$ satisfy the boundary conditions on $\partial \mathbb{D}$. It is called weakly dual-consistent up to order $q \in \mathbb{N}$ iff

$$\left\langle \vec{\mathsf{R}}^\dagger \left[\vec{Q}_b, \vec{Q}_b^\dagger \right] - \text{proj} \left(\mathcal{R}^\dagger \left[Q_b, Q_b^\dagger \right] \right), \delta \vec{Q}_b \right\rangle_{\mathbf{P}} = \mathcal{O}\left(h^q \right), \tag{5.2}$$

for all $\delta Q_b \in \left[H^1 \left(\mathbb{R}_0^+ \right) \times H^2 \left(\overline{\mathbb{D}} \right) \right]^5$ such that $\delta Q_b \left(\boldsymbol{\xi}, t \right)$ satisfies the linearized boundary conditions on $\partial \mathbb{D}$. A discretization that is strongly dual-consistent is also weakly dual-consistent, but the converse is not necessarily true.

The following lemma simplifies the analysis of dual-consistency.

Lemma 5.2. *Let s be the order of accuracy of boundary stencils used in the SBP derivative operators in (3.12). The semi-disrcetization (3.12) is strongly dual-consistent up to order $s \in \mathbb{N}$ according to (5.1) if*

$$\left\| \vec{\mathsf{R}}_{\text{SAT}}^\dagger \left[\vec{Q}_b, \vec{Q}_b^\dagger \right] \right\|_\infty = \mathcal{O}\left(h^s \right).$$

It is weakly dual-consistent according to (5.2) if

$$\left\langle \vec{\mathsf{R}}_{\text{SAT}}^\dagger \left[\vec{Q}_b, \vec{Q}_b^\dagger \right], \delta \vec{Q}_b \right\rangle_{\mathbf{P}} = \mathcal{O}\left(h^s \right).$$

Proof. The proof is straightforward and we only provide an outline here. For proving strong dual-consistency, we add and subtract $\vec{\mathsf{R}}_{\text{SAT}}^\dagger \left[\vec{Q}_b, \vec{Q}_b^\dagger \right]$ inside the norm in (5.1) and use the triangle inequality. For weak dual-

consistency, we add and subtract $\vec{\mathsf{R}}^{\dagger}_{\text{SAT}} \left[\vec{Q}_b, \vec{Q}^{\dagger}_b \right]$ to $\vec{\mathsf{R}}^{\dagger} \left[\vec{Q}_b, \vec{Q}^{\dagger}_b \right]$ in (5.2) and invoke linearity of the inner product. The proof for both cases then follows from use of Lemma 3.1. $\square$

Remark 5.3. The use of SBP discrete derivative operators and the artificial dissipation operator (3.7) allows us to pose the dual-consistency requirement in Definition 5.1 as a condition on the SATs used to enforce the boundary conditions only. This would not have been possible, for example, with discrete derivative operators that do not satisfy an SBP rule or with artificial dissipation based on low pass filters.

For the following analysis, we assume that a specific boundary condition is enforced on the $\boldsymbol{\xi} \in B^{\pm}_{\alpha}$ face of the unit cube computational domain $\mathbb{D}$, and ignore the other faces without loss of generality. The superscript $\pm$ allows us to simultaneously write the boundary conditions for both B^+_{α} and B^-_{α} using a single equation.

5.1   Inflows and Outflows

To model inflows and outflows, we use approximate characteristic boundary conditions based on a linearization of the governing equations. In our simulations, we will supply boundary data through a stationary target solution $Q_t(\mathbf{x})$, selected such that when transformed to characteristic variables, the perturbation $Q(\mathbf{x}, t) - Q_t(\mathbf{x})$ satisfies the condition

$$\mathcal{A}^{I\mp}_{\alpha} [Q_t] (Q - Q_t) - \mathrm{M}_{\alpha i} \left(\mathcal{F}^V_i [Q] - \mathcal{F}^V_i [Q_t] \right) = 0, \ \boldsymbol{\xi} \in B^{\pm}_{\alpha}, \ t \geq 0, \tag{5.3}$$

which is accurate up to $\mathcal{O}(\|Q - Q_t\|)$. This is common practice for highly non-reflecting boundary conditions [24, 37], but has the obvious challenge of properly selecting the target solution. Linearizing (5.3) with respect to $Q(\boldsymbol{\xi}, t)$, we obtain

$$\left(\mathcal{A}^{I\mp}_{\alpha} [Q_t] - \mathcal{A}^V_{\alpha} [Q] \right) \delta Q - \mathcal{B}_{\alpha j} [Q] \frac{\partial}{\partial \xi_j} \left(\mathcal{C} [Q] \delta Q \right) = 0, \ \boldsymbol{\xi} \in B^{\pm}_{\alpha}, \ t \geq 0. \tag{5.4}$$

A consistent SAT that enforces (5.3) is

$$\vec{\mathsf{R}}^{\pm}_{\text{SAT},\alpha} \left[\vec{Q} \right] = \pm \sigma^I \boldsymbol{\Delta}^{\pm}_{\alpha} \left(\mathbf{A}^{I\mp}_{\alpha} \left[\vec{Q}_t \right] + \tilde{\mathbf{A}}^{\mp}_{\alpha} \left[\vec{Q}_t \right] \right) \left(\vec{Q} - \vec{Q}_t \right)$$
$$\mp \sigma^V \boldsymbol{\Delta}^{\pm}_{\alpha} \mathbf{M}_{\alpha i} \left(\vec{\mathsf{F}}^V_i \left[\vec{Q} \right] - \vec{\mathsf{F}}^V_i \left[\vec{Q}_t \right] \right), \forall \vec{Q} \in V^5_h \tag{5.5}$$

where $\mathbf{A}_\alpha^{I\pm}\left[\vec{Q}\right] = \text{proj}\left(\tilde{A}_\alpha^{I\pm}[Q]\right)$, $\tilde{\mathbf{A}}_\alpha^\pm\left[\vec{Q}\right] = \text{proj}\left(\tilde{A}_\alpha^\pm[Q]\right)$,

$$
\tilde{A}_\alpha^+[Q] = \begin{cases} \mathcal{T}_\alpha[Q]\,\tilde{\Lambda}_\alpha^+[Q]\,\mathcal{T}_\alpha^{-1}[Q] & , \ 0 < -\hat{u}_\alpha < a \\ 0 & , \ \text{otherwise} \end{cases}
$$

$$
\tilde{A}_\alpha^-[Q] = \begin{cases} \mathcal{T}_\alpha[Q]\,\tilde{\Lambda}_\alpha^-[Q]\,\mathcal{T}_\alpha^{-1}[Q] & , \ 0 < \hat{u}_\alpha < a \\ 0 & , \ \text{otherwise,} \end{cases}
$$

$$
\tilde{\mathbf{\Lambda}}_\alpha^+\left[\vec{Q}\right] = -\text{proj}\left\{ \tilde{\mathrm{M}}_\alpha \begin{bmatrix} 0 & 0 & 0 & 0 & 0 \\ 0 & 0 & 0 & 0 & 0 \\ 0 & 0 & 0 & 0 & 0 \\ 0 & 0 & 0 & 0 & 0 \\ 0 & 0 & 0 & \hat{u}_\alpha + a & 0 \end{bmatrix} \right\}
$$

$$
\tilde{\mathbf{\Lambda}}_\alpha^-\left[\vec{Q}\right] = -\text{proj}\left\{ \tilde{\mathrm{M}}_\alpha \begin{bmatrix} 0 & 0 & 0 & 0 & 0 \\ 0 & 0 & 0 & 0 & 0 \\ 0 & 0 & 0 & 0 & 0 \\ 0 & 0 & 0 & 0 & \hat{u}_\alpha - a \\ 0 & 0 & 0 & 0 & 0 \end{bmatrix} \right\},
$$

and the condition for stability is, $\sigma^I > \frac{1}{2}$ and $\sigma^V = 1$ [79]. The columns of $\mathcal{T}_\alpha[Q]$ are the right eigenvectors of $\mathcal{A}_\alpha^I[Q]$, and the rows of $\mathcal{T}_\alpha^{-1}[Q]$ are the left eigenvectors of $\mathcal{A}_\alpha^I[Q]$. Their full expressions are given by Pulliam and Chaussee [65]. Similarly, linearizing (5.5) yields

$$
\mathbf{S}_{\text{SAT},\alpha}^\pm\left[\vec{Q}\right] = \pm\sigma^I \mathbf{\Delta}_\alpha^\pm \left(\mathbf{A}_\alpha^{I\mp}\left[\vec{Q}_t\right] + \tilde{\mathbf{A}}_\alpha^\pm\left[\vec{Q}_t\right] \right)
$$
$$
\mp \sigma^V \mathbf{\Delta}_\alpha^\pm \left(\mathbf{A}_\alpha^V\left[\vec{Q}\right] + \mathbf{B}_{\alpha i}\left[\vec{Q}\right]\mathbf{D}_i\mathbf{C}\left[\vec{Q}\right] \right), \tag{5.6}
$$

Svärd et al. [79] showed the existence of an energy estimate for the continuous and discrete problems with this approach using the principle of frozen coefficients, which indicates that it is well-posed for the continuous IBVP and stable for the discrete problem with respect to small-amplitude fluctuations, respectively.

A special case of (5.3) is a "far-field" physical boundary to model an infinite domain. In this case, the known ambient conditions are used to supply boundary data and the viscous term in (5.3) can be neglected. The result is the well-known locally one-dimensional inviscid (LODI) characteristic boundary conditions [63],

which have been successfully used in aeroacoustic simulations [14]. Additionally, we pad the boundary with a sponge layer, which serves as compact support for a forcing term

$$\mathcal{R}^{\pm}_{\text{sponge},\alpha}[Q] = -\sigma_{\text{sponge}} \left| 1 - \tilde{x}^{\perp}_{\alpha} \right|^2 (Q - Q_t), \tag{5.7}$$

that is added to the RHS of (2.6). The role of this forcing is to drive the solution near the boundaries towards the target state [22], thereby improving the asymptotic convergence of (5.3) for a nonlinear problem. In (5.7), $\sigma_{\text{sponge}} > 0$ is a constant scaling factor and $\tilde{x}^{\perp}_{\alpha}$ is the distance from the boundary measured along the curve perpendicular to the isosurfaces of ξ_{α}, and normalized so that $0 \leq \tilde{x}^{\perp}_{\alpha} \leq 1$ across the sponge layer. Thus, the damping strength is maximum for $\boldsymbol{\xi} \in B^{\pm}_{\alpha}$ and decreases quadratically to zero away from the boundary.

Theorem 5.4. *Let $\mathcal{J}[Q]$ be a functional of the form (2.14) with $\mathcal{K}_S[Q] = 0$. The semi-discrete approximation (3.12) with the SAT (5.5) for enforcing an inflow/outflow boundary condition (5.3) is strongly dual-consistent of order s' for some $s' > 0$ if $\sigma^I = \sigma^V = 1$. If $\vec{Q}_t = \text{proj}(Q_t)$ and $\vec{Q}_b = \text{proj}(Q_b)$, where Q_t is the prescribed target state in (5.3) and Q_b is a solution of (5.3), then s' is the maximum value for which*

$$\left\| \boldsymbol{\Delta}^{\pm}_{\alpha} \left(\vec{Q}_b - \vec{Q}_t \right) \right\|_{\infty} \sim \mathcal{O}\left(h^{s'} \right),$$

where $\sim$ denotes asymptotic equality.

Proof. Using the continuous-adjoint boundary conditions corresponding to an inflow/outflow physical boundary condition on $\boldsymbol{\xi} \in B^{\pm}_{\alpha}$, we get

$$\left(\mathbf{A}^{I\pm}_{\alpha} \left[\vec{Q}_t \right] - \tilde{\mathbf{A}}^{\mp}_{\alpha} \left[\vec{Q}_t \right] \right)^{\mathrm{T}} \vec{Q}^{\dagger}_b + \mathbf{C}^{\mathrm{T}} \left[\vec{Q}_b \right] \mathbf{B}^{\mathrm{T}}_{i\alpha} \left[\vec{Q}_b \right] \mathbf{D}_i \vec{Q}^{\dagger}_b = 0.$$

From (5.6) and (4.13), we get

$$\begin{aligned}
\vec{\mathsf{R}}^{\dagger}_{\text{SAT}} \left[\vec{Q}_b, \vec{Q}^{\dagger}_b \right] &= \mp \left(\sigma^V - 1 \right) \mathbf{J} \mathbf{P}^{-1} \left(\mathbf{A}^{V}_{\alpha} \left[\vec{Q}_b \right] + \mathbf{B}_{\alpha i} \left[\vec{Q}_b \right] \mathbf{D}_i \mathbf{C} \left[\vec{Q}_b \right] \right)^{\mathrm{T}} \boldsymbol{\Delta}^{\pm}_{\alpha} \vec{Q}^{\dagger}_b \\
&\quad \pm \left(\sigma^I - 1 \right) \mathbf{J} \mathbf{P}^{-1} \boldsymbol{\Delta}^{\pm}_{\alpha} \left(\mathbf{A}^{I\mp}_{\alpha} \left[\vec{Q}_t \right] + \tilde{\mathbf{A}}^{\mp}_{\alpha} \left[\vec{Q}_t \right] \right)^{\mathrm{T}} \vec{Q}^{\dagger}_b \\
&\quad \mp \mathbf{J} \mathbf{P}^{-1} \boldsymbol{\Delta}^{\pm}_{\alpha} \left(\mathbf{A}^{I}_{\alpha} \left[\vec{Q}_b \right] - \mathbf{A}^{I}_{\alpha} \left[\vec{Q}_t \right] \right)^{\mathrm{T}} \vec{Q}^{\dagger}_b.
\end{aligned}$$

For $\sigma^I = \sigma^V = 1$, the first two terms vanish. Further, $\boldsymbol{\Delta}^{\pm}_{\alpha} \mathbf{A}^{I}_{\alpha} \left[\vec{Q}_b \right] = \boldsymbol{\Delta}^{\pm}_{\alpha} \mathbf{A}^{I}_{\alpha} \left[\vec{Q}_e \right]$. Using a Taylor expansion of $\mathbf{A}^{I}_{\alpha} \left[\vec{Q}_e \right]$ about $\mathbf{A}^{I}_{\alpha} \left[\vec{Q}_t \right]$ leads to

$$\left\| \vec{\mathsf{R}}^{\dagger}_{\text{SAT}} \left[\vec{Q}_b, \vec{Q}^{\dagger}_b \right] \right\|_{\infty} = \mathcal{O}\left(h^{s'} \right),$$

35

The proof follows from Lemma 5.2. $\qquad\qquad\qquad\qquad\qquad\qquad\qquad\qquad\qquad\qquad\qquad\qquad\qquad$ $\square$

5.2 Impermeable Wall

At an impermeable wall, the normal component of velocity is set to zero:

$$\hat{u}_\alpha\left(\boldsymbol{\xi},t\right) \equiv \hat{\mathrm{M}}_{\alpha i}\left(\boldsymbol{\xi}\right)u_i\left(\boldsymbol{\xi},t\right) = 0,\ \boldsymbol{\xi}\in B_\alpha^\pm,\ t\geq 0. \tag{5.8}$$

This is a well-posed boundary condition for the compressible Euler equations [40], which are obtained from (2.6) by setting $F_i^V = 0$, $i = 1,2,3$. Svärd and Nordström [78] derived an SAT to enforce (5.8) and showed the existence of an energy estimate for the discrete problem. They noted that their specific form chosen for the construction of the penalty term is not unique. We will use a different form,

$$\vec{\mathsf{R}}_{\mathrm{SAT},\alpha}^\pm\left[\vec{Q}\right] = \pm\sigma^I\boldsymbol{\Delta}_\alpha^\pm\vec{\mathsf{Y}}_\alpha^I\left[\vec{Q}\right],\ \forall\vec{Q}\in V_h^5, \tag{5.9}$$

where

$$\vec{\mathsf{Y}}_\alpha^I\left[\vec{Q}\right] = \mathrm{proj}\left(\tilde{\mathrm{M}}_\alpha\begin{bmatrix}\rho\hat{u}_\alpha \\ \rho\hat{u}_\alpha u_1 \\ \rho\hat{u}_\alpha u_2 \\ \rho\hat{u}_\alpha u_3 \\ \rho\hat{u}_\alpha h\end{bmatrix}\right). \tag{5.10}$$

Our choice will be motivated by the discussion to follow in Theorem 5.5, where we show that the SAT 5.9 leads to a strongly dual-consistent discretization for functionals of the form (2.14) with $\mathcal{K}_S\left[Q\right]$ an arbitrary function of pressure. To prove stability for the SAT (5.9), we consider the linearized compressible Euler equations

$$\frac{\partial}{\partial t}\left(\delta Q\right) = \delta\mathcal{R}\left[Q;\delta Q\right],\quad \delta\mathcal{R}\left[Q;\delta Q\right] = -J\frac{\partial}{\partial\xi_i}\left(\mathcal{A}_i^I\left[Q\right]\delta Q\right).$$

We will follow the approach of Svärd and Nordström [78] and consider a single boundary B_α^- where an impermeable wall boundary condition $\hat{u}_\alpha \equiv \hat{\mathrm{M}}_{\alpha i}u_i = 0$ is to be enforced. The overall linearized semi-discrete problem is

$$\mathbf{J}^{-1}\frac{d}{dt}\left(\delta\vec{Q}\right) = -\mathbf{D}_i\mathbf{A}_i^I\left[\vec{Q}\right]\delta\vec{Q} + \sigma_{\mathrm{diss.}}\sum_i\mathbf{DI}_i\delta\vec{Q} + \mathbf{P}^{-1}\mathbf{S}_{\mathrm{SAT},\alpha}^-\left[\vec{Q}\right]\delta\vec{Q}, \tag{5.11}$$

where $\mathbf{S}_{\mathrm{SAT},\alpha}^{-}\left[\vec{Q}\right]$ is given by (5.13). Using the principle of frozen coefficients [40], we set $\vec{Q} = \vec{Q}_0$ and symmetrize (5.11) to obtain

$$\mathbf{J}^{-1}\frac{d}{dt}\left(\delta\vec{W}\right) = -\mathbf{D}_i\hat{\mathbf{A}}_i^I\left[\vec{Q}_0\right]\delta\vec{W} + \sigma_{\mathrm{diss.}}\sum_i\mathbf{D}\mathbf{I}_i\delta\vec{W} + \mathbf{P}^{-1}\hat{\mathbf{S}}_{\mathrm{SAT},\alpha}^{-}\left[\vec{Q}_0\right]\delta\vec{W},$$

where $\delta\vec{W} = \mathbf{\Sigma}\left[\vec{Q}_0\right]\delta\vec{Q}$,

$$\hat{\mathbf{A}}_i^I\left[\vec{Q}\right] = \mathbf{\Sigma}\left[\vec{Q}\right]\mathbf{A}_i^I\left[\vec{Q}\right]\left(\mathbf{\Sigma}\left[\vec{Q}\right]\right)^{-1}$$

$$\hat{\mathbf{S}}_{\mathrm{SAT},\alpha}^{-}\left[\vec{Q}\right] = \mathbf{\Sigma}\left[\vec{Q}\right]\mathbf{S}_{\mathrm{SAT},\alpha}^{-}\left[\vec{Q}\right]\left(\mathbf{\Sigma}\left[\vec{Q}\right]\right)^{-1},$$

and $\mathbf{\Sigma}\left[\vec{Q}\right] = \left(\mathbf{\Sigma}\left[\vec{Q}\right]\right)^{\mathrm{T}}$ is the symmetrizer. From the linearized boundary condition $\delta\hat{u}_\alpha = 0$, we can show that

$$\left(\hat{\mathbf{S}}_{\mathrm{SAT},\alpha}^{-}\left[\vec{Q}_0\right]\right)^{\mathrm{T}}\delta\vec{W} = -\sigma^I\hat{\mathbf{A}}_\alpha^I\left[\vec{Q}_0\right]\mathbf{\Delta}_\alpha^{-}\delta\vec{W}.$$

To assess the stability of the SAT (5.9), we consider the energy estimate

$$\frac{d}{dt}\left\|\delta\vec{W}\right\|_{\mathbf{P}}^2 = \left\langle\frac{d}{dt}\left(\delta\vec{W}\right), \delta\vec{W}\right\rangle_{\mathbf{P}} + \left\langle\delta\vec{W}, \frac{d}{dt}\left(\delta\vec{W}\right)\right\rangle_{\mathbf{P}}$$

$$= -\left(\delta\vec{W}\right)^{\mathrm{T}}\hat{\mathbf{A}}_i^I\left[\vec{Q}_0\right]\mathbf{\Delta}_i\delta\vec{W} + 2\sigma_{\mathrm{diss.}}\left(\delta\vec{W}\right)^{\mathrm{T}}\left(\mathbf{P}\sum_i\mathbf{D}\mathbf{I}_i\right)^{\mathrm{T}}\delta\vec{W}$$

$$+ 2\left(\delta\vec{W}\right)^{\mathrm{T}}\left(\hat{\mathbf{S}}_{\mathrm{SAT},\alpha}^{-}\left[\vec{Q}_0\right]\right)^{\mathrm{T}}\delta\vec{W}.$$

The term $\left(\delta\vec{W}\right)^{\mathrm{T}}\left(\mathbf{P}\sum_i\mathbf{D}\mathbf{I}_i\right)^{\mathrm{T}}\delta\vec{W}$ is dissipative and can be safely ignored. Dropping the terms in $\hat{\mathbf{A}}_i^I\left[\vec{Q}_0\right]\mathbf{\Delta}_i$ on all other boundaries and retaining only $-\hat{\mathbf{A}}_\alpha^I\left[\vec{Q}_0\right]\mathbf{\Delta}_\alpha^{-}$, we get

$$\frac{d}{dt}\left\|\delta\vec{W}\right\|_{\mathbf{P}}^2 = \left(1 - 2\sigma^I\right)\left(\delta\vec{W}\right)^{\mathrm{T}}\hat{\mathbf{A}}_\alpha^I\left[\vec{Q}_0\right]\mathbf{\Delta}_\alpha^{-}\delta\vec{W}.$$

An energy estimate exists for $\sigma^I > \frac{1}{2}$, which is the condition for stability.

Linearizing (5.8) and (5.9) yields

$$\delta\hat{u}_\alpha\left(\boldsymbol{\xi}, t\right) = 0,\ \boldsymbol{\xi} \in B_\alpha^{\pm},\ t \geq 0, \tag{5.12}$$

and

$$\mathbf{S}_{\mathrm{SAT},\alpha}^{\pm}\left[\vec{Q}\right] = \pm\sigma^I\boldsymbol{\Delta}_{\alpha}^{\pm}\left\{\mathbf{A}_{\alpha}^I\left[\vec{Q}\right] - \mathrm{proj}\left(\begin{bmatrix} 0 \\ \mathrm{M}_{\alpha 1} \\ \mathrm{M}_{\alpha 2} \\ \mathrm{M}_{\alpha 3} \\ 0 \end{bmatrix}\begin{bmatrix} \frac{\gamma-1}{2}u_i u_i \\ -(\gamma-1)u_1 \\ -(\gamma-1)u_2 \\ -(\gamma-1)u_3 \\ \gamma-1 \end{bmatrix}^{\mathrm{T}}\right)\right\}, \tag{5.13}$$

respectively.

Theorem 5.5. *Let $\mathcal{J}[Q]$ be a functional of the form (2.14) where $\mathcal{K}_V[Q]$ is arbitrary and $\mathcal{K}_S[Q]$ is a function of pressure only. Then, the semi-discrete approximation (3.12) with the SAT (5.9) for enforcing an impermeable wall boundary condition (5.8) is strongly dual-consistent of order s for $\sigma^I = 1$, where s is the order of accuracy of the boundary stencils of the diagonal-norm SBP operators in (3.12).*

Proof. Let $\mathcal{K}_S[Q] = \tilde{\mathcal{K}}_S[p]$, where $\tilde{\mathcal{K}}_S[p]$ is a (possibly trivial) nonlinear scalar-field valued functional of pressure. The continuous-adjoint boundary conditions corresponding to an impermeable wall physical boundary condition on $\boldsymbol{\xi} \in B_{\alpha}^{\pm}$ can be obtained from (4.3), and written

$$Q_i^{\dagger}\mathrm{M}_{\alpha i} = \pm\frac{\delta\tilde{\mathcal{K}}_s}{\partial p}[p], \; \boldsymbol{\xi} \in B_{\alpha}^{\pm}, \; t \geq 0. \tag{5.14}$$

Using (5.13) and retaining only the inviscid terms in (4.13) yields

$$\vec{\mathsf{R}}_{\mathrm{SAT}}^{\dagger}\left[\vec{Q},\vec{Q}^{\dagger}\right] = \pm\left(\sigma^I - 1\right)\mathbf{J}\mathbf{P}^{-1}\boldsymbol{\Delta}_{\alpha}^{\pm}\left(\mathbf{A}_{\alpha}^I\left[\vec{Q}\right]\right)^{\mathrm{T}}\vec{Q}^{\dagger}$$

$$\mp\sigma^I\mathbf{J}\mathbf{P}^{-1}\boldsymbol{\Delta}_{\alpha}^{\pm}\mathrm{proj}\left(\begin{bmatrix} \frac{\gamma-1}{2}u_i u_i \\ -(\gamma-1)u_1 \\ -(\gamma-1)u_2 \\ -(\gamma-1)u_3 \\ \gamma-1 \end{bmatrix}\begin{bmatrix} 0 \\ \mathrm{M}_{\alpha 1} \\ \mathrm{M}_{\alpha 2} \\ \mathrm{M}_{\alpha 3} \\ 0 \end{bmatrix}^{\mathrm{T}}\right)\vec{Q}^{\dagger}$$

$$+\mathbf{J}\mathbf{P}^{-1}\boldsymbol{\Delta}_{\alpha}^{\pm}\mathrm{proj}\left(\begin{bmatrix} \frac{\gamma-1}{2}u_i u_i \\ -(\gamma-1)u_1 \\ -(\gamma-1)u_2 \\ -(\gamma-1)u_3 \\ \gamma-1 \end{bmatrix}\frac{\delta\tilde{\mathcal{K}}_s}{\partial p}[p]\right)$$

for all $\vec{Q},\vec{Q}^{\dagger} \in V_h^5$. For $\sigma^I = 1$, the first term vanishes. Using (5.14), it is easily shown that $\vec{\mathsf{R}}_{\mathrm{SAT}}^{\dagger}\left[\vec{Q},\vec{Q}_b^{\dagger}\right] = 0$

for all $\vec{Q} \in V_h^5$, where $\vec{Q}_b^\dagger = \text{proj}\left(Q_b^\dagger\right)$ and $Q_b^\dagger(\boldsymbol{\xi}, t)$ satisfies (5.14). Again, the proof follows from Lemma 5.2.

$\square$

5.3   Isothermal Wall

For viscous flows, the fluid velocity at a wall satisfies a no-slip condition. We consider the case of a stationary isothermal wall, where the velocity components are zero and the temperature distribution is specified:

$$u_i(\boldsymbol{\xi}, t) = 0, \quad \text{and} \quad T(\boldsymbol{\xi}, t) = T_w(\boldsymbol{\xi}), \; \boldsymbol{\xi} \in B_\alpha^\pm, \; t \geq 0. \tag{5.15}$$

Using the principle of frozen coefficients [41], Svärd and Nordström [78] showed that this boundary condition leads to an energy estimate for the linearized problem. To enforce (5.15), we use an SAT of the form

$$\vec{\mathsf{R}}_{\text{SAT},\alpha}^\pm\left[\vec{Q}\right] = \pm\sigma^I \boldsymbol{\Delta}_\alpha^\pm \vec{\mathsf{Y}}_\alpha^I\left[\vec{Q}\right] - \sigma^V \boldsymbol{\Delta}_\alpha^\pm \vec{\mathsf{Y}}_\alpha^V\left[\vec{Q}\right], \; \forall \vec{Q} \in V_h^5, \tag{5.16}$$

where $\vec{\mathsf{Y}}_\alpha^I\left[\vec{Q}\right]$ is defined in (5.10) and

$$\vec{\mathsf{Y}}^V\left[\vec{Q}\right] = \text{proj}\begin{bmatrix} 0 & \rho u_1 & \rho u_2 & \rho u_2 & \rho E - \frac{\rho T_w}{\gamma} \end{bmatrix}^{\text{T}}.$$

Svärd and Nordström [78] derived a stability condition for an SAT whose form is identical to (5.16) except the inviscid contribution. Based on their analysis for the viscous penalty term, the condition for stability of the SAT (5.16) is $\sigma^I > \frac{1}{2}$ and $\sigma^V > \frac{1}{4\text{Re}} \max\left(\begin{bmatrix} \frac{\gamma}{\text{Pr}} & \frac{5}{3} \end{bmatrix}^{\text{T}} \otimes \hat{\mathbf{J}}\hat{\mathbf{P}}^{-1}\hat{\boldsymbol{\Delta}}_\alpha^\pm \text{proj}\left(\frac{\mu}{\rho}\right)\right)$, where $\max \vec{f}$ denotes the largest component of the semi-discrete vector $\vec{f}$.

Linearizing (5.15) and (5.16) yields

$$\delta u_i(\boldsymbol{\xi}, t) = 0, \quad \text{and} \quad \delta T(\boldsymbol{\xi}, t) = 0 \; \boldsymbol{\xi} \in B_\alpha^\pm, \; t \geq 0, \tag{5.17}$$

and

$$
\mathbf{S}_{\text{SAT},\alpha}^{\pm}\left[\vec{Q}\right] = \pm \sigma^I \boldsymbol{\Delta}_\alpha^{\pm} \left\{ \mathbf{A}_\alpha^I \left[\vec{Q}\right] - \text{proj} \left(\begin{bmatrix} 0 \\ \text{M}_{\alpha 1} \\ \text{M}_{\alpha 2} \\ \text{M}_{\alpha 3} \\ 0 \end{bmatrix} \begin{bmatrix} \frac{\gamma-1}{2} u_i u_i \\ -(\gamma-1)u_1 \\ -(\gamma-1)u_2 \\ -(\gamma-1)u_3 \\ \gamma-1 \end{bmatrix}^{\text{T}} \right) \right\}
$$

$$
- \sigma^V \boldsymbol{\Delta}_\alpha^{\pm} \text{proj} \begin{bmatrix} 0 & 0 & 0 & 0 & 0 \\ 0 & 1 & 0 & 0 & 0 \\ 0 & 0 & 1 & 0 & 0 \\ 0 & 0 & 0 & 1 & 0 \\ -\frac{T_w}{\gamma} & 0 & 0 & 0 & 1 \end{bmatrix}, \tag{5.18}
$$

respectively.

Theorem 5.6. *Let $\mathcal{J}[Q]$ be a functional of the form (2.14) where $\mathcal{K}_V[Q]$ is arbitrary and $\mathcal{K}_S[Q]$ is a (possibly trivial) function of the flux function along the x_α-direction: $\hat{\mathcal{F}}_\alpha[Q] = \text{M}_{\alpha i}\left(\mathcal{F}_i^I[Q] - \mathcal{F}_i^V[Q]\right)$. Then, the semi-discrete approximation (3.12) with the SAT (5.16) for enforcing an isothermal no-slip wall boundary condition (5.15) is weakly dual-consistent of order s for $\sigma^I = 1$ and σ^V arbitrary, where s is the order of accuracy of the boundary stencils of the diagonal-norm SBP operators in (3.12).*

Proof. Linearizing $\mathcal{K}_S[Q]$ leads to an expression of the form

$$
\delta \mathcal{K}_S[Q; \delta Q] = -\frac{\delta \mathcal{K}_S}{\delta \hat{\mathcal{F}}_\alpha}[Q]\left(\mathcal{A}_\alpha[Q]\delta Q - \mathcal{B}_{\alpha i}[Q]\frac{\partial}{\partial \xi_i}\left(\mathcal{C}[Q]\delta Q\right)\right),
$$

where $\frac{\delta \mathcal{K}_S}{\delta \hat{\mathcal{F}}_\alpha}[Q]$ is a vector-field valued functional with at most 4 non-trivial components since the flux function corresponding to density is zero at the wall. From (4.3), the continuous-adjoint boundary condition at the wall is

$$
\begin{bmatrix} 0 & 1 & 1 & 1 & 1 \end{bmatrix} Q^\dagger = \mp \left(\frac{\delta \mathcal{K}_S}{\delta \hat{\mathcal{F}}_\alpha}[Q]\right)^{\text{T}}, \ \boldsymbol{\xi} \in B_\alpha^{\pm}, \ t \geq 0. \tag{5.19}
$$

There are 4 linearly independent boundary conditions in (5.19), which is as expected given the well-known characteristic structure of the flow equaitons. Let $\vec{Q}_b^\dagger = \text{proj}\left(Q_b^\dagger\right)$, where $Q_b^\dagger(\boldsymbol{\xi}, t)$ satisfies (5.19).

From (4.13) and (5.18), we get

$$
\vec{\mathsf{R}}^{\dagger}_{\mathrm{SAT}}\left[\vec{Q}_b, \vec{Q}_b^{\dagger}\right] = \pm\left(\sigma^I - 1\right)\mathbf{J}\mathbf{P}^{-1}\left(\mathbf{A}_{\alpha}^{I}\left[\vec{Q}\right]\right)^{\mathrm{T}}\boldsymbol{\Delta}_{\alpha}^{\pm}\vec{Q}_b^{\dagger}
$$

$$
\mp\sigma^I\mathbf{J}\mathbf{P}^{-1}\mathrm{proj}\left(\begin{bmatrix} 0 \\ 0 \\ 0 \\ 0 \\ \gamma-1 \end{bmatrix}\begin{bmatrix} 0 \\ \mathrm{M}_{\alpha 1} \\ \mathrm{M}_{\alpha 2} \\ \mathrm{M}_{\alpha 3} \\ 0 \end{bmatrix}^{\mathrm{T}}\right)\boldsymbol{\Delta}_{\alpha}^{\pm}\vec{Q}_b^{\dagger}
$$

$$
\mp\mathbf{J}\mathbf{P}^{-1}\boldsymbol{\Delta}_{\alpha}^{\pm}\mathbf{C}^{\mathrm{T}}\left[\vec{Q}\right]\mathbf{B}_{i\alpha}^{\mathrm{T}}\left[\vec{Q}\right]\mathbf{D}_i\vec{Q}_b^{\dagger}.
$$

For $\sigma^I = 1$, the first term vanishes. Taking an inner product with $\delta\vec{Q}_b = \mathrm{proj}\left(\delta Q_b\right)$, where $\delta Q_b\left(\boldsymbol{\xi}, t\right)$ satisfies the linearized boundary conditions (5.17) yields $\left\langle\vec{\mathsf{R}}^{\dagger}_{\mathrm{SAT}}\left[\vec{Q}_b, \vec{Q}_b^{\dagger}\right], \delta\vec{Q}_b\right\rangle = 0$. The result follows from Lemma 5.2. $\qquad\square$

5.4 Interface Treatment for Multi-Block Grids

For simulations of flows involving complex geometries, discretization using a single structured mesh may be inefficient despite the existence of sophisticated grid generation techniques. This can be addressed using a semi-structured approach, in which the computational domain is divided into sub-domains that are individually more amenable to such a discretization. In this paper, we restrict ourselves to non-overlapping sub-domains which can intersect on a common interface, and require that grid lines passing through the interface are C^0 continuous. To simplify the discussion, we consider two sub-domains $\mathbb{D}^L$ and $\mathbb{D}^R$ with the properties described in Section 2.1, such that $\partial\mathbb{D}^L \cap \partial\mathbb{D}^R = B_1^{L+} = B_1^{R-}$. Figure 5.1 shows a schematic of such a configuration.

Let N_1^L and N_1^R denote the number of grid points along the ξ_1-direction for the sub-domains $\mathbb{D}^L$ and $\mathbb{D}^R$, respectively. Per our requirements, the number of grid points along the ξ_2- and ξ_3-directions are equal for both sub-domains and are denoted as N_2 and N_3, respectively. The semi-discretization formulated in Chapter 3 can be readily extended to this multi-block configuration by defining a semi-discrete vector

$$
\vec{f}(t) = \begin{bmatrix} \vec{f}^L(t) \\ \vec{f}^R(t) \end{bmatrix}, \tag{5.20}
$$

where $\vec{f}^L(t) \in \left[H^0\left(\mathbb{R}_0^+\right)\right]^{N_1^L N_2 N_3}$ and $\vec{f}^R(t) \in \left[H^0\left(\mathbb{R}_0^+\right)\right]^{N_1^R N_2 N_3}$. Thus, $\vec{f}(t)$ is an $\left(N_1^L + N_1^R\right)N_2 N_3 \times$
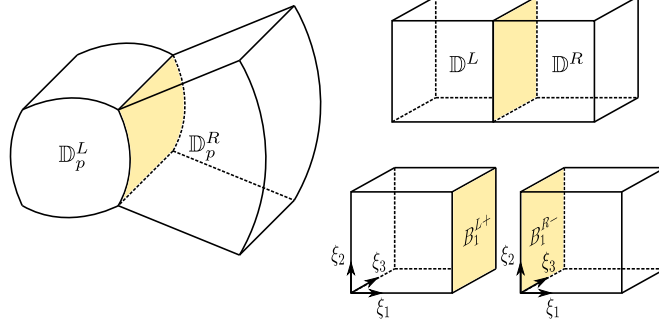
Figure 5.1: Schematic of a multi-block grid. $\mathbb{D}_p^L$ and $\mathbb{D}_p^R$ are the physical sub-domains; $\mathbb{D}^L$ and $\mathbb{D}^R$ are the corresponding computational sub-domains. There are a duplicate set of nodes on the interface $\partial\mathbb{D}^L \cap \partial\mathbb{D}^R$ corresponding to the computational boundary surfaces B_1^{L+} and B_1^{R-}, respectively.

1 column vector, whose components are the semi-discrete approximations of $f(\mathbf{x}, t)$ on the grid points corresponding to the sub-domains $\mathbb{D}^L$ and $\mathbb{D}^R$.

Nordström et al. [60] proposed an interface penalty term, which can be expressed using our notation as

$$
\vec{\mathsf{R}}_{\text{SAT},1}^{\text{int.}}\left[\vec{Q}\right] = \sigma_L^I \begin{bmatrix} \boldsymbol{\Delta}_1^{L+} & -\tilde{\boldsymbol{\Delta}}_1 \\ 0 & 0 \end{bmatrix} \mathbf{A}_1^{I-}\left[\vec{Q}_{\text{int.}}\right]\vec{Q} + \sigma_R^I \begin{bmatrix} 0 & 0 \\ \tilde{\boldsymbol{\Delta}}_1^{\text{T}} & -\boldsymbol{\Delta}_1^{R-} \end{bmatrix} \mathbf{A}_1^{I+}\left[\vec{Q}_{\text{int.}}\right]\vec{Q}
$$
$$
- \sigma^V \begin{bmatrix} \boldsymbol{\Delta}_1^{L+} & -\tilde{\boldsymbol{\Delta}}_1 \\ \tilde{\boldsymbol{\Delta}}_1^{\text{T}} & -\boldsymbol{\Delta}_1^{R-} \end{bmatrix} \mathbf{M}_{1i}\vec{\mathsf{F}}_i^V\left[\vec{Q}\right], \tag{5.21}
$$

where $\boldsymbol{\Delta}_1^{L+} = I_5 \otimes E_1^{L+} \otimes P_2 \otimes P_3$, $\boldsymbol{\Delta}_1^{R-} = I_5 \otimes E_1^{R-} \otimes P_2 \otimes P_3$, and $\tilde{\boldsymbol{\Delta}}_1 = I_5 \otimes \tilde{E}_1 \otimes P_2 \otimes P_3$. This form of expression will be useful for our objectives. We define $E_1^{L+} = \text{diag}\begin{bmatrix} 0 & 0 & \dots & 1 \end{bmatrix}_{N_1^L \times N_1^L}^{\text{T}}$ and $E_1^{R-} = \text{diag}\begin{bmatrix} 1 & 0 & \dots & 0 \end{bmatrix}_{N_1^R \times N_1^R}^{\text{T}}$ as before, so that $\boldsymbol{\Delta}_1^{L+}$ and $\boldsymbol{\Delta}_1^{R-}$ zero the components of a semi-discrete vector corresponding to nodes not located on the surfaces B_1^{L+} and B_1^{R-}, respectively. $\tilde{E}_1$ is defined as an $N_1^L \times N_1^R$ matrix with entry 1 at position $\left(N_1^L, 1\right)$ and zero everywhere else. Thus, when $\tilde{\boldsymbol{\Delta}}_1$ multiplies a semi-discrete vector of the form (5.20), it takes components of $\vec{f}^R(t)$ corresponding to nodes located on B_1^{R-}, scales them by a constant, and re-positions them so that they correspond to nodes located on B_1^{L+}. Implementing this operator in a numerical solver involves a transfer of data from between sub-domains and poses a challenge to our otherwise highly parallelizable multi-block stencil-based semi-discretization. Additional care is required when the sub-domains are oriented differently from the configuration shown in Figure 5.1. For instance, the sub-domains may be oriented such that the B_1^{L+} computational surface of $\mathbb{D}^L$ intersects the B_2^{R-} computational surface of $\mathbb{D}^R$. In practice, this may require reshaping of the data received by a sub-domain so that the ordering of the semi-discrete vectors $\vec{f}^L(t)$ and $\vec{f}^R(t)$ in (5.20) is preserved.

In (5.21), $Q_{\text{int.}}$ is the Roe-average of Q_L and Q_R defined as

$$\rho_{\text{int.}} = \sqrt{\rho^L \rho^R}$$

$$u_{\text{int.},i} = \frac{\sqrt{\rho^L} u_i^L + \sqrt{\rho^R} u_i^R}{\sqrt{\rho^L} + \sqrt{\rho^R}}, \quad \text{for } i = 1, 2, 3,$$

$$h_{\text{int.}} = \frac{\sqrt{\rho^L} h^L + \sqrt{\rho^R} h^R}{\sqrt{\rho^L} + \sqrt{\rho^R}},$$

where h denotes the enthalpy. Using the Roe-average for $Q_{\text{int.}}$ is necessary for conservation of inviscid fluxes across the interface — an arithmetic average, for example, doesn't guarantee conservation [66]. The first term in (5.21) penalizes the difference at the interface, of the inviscid fluxes corresponding to the characteristics entering $\mathbb{D}^L$ and those corresponding to characteristics leaving $\mathbb{D}^R$, the second term penalizes the difference between inviscid fluxes corresponding to characteristics leaving $\mathbb{D}^R$ and those corresponding to characteristics entering $\mathbb{D}^L$, and the last term penalizes the difference in viscous fluxes. The SAT (5.21) is stable for $\sigma_L^I \geq \frac{1}{2}$, $\sigma_R^I \geq \frac{1}{2}$ and $\sigma^V = \frac{1}{2}$ [60]. The condition for fluxes at the interface to be conserved is $\sigma_L^I = \sigma_R^I = 1$. We will show shortly that these conditions also lead to dual-consistency.

Theorem 5.7. *Let $\mathcal{J}[Q]$ be a functional of the form (2.14), where $\mathbb{D} = \mathbb{D}^L \cup \mathbb{D}^R$, and $\mathbb{D}^L$ and $\mathbb{D}^R$ are non-overlapping sub-domains as shown in Figure 5.1. Then, the semi-discrete approximation (3.12) with the SAT (5.21) is weakly dual-consistent of order s if $\sigma_L^I = \sigma_R^I = 1$ and $\sigma^V = \frac{1}{2}$, where s is the order of accuracy of the boundary stencils of the diagonal-norm SBP operators in (3.12).*

Proof. We ignore all other computational boundary surfaces except the interface $\partial \mathbb{D}^L \cap \partial \mathbb{D}^R$. An equivalent expression to (4.13) for the present multi-block grid is

$$\vec{\mathsf{R}}_{\text{SAT}}^\dagger \left[\vec{Q}, \vec{Q}^\dagger\right] = - \begin{bmatrix} \boldsymbol{\Delta}_1^{L+} & 0 \\ 0 & -\boldsymbol{\Delta}_1^{R-} \end{bmatrix} \mathbf{JP}^{-1} \left\{ \left(\mathbf{A}_1^I \left[\vec{Q}\right]\right)^{\mathrm{T}} \vec{Q}^\dagger - \mathbf{C}^{\mathrm{T}} \left[\vec{Q}\right] \mathbf{B}_{i1}^{\mathrm{T}} \left[\vec{Q}\right] \mathbf{D}_i \vec{Q}^\dagger \right\}$$

$$+ \mathbf{JP}^{-1} \left(\mathbf{A}_1^V \left[\vec{Q}\right] + \mathbf{B}_{1i} \left[\vec{Q}\right] \mathbf{D}_1 \mathbf{C} \left[\vec{Q}\right]\right)^{\mathrm{T}} \begin{bmatrix} \boldsymbol{\Delta}_1^{L+} & 0 \\ 0 & -\boldsymbol{\Delta}_1^{R-} \end{bmatrix} \vec{Q}^\dagger$$

$$+ \mathbf{JP}^{-1} \left(\mathbf{S}_{\text{SAT},1}^{\text{int.}} \left[\vec{Q}\right]\right)^{\mathrm{T}} \vec{Q}^\dagger + \begin{bmatrix} \boldsymbol{\Delta}_1^{L+} & 0 \\ 0 & \boldsymbol{\Delta}_1^{R-} \end{bmatrix} \mathbf{JP}^{-1} \frac{\delta \mathsf{K}_S}{\delta \vec{Q}} \left[\vec{Q}\right] = 0, \quad (5.22)$$

for all $\vec{Q}, \vec{Q}^\dagger \in V_h^{5N_1^L N_2 N_3} \times V_h^{5N_1^R N_2 N_3}$, where $\mathbf{S}_{\text{SAT},1}^{\text{int.}} \left[\vec{Q}\right]$ is defined implicitly using $\mathbf{S}_{\text{SAT},1}^{\text{int.}} \left[\vec{Q}\right] \delta \vec{Q} = \delta \vec{\mathsf{R}}_{\text{SAT},1}^{\text{int.}} \left[\vec{Q}; \delta \vec{Q}\right]$. Let $\vec{Q}_b = \text{proj}(Q_b)$, where $Q_b(\mathbf{x}, t)$ is C^0 continuous across the interface $\partial \mathbb{D}^L \cap \partial \mathbb{D}^R$. Since the computational surfaces B_1^{L+} and B_1^{R-} are topologically equivalent in the physical domain, the

Roe-averaged state in (5.21) is computed using "left" and "right" states that are both equal to Q_b. Linearizing (5.21), we get

$$\mathbf{S}_{\text{SAT},1}^{\text{int.}}\left[\vec{Q}_b\right] = \sigma_L^I \begin{bmatrix} \boldsymbol{\Delta}_1^{L+} & -\tilde{\boldsymbol{\Delta}}_1 \\ 0 & 0 \end{bmatrix} \mathbf{A}_1^{I-}\left[\vec{Q}_b\right] + \sigma_R^I \begin{bmatrix} 0 & 0 \\ \tilde{\boldsymbol{\Delta}}_1^{\text{T}} & -\boldsymbol{\Delta}_1^{R-} \end{bmatrix} \mathbf{A}_1^{I+}\left[\vec{Q}_b\right]$$

$$- \sigma^V \begin{bmatrix} \boldsymbol{\Delta}_1^{L+} & -\tilde{\boldsymbol{\Delta}}_1 \\ \tilde{\boldsymbol{\Delta}}_1^{\text{T}} & -\boldsymbol{\Delta}_1^{R-} \end{bmatrix} \left(\mathbf{A}_1^{V}\left[\vec{Q}_b\right] + \mathbf{B}_{1i}\left[\vec{Q}_b\right] \mathbf{D}_i \mathbf{C}\left[\vec{Q}_b\right]\right). \tag{5.23}$$

The surface integral in (2.14) does not have any contribution from nodes located on the interface. Hence, the last term in (5.22) vanishes. Using $\sigma_L^I = \sigma_R^I = 1$ and $\sigma^V = \frac{1}{2}$, and combining (5.22) and (5.23) leads to

$$\vec{\mathsf{R}}_{\text{SAT}}^{\dagger}\left[\vec{Q}_b, \vec{Q}^{\dagger}\right] = \mathbf{JP}^{-1}\left(\begin{bmatrix} 0 & 0 \\ -\tilde{\boldsymbol{\Delta}}_1^{\text{T}} & \boldsymbol{\Delta}_1^{R-} \end{bmatrix} \left(\mathbf{A}_1^{I-}\left[\vec{Q}_b\right]\right)^{\text{T}} + \begin{bmatrix} -\boldsymbol{\Delta}_1^{L+} & \tilde{\boldsymbol{\Delta}}_1 \\ 0 & 0 \end{bmatrix} \left(\mathbf{A}_1^{I+}\left[\vec{Q}_b\right]\right)^{\text{T}}\right) \vec{Q}^{\dagger}$$

$$+ \frac{1}{2}\mathbf{JP}^{-1}\left(\mathbf{A}_1^{V}\left[\vec{Q}_b\right] + \mathbf{B}_{1i}\left[\vec{Q}_b\right] \mathbf{D}_1 \mathbf{C}\left[\vec{Q}_b\right]\right)^{\text{T}} \begin{bmatrix} \boldsymbol{\Delta}_1^{L+} & -\tilde{\boldsymbol{\Delta}}_1 \\ \tilde{\boldsymbol{\Delta}}_1^{\text{T}} & -\boldsymbol{\Delta}_1^{R-} \end{bmatrix} \vec{Q}^{\dagger}$$

$$+ \mathbf{JP}^{-1} \begin{bmatrix} \boldsymbol{\Delta}_1^{L+} & 0 \\ 0 & -\boldsymbol{\Delta}_1^{R-} \end{bmatrix} \mathbf{C}^{\text{T}}\left[\vec{Q}\right] \mathbf{B}_{i1}^{\text{T}}\left[\vec{Q}\right] \mathbf{D}_i \vec{Q}^{\dagger}.$$

Rewriting (4.4) in a conservation form, it can be shown that the interface condition for the continuous-adjoint requires C^0 continuity of $\left(\mathcal{A}_1^{I\pm}[Q]\right)^{\text{T}} Q^{\dagger}(\mathbf{x}, t)$ and $\left\{-\left(\mathcal{A}_1^{V}[Q]\right)^{\text{T}} + \mathcal{C}^{\text{T}}[Q]\mathcal{B}_{i1}^{\text{T}}[Q]\right\} \partial Q^{\dagger}/\partial\xi_i$. Let $\vec{Q}_b^{\dagger} = \text{proj}\left(Q_b^{\dagger}\right)$ and $\delta\vec{Q}_b = \text{proj}(\delta Q_b)$, where $Q_b^{\dagger}(\mathbf{x}, t)$ satisfies this interface condition and $\delta Q_b(\mathbf{x}, t)$ is C^0 continuous across the interface. Then, we get

$$\left\langle \vec{\mathsf{R}}_{\text{SAT}}^{\dagger}\left[\vec{Q}_b, \vec{Q}_b^{\dagger}\right], \delta\vec{Q}_b \right\rangle = 0,$$

and the proof follows from Lemma 5.2. $\qquad\qquad\qquad\qquad\qquad\qquad\qquad\qquad\qquad\qquad$ $\square$

We defined diagonal-norm SBP operators in Section 3.1 and showed that they consist of $2s$-order accurate stencils at interior points and s-order accurate boundary closures, resulting in an overall order of accuracy of $s+1$ with respect to the diagonal norm associated with the operator. Hicken and Zingg [29] showed that when such schemes are combined with SATs that lead to a dual-consistent discretization, functional estimates can be obtained that are $2s$-order accurate, a property known as superconvergence. This result is proven for linear functionals of a scalar variable that satisfies a linear hyperbolic or elliptic PDE in one dimension, with a

seemingly direct extension to nonlinear functionals and PDEs discretized using three-dimensional curvilinear multi-block grids with interfaces. As a consequence of superconvergence, dual-consistent discretizations approximate the integral form of conservation laws upto the order of accuracy of the interior stencils of the SBP scheme used. Fisher et al. [21] constructed diagonal-norm SBP operators that can be cast as a telescoping operator consistent with the divergence form of conservation laws, which leads to discrete-exact global conservation even in the presence of shocks. For $s = 2$, their scheme is identical to the SBP 2–4 scheme used here. The SBP 3–6 and SBP 4–8 schemes used here do not satisfy a telescoping property. The interface dual-consistency condition proved in Theorem 5.7 is key to be able to use such schemes on multi-block grids with interfaces.

Chapter 6

Verification

Due to the complexity of the formulation, it is important to provide detailed verification that both the formulation and its implementation are correct. In this chapter, we consider two examples, including adjoint-based sensitivity of drag force for steady inviscid flow over a NACA0012 airfoil, and unsteady aeroacoustic control of a two-dimensional viscous shear layer. The examples have been chosen to test different aspects of the formulation and demonstrate the theorems presented in Chapter 5.

6.1 Drag Sensitivity of a NACA0012 Airfoil

First, we consider steady inviscid two-dimensional flow over a NACA0012 airfoil at $2°$ angle of attack. The freestream Mach number is 0.5. The shape of the top and bottom surfaces of the airfoil are described by

$$x_2 = \pm 5c'tf\left(x_1/c'\right),\ 0 \leq x_1 \leq c',$$

where c' is the chord length, $t = 0.12$, and

$$f\left(\eta\right) = 0.2969\sqrt{\eta} - 0.126\eta - 0.3516\eta^2 + 0.2843\eta^3 - 0.1015\eta^4.$$

Since this profile is not differentiable at $\mathbf{x} = \left(c', \pm 2.52 \times 10^{-3}c'\right)$, we regularize it with a smooth curve using

$$x_2 = \begin{cases} \pm 5c'tf\left(x_1/c'\right) & ,\ 0 \leq x_1 \leq c' \\ \pm c'\sqrt{\beta\left(x_1 - c\right)/c'} & ,\ c' < x_1 \leq c. \end{cases} \tag{6.1}$$

Enforcing C^1-continuity at $x_1 = c'$, we get $\beta = -1.2729 \times 10^{-4}$, and the modified chord length $c = 1.00449c'$. Hereafter, we will use c as the reference chord length for non-dimensionalization. An O-grid with 512×448 points in the directions tangential and normal to the airfoil surface, respectively, is generated by extruding the profile (6.1) outwards using the commercial software Gridgen [74]. The freestream flow is assumed to be
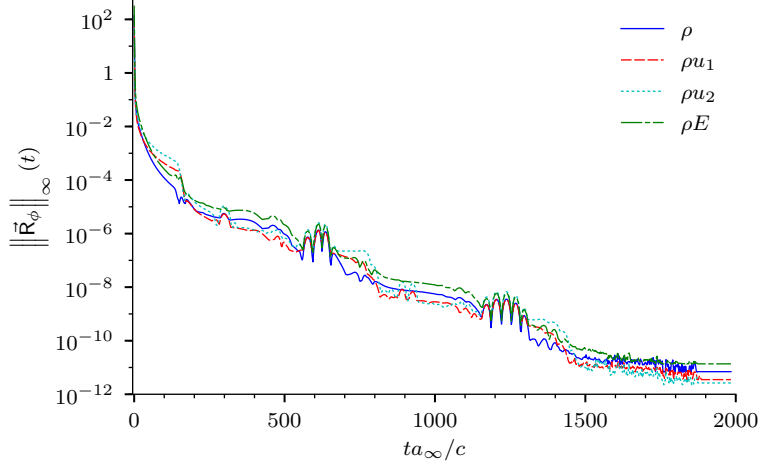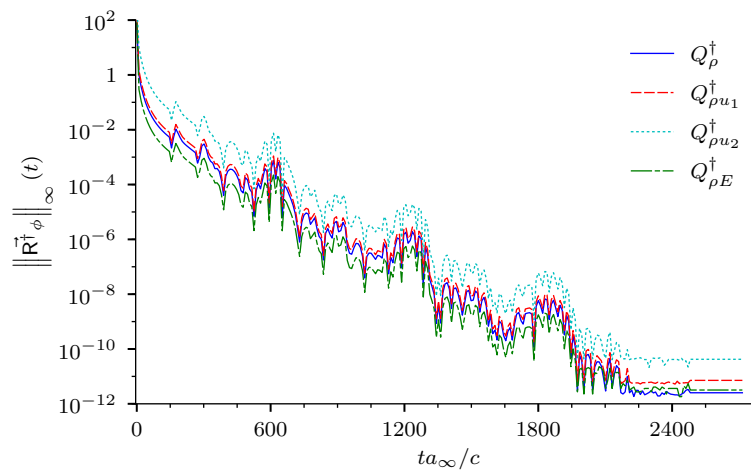
Figure 6.1: Convergence history of the normalized residuals for the density, momentum and energy equations.

along the x_1-direction and the grid is rotated to account for the angle of attack. In the direction normal to the airfoil surface, the physical domain extends to a distance of about $65c$. The mesh is stretched along this direction, with a maximum point-to-point stretching of 2%.

The flow is initialized with $\rho = \rho_\infty$, $u_1 = u_\infty = 0.5a_\infty$, $u_2 = 0$, and $p = p_\infty$. An SBP 2–4 scheme with fourth-order accuracy at interior points and second-order accuracy near boundaries is used in the semi-discrete approximation (3.12) excluding viscous terms. Artificial dissipation is included per (3.12) and (3.7) with $\sigma_{\text{diss.}} = 0.012$. At the surface of the airfoil, an SAT of the form (5.9) with $\sigma^I = 1$ enforces the impermeable wall condition. This effectively handles the initial transient introduced by using an initial condition that violates the impermeable wall condition on the airfoil surface. The outer far-field boundary is padded with a sponge layer of size $20c$, where the procedure described in Section 5.1 is used to model a far-field boundary condition.

Starting from the initial condition, the semi-discrete approximation of the compressible Euler equations are integrated in time using the fourth-order Runge–Kutta (RK4) scheme (3.16) until the residual $\left\| \vec{\mathsf{R}} \left[\vec{Q} \right] \right\|_\infty$ becomes zero up to floating-point roundoff. Figure 6.1 shows the convergence history of the residuals for the density, momentum and energy equations, respectively. For this steady-state problem, the time history of the flow solution is not required to solve the steady adjoint equations. Hence, alternate approaches for solving the nonlinear system $\vec{\mathsf{R}} \left[\vec{Q} \right] = 0$, such as Newton–Krylov methods are perfectly valid, and may even be more efficient. Our decision to use the RK4 method is motivated mainly by its ease of implementation and the popularity of it and related multi-stage methods in high-fidelity flow physics simulations.

Figure 6.2 visualizes the contours of $p - p_\infty$ at steady state. Figure 6.3 shows a comparison of the present numerical results for the pressure coefficient $C_p = \frac{p - p_\infty}{\frac{1}{2}\rho_\infty u_\infty^2}$ on the airfoil surface with the experiment

47
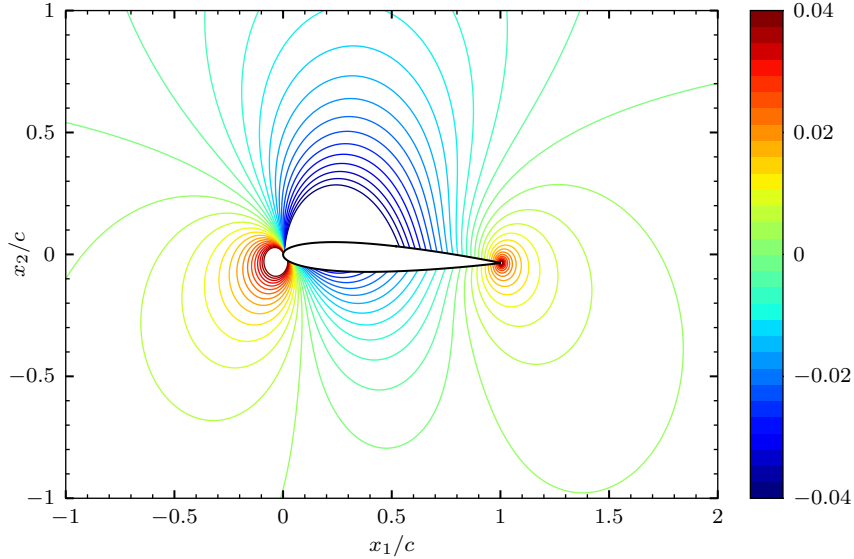
Figure 6.2: Contours of $p - p_\infty$ at steady state.

of Ladson et al. [42] at Ma $= 0.5054$, $\alpha = 2.0264°$ and $\mathrm{Re}_c = 3.025 \times 10^6$. A good qualitative agreement with the experiment is observed, which is sufficient for the purpose of this demonstration. Agreement is imperfect, as typically seen for this inviscid model [35, 71].

The drag force on the airfoil is

$$\mathcal{J}[Q] = - \int_{B_2^-} \left[p(\boldsymbol{\xi}, t) - p_\infty \right] \mathrm{M}_{21} d\xi_1,$$

where $\mathrm{M}_{21} d\xi_1$ is the area of an infinitesimal surface along the airfoil, and the integration is over the airfoil surface, which in our case maps to the computational boundary B_2^-. The corresponding continuous-adjoint boundary condition is $\mathrm{M}_{21} \left(Q_2^\dagger - 1 \right) + \mathrm{M}_{22} Q_3^\dagger = 0$. To solve the semi-discrete adjoint equations to obtain the sensitivity of $\mathcal{J}[Q]$, we use the same procedure and convergence criterion as the flow equations. Figure 6.4 shows the convergence history of the residuals of the adjoint density, momentum and energy equations, respectively.

From Theorem 5.5, the choice $\sigma^I = 1$ for the SAT at the airfoil surface leads to a dual-consistent scheme. Thus, we may anticipate the semi-discrete adjoint to be smooth and free from spurious oscillations. Figure 6.5 compares the $Q_3^\dagger$ adjoint field obtained using $\sigma^I = 1$ and $\sigma^I = 2$. At each point in physical space, the magnitude of $Q_3^\dagger$ represents the linear response of the drag functional to an impulse-like forcing applied at that point to the x_2-momentum equation. A negative sign indicates that a forcing in the $+x_2$-direction at that location is favorable, or leads to a reduction in drag, and vice-versa. The results in Figure 6.5 agree with the usual expectation that a suction force applied at the upper surface of the airfoil near the leading
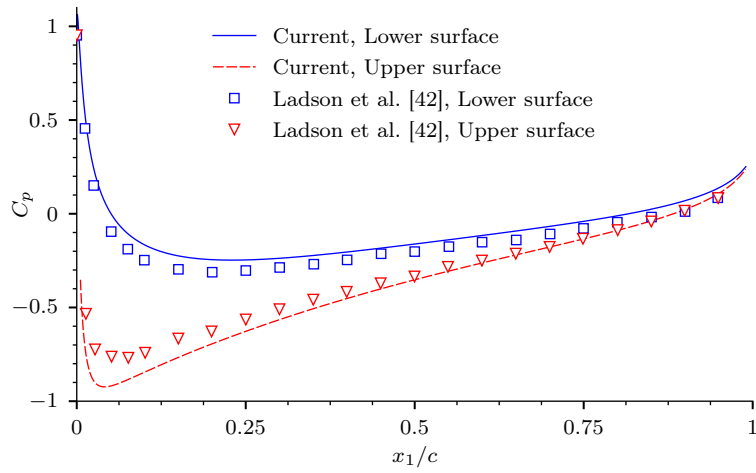
Figure 6.3: Comparison of pressure coefficient $C_p = \frac{p - p_\infty}{\frac{1}{2}\rho_\infty u_\infty^2}$ on the upper and lower surfaces of the airfoil with experiment.

Figure 6.4: Convergence history of the normalized residuals for the adjoint density, momentum and energy equations.
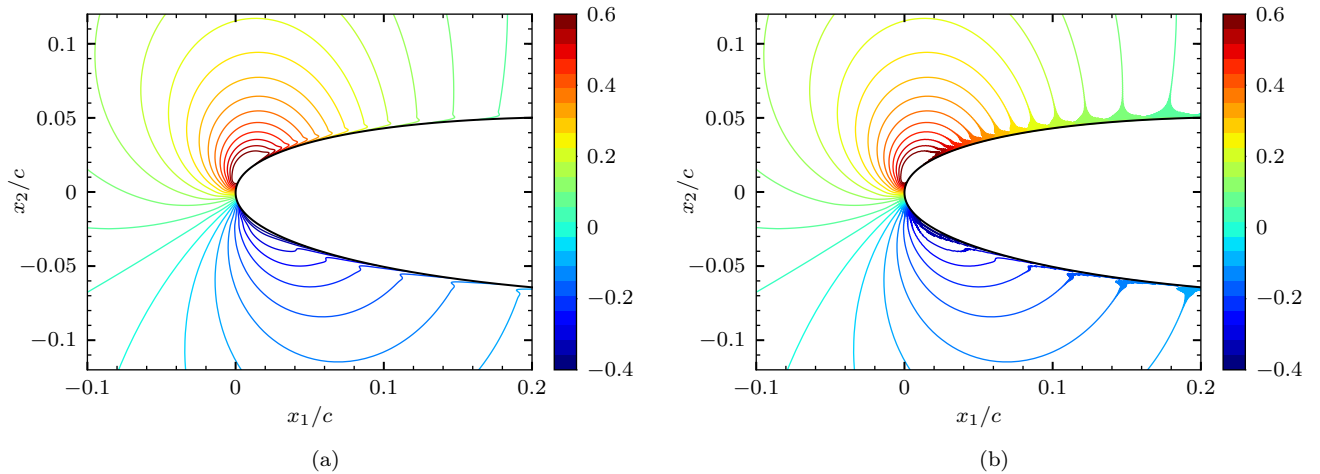
Figure 6.5: Comparison of the $Q_3^\dagger$ adjoint field obtained by solving the semi-discrete adjoint equations with: (a) a dual-consistent ($\sigma^I = 1$), and (b) a dual-inconsistent ($\sigma^I = 2$) discretization.

edge results in drag reduction. Further, the $Q_3^\dagger$ field in Figure 6.5a is similar to that obtained by Hicken and Zingg [31]. The steady-state dual-inconsistent adjoint solution is oscillatory and contains 2δ-waves, whose amplitude is maximum at the airfoil surface. We emphasize that this is still the discrete-exact adjoint of a valid and high-resolution space–time discretization of the flow equations. The spurious modes in the dual-inconsistent adjoint solution cannot be removed by increasing the amount of artificial dissipation, since this is not set independently but is constrained by the amount of dissipation added to the primal discretization through (4.11).

The dual-consistent adjoint field in Figure 6.5a is free from 2δ-waves and oscillatory behavior, but has a sharp gradient over a layer close to the airfoil surface. Tests revealed that the thickness of this layer is proportional to the amount of artificial dissipation $\sigma_{\text{diss.}}$ in (3.12). To investigate this further, we discretized the continuous-adjoint equations using the same numerics *and* the same adjoint coefficients, but instead of adding an artificial dissipation, we used an explicit five-point stencil fourth-order accurate filter [45] with strength $\sigma_f = 0.01$ applied every 20 timesteps. Figure 6.6 shows a comparison of the steady-state $Q_3^\dagger$ adjoint field obtained from the two approaches. Since Theorem 5.5 guarantees that (4.12) is a consistent and accurate discretization of the continuous-adjoint equations for $\sigma^I = 1$, we conclude that the sharp gradient in the adjoint field in Figure 6.6a is the sensitivity contribution to $\mathcal{J}[Q]$ of the artificial dissipation term in the primal system. We do not expect the impact of this to be significant in our viscous Navier–Stokes demonstrations, where the artificial viscosity due to numerical dissipation is relatively small compared to physical viscosity. If the numerical model of the viscous flow is deemed to be a sufficiently accurate representation of the physics, this then is the adjoint that is both consistent with its formulation for the

50
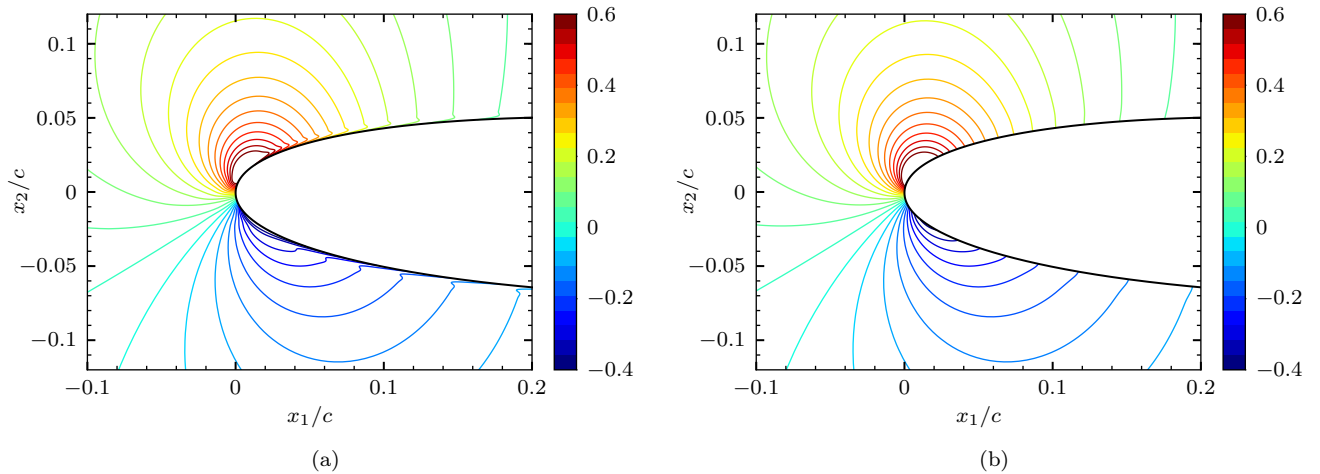
Figure 6.6: Comparison of the $Q_3^\dagger$ adjoint field obtained by solving the continuous-adjoint equations with: (a) an SAT artificial dissipation scheme, and (b) an explicit five-point stencil fourth-order accurate filter, which would not yield a dual-consistent form.

continuous problem and exact for its discretization.

6.2   Finite-Precision Effect on Discrete-Adjoint Accuracy

In Section 2.4, we showed that the accuracy of the discrete-adjoint-based gradient is limited by the finite-precision arithmetic employed when solving the discretized forward and adjoint equations. The effect of accumulation of roundoff errors becomes significant, especially when combined with the amplification of sensitivity due to the inherent chaos of turbulence. This will be discussed in some detail in Chapter 7, where we compare the accuracy of the continuous- and discrete-adjoint-based sensitivities based on the gradient error (2.22) for a turbulent mixing layer. Verifying the limit at which roundoff errors dominate the balance (2.23) for the discrete-adjoint method is in general, computationally expensive, since it requires simulations with multiple precisions that may not be natively supported at the computer hardware level. At the time of writing, quadruple-precision arithmetic, which involves operations on IEEE 754 128-bit floating point numbers [1] is only supported through software emulation on all computing architectures. Here, we demonstrate this roundoff error limit for a relatively computationally inexpensive simulation of a two-dimensional mixing layer using single-, double- and quadruple-precision arithmetic. This is a nonlinear, but relatively deterministic solution of the flow equations, for which we do not expect the amplification of errors to occur via the chaotic mechanisms available in the turbulent flows we consider subsequently in Chapters 7 and 8.

Figure 6.7 shows a schematic of this flow. It is a mixing layer between two streams of velocities $0.9a_\infty$

51
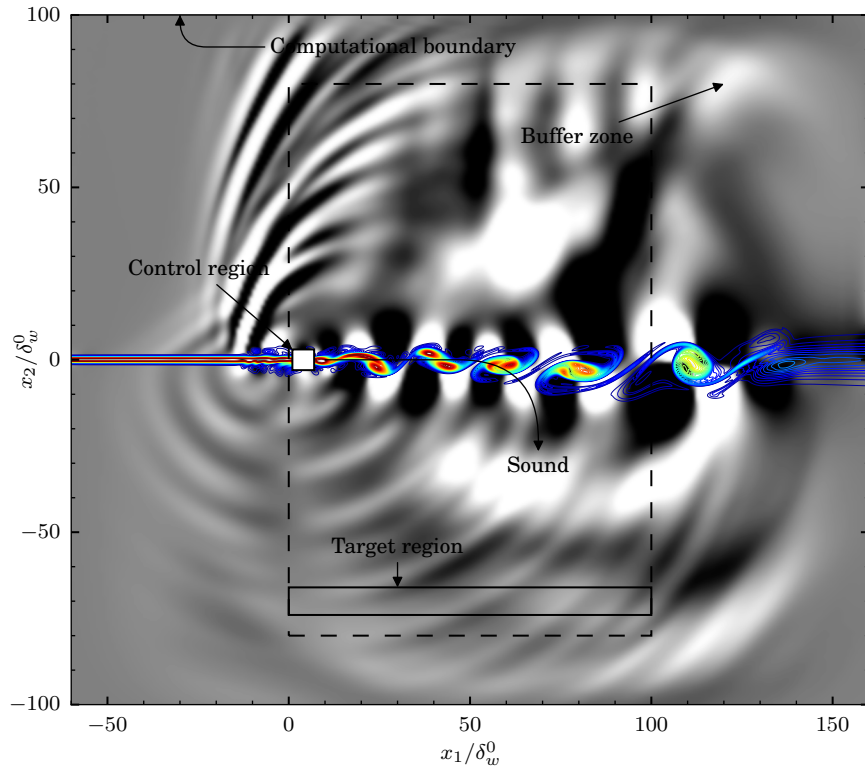
Figure 6.7: The two-dimensional spatially developing mixing layer visualized with vorticity magnitude (colors) and dilatation (grays) at $t = t_0$. The extent of the control region Γ is $\left[\delta_w^0, 7\delta_w^0\right] \times \left[-3\delta_w^0, 3\delta_w^0\right]$ and that of the target region Ω is $\left[0, 100\delta_w^0\right] \times \left[-74\delta_w^0, -66\delta_w^0\right]$.

and $0.2a_\infty$. It is simulated with a mesh with 961×641 grid points in the x_1- and x_2-directions, respectively. The target and control mollifying support functions from (2.14) and (2.19), respectively, are such that

$$W_\Omega\left(\boldsymbol{\xi}\right) \sim B_{0,2}\left(x_2^\Omega\right)\left\{\tanh\left[160\left(x_1^\Omega - 0.035\right)\right] - \tanh\left[160\left(x_1^\Omega - 0.965\right)\right]\right\}$$

$$W_\Gamma\left(\boldsymbol{\xi}\right) \sim \left\{\tanh\left[40\left(x_1^\Gamma - 0.2\right)\right] - \tanh\left[40\left(x_1^\Gamma - 0.8\right)\right]\right\}\left\{\tanh\left[40\left(x_2^\Gamma - 0.2\right)\right] - \tanh\left[40\left(x_2^\Gamma - 0.8\right)\right]\right\},$$

and $\int_{\boldsymbol{\xi}\in\mathbb{D}} W_\Omega\left(\boldsymbol{\xi}\right)\frac{1}{J(\boldsymbol{\xi})}d^2\boldsymbol{\xi} = \int_{\boldsymbol{\xi}\in\mathbb{D}} W_\Gamma\left(\boldsymbol{\xi}\right)\frac{1}{J(\boldsymbol{\xi})}d^2\boldsymbol{\xi} = 1$, where

$$x_1^\Omega = \begin{cases} \frac{x_1}{100\delta_w^0}, & \left|\frac{x_1}{\delta_w^0} - 50\right| \leq 50 \\ 0, & \text{otherwise} \end{cases}$$

$$x_2^\Omega = \begin{cases} \frac{1}{8}\left(\frac{x_2}{\delta_w^0} + 74\right), & \left|\frac{x_2}{\delta_w^0} + 70\right| \leq 4 \\ 0, & \text{otherwise} \end{cases}$$

$$x_1^\Gamma = \begin{cases} \frac{1}{6}\left(\frac{x_1}{\delta_w^0} - 1\right), & \left|\frac{x_1}{\delta_w^0} - 4\right| \leq 3 \\ 0, & \text{otherwise} \end{cases}$$

$$x_2^\Gamma = \begin{cases} \frac{1}{6}\left(\frac{x_2}{\delta_w^0} + 3\right), & \left|\frac{x_2}{\delta_w^0}\right| \leq 3 \\ 0, & \text{otherwise.} \end{cases}$$

Full details of this flow are available [89, 90], and are not reported here. The mixing layer is advanced in time using a constant time step size $\Delta t = 0.03\delta_w^0/a_\infty$ using the RK4 scheme (3.16). Starting from the initial condition

$$\rho = \rho_\infty$$
$$u_1 = U_2 + \frac{1}{2}\left(U_1 - U_2\right)\left[1 + \tanh\left(\frac{2x_2}{\delta_w^0}\right)\right]$$
$$u_2 = 0$$
$$p = p_\infty,$$

where $U_1 = 0.9a_\infty$ and $U_2 = 0.2a_\infty$, the flow is simulated from $t = 0$ to $t = t_0 = 840\delta_w^0/a_\infty$, which marks the beginning of the control interval. Following this, $20,800$ timesteps are taken from $t = t_0$ to $t = t_1 = 1464\delta_w^0/a_\infty$.
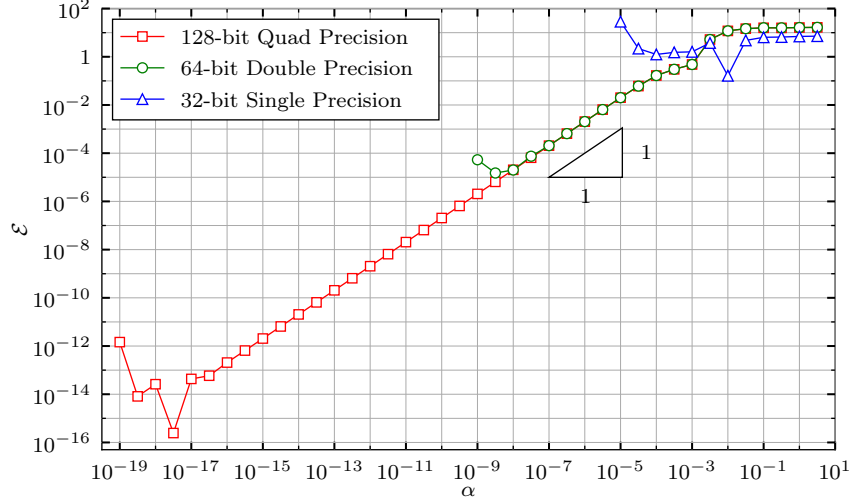
Figure 6.8: Gradient accuracy per (2.22) for different arithmetic precisions for the two-dimensional mixing layer.

Figure 6.8 shows a comparison between the accuracy of the discrete-exact gradients obtained from simulations performed with single 32-bit (single-precision), 64-bit (double-precision), and 128-bit (quadruple-precision) floating-point arithmetic. As $\alpha \to 0$, the gradient error $\mathcal{E} = \mathcal{O}(\alpha)$ upto a limit that is proportional to the computing precision. This indicates that the discrete-adjoint formulation as implemented in the numerical solver is compatible with the space–time discretization of the flow equations since any incompatibility would be expected to contribute to the $\mathcal{O}\left(\frac{1}{N_i^a}, \Delta t^b\right)$ term in (2.23) that dominates the floating-point roundoff errors for the spatial and temporal resolutions employed in this simulation. Figure 6.9 shows the discrete-adjoint $Q_4^\dagger(\boldsymbol{\xi}, t)$ field, which corresponds to the energy equation in a two-dimensional formulation. Theorem 5.4 guarantees that the discretization (3.12) is dual-consistent for $\sigma^I = \sigma^V = 1$ in the SATs (5.5) that enforce the boundary conditions. Thus, we anticipate the corresponding $Q_4^\dagger(\boldsymbol{\xi}, t)$ field to be free from sensitivities that are an artifact of the discretization . Figure 6.9a demonstrates this. In contrast, a different value $\sigma^I = 10$ that meets the stability condition for the SATs, leads to a non-smooth adjoint field which is still discrete-exact and compatible with the corresponding space–time discretization of the forward model. Vishnampet et al. [83] reported this quantity for the same mixing layer using a slightly different formulation with additional incompatibilities in the discretization that degrade the approximation (5.1) further. Their discretization violates Lemma 5.2, and leads to errors in (5.1) that have support both at the boundaries of the computational domain as well as at interior points. Consequently, their result showed significantly higher-amplitude saw-tooth type features in the $Q_4^\dagger(\boldsymbol{\xi}, t)$ field. Figure 6.9b shows similar saw-tooth type features, but to a much smaller extent.
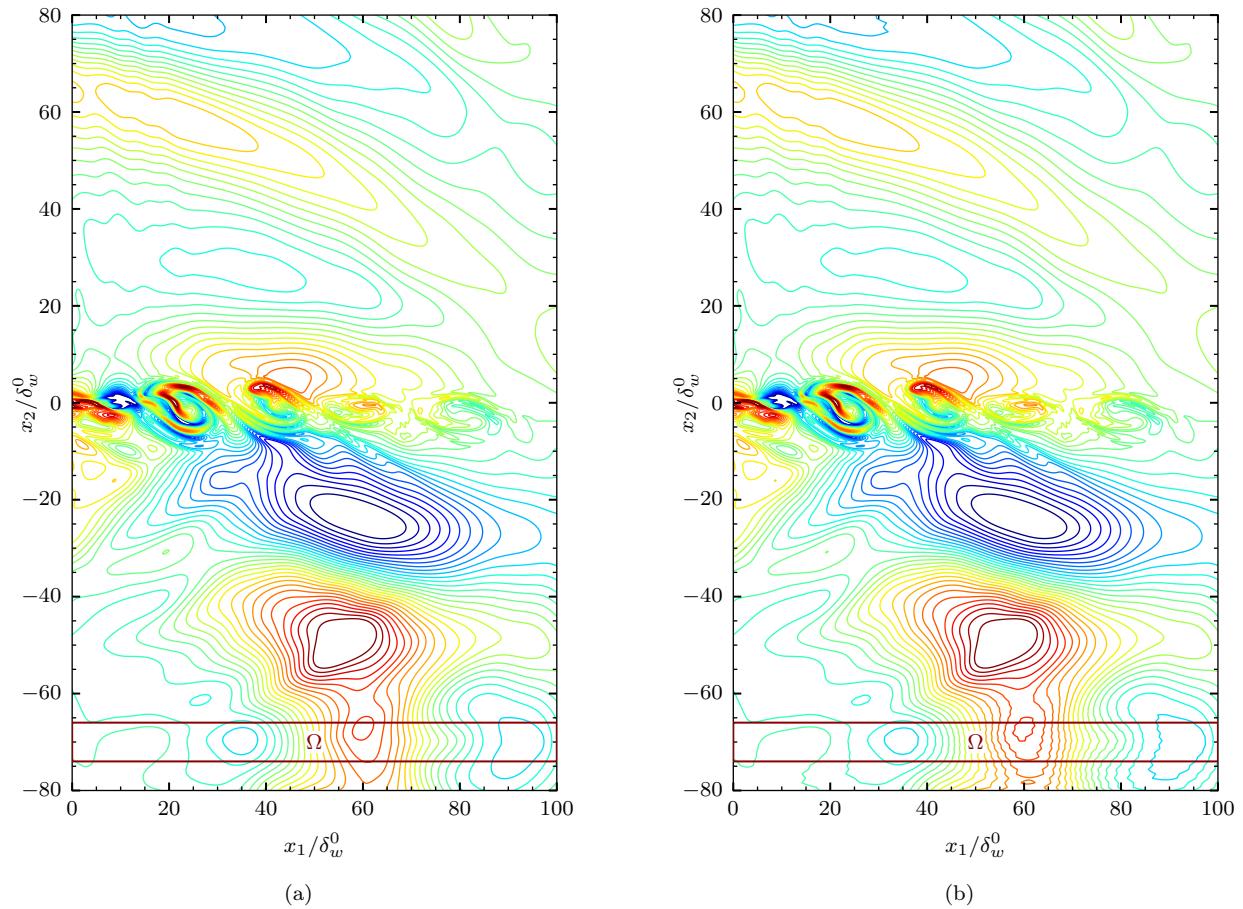
Figure 6.9: Comparison of the $Q_4^\dagger$ adjoint field obtained by solving the discrete-adjoint equations with: (a) $\sigma^I = 1$ which leads to a dual-consistent discretization, and (b) $\sigma^I = 10$ which leads to a stable, but dual-inconsistent discretization.

Chapter 7

Adjoint Errors in Turbulence

In this chapter, we derive the specific fully discrete adjoint equations corresponding to the three-dimensional compressible flow equations discretized with high-order schemes commonly used in aeroacoustic simulations. The spatial discretization considered here is different from that disucssed in Chapter 3 and does not have the same conservation properties, but is commonly used and effective for the class of flows we wish to study. The sensitivity gradient from the fully discrete adjoint formulation is shown to provide an exact gradient[*] of the cost functional for the sound radiated by a compressible turbulent mixing layer. Further, some key advances are made that make implementation of the fully discrete adjoint practical for such discretizations. This is an important step beyond the algorithms that have been developed to do this for aerodynamic simulations so far. Application of the fully discrete adjoint method to an important category of free-shear flows will highlight differences from the continuous-adjoint approach and facilitate an adjoint-field error analysis.

7.1 Flow Configuration

The fully discrete adjoint method is demonstrated on a three-dimensional temporally developing mixing layer shown in Figure 7.1, which is almost identical to the "ML2" mixing layer studied by Kleinman and Freund [39]. A temporally developing mixing layer is studied here because it captures the essential features of an inhomogeneous turbulent flow, while its periodicity in the streamwise and spanwise directions makes it computationally convenient. The initial mean flow is

$$\overline{u}_1 = \frac{\Delta U}{2} \tanh\left(\frac{x_2}{2\delta_m^0}\right)$$

$$\overline{u}_2 = \overline{u}_3 = 0$$

$$\overline{p} = p_\infty, \tag{7.1}$$

---

[*]Aside from roundoff errors introduced due to floating-point arithmetic.
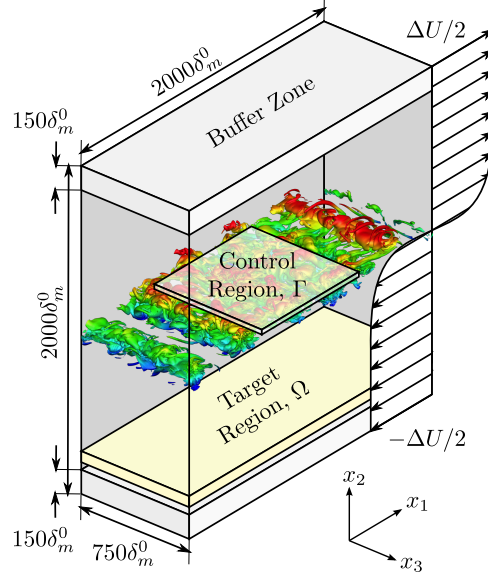
Figure 7.1: The three-dimensional temporally developing mixing layer at $t = t_0$ with turbulence visualized by vorticity magnitude isosurfaces colored by the value of x_2/δ_m^0.

with velocity difference $\Delta U = 0.9a_\infty$, where a_∞ is the ambient speed of sound. The initial mean density is obtained using the Crocco-Busemann relation assuming that upper and lower streams have the same temperature:

$$\overline{\rho} = \rho_\infty \left[1 + \frac{\gamma - 1}{2a_\infty^2} \left(\frac{\Delta U^2}{4} - \overline{u}_1^2 \right) \right]^{-1}. \tag{7.2}$$

The momentum thickness is used throughout as a length scale and is defined

$$\delta_m \left(t \right) = \frac{1}{\rho_\infty \Delta U^2} \int_{-\infty}^{\infty} \overline{\rho} \left(\frac{\Delta U^2}{4} - \widetilde{u}_1^2 \right) dx_2,$$

where $\overline{\cdot}$ and $\widetilde{\cdot}$ denote Reynolds and Favre averages, respectively [46]. The initial momentum thickness is defined as $\delta_m^0 = \delta_m \left(t = 0 \right)$. For the present flow configuration, the Reynolds average $\overline{\varphi} \left(x_2, t \right)$ is obtained by averaging $\varphi \left(\boldsymbol{x}, t \right)$ in the homogeneous x_1- and x_3-directions. The corresponding Favre average is

$$\widetilde{\varphi} = \frac{\overline{\rho\varphi}}{\overline{\rho}}.$$

Perturbations from the Reynolds and Favre averages are denoted as φ' and φ'', respectively.

7.2 Discretization

The governing equations discussed in Section 2.2 are rewritten here in the same form used for the semi-discrete approximation. The fluid is assumed to be a constant-viscosity Newtonian perfect gas with zero bulk viscosity $\mu_B = 0$ and the same non-dimensionalization described in Section 2.2 is used. In Cartesian coordinates, the expanded component-form of the governing equations (without any control action) is

$$\mathcal{N}_1[Q](\boldsymbol{x}, t) = \frac{\partial \rho}{\partial t} + \frac{\partial}{\partial x_i}(\rho u_i)$$

$$\mathcal{N}_{i+1}[Q](\boldsymbol{x}, t) = \frac{\partial}{\partial t}(\rho u_i) + \frac{\partial}{\partial x_j}(\rho u_i u_j + p\delta_{ij}) - \frac{\partial \tau_{ij}}{\partial x_j}, \quad \text{for } i = 1, 2, 3$$

$$\mathcal{N}_5[Q](\boldsymbol{x}, t) = \frac{\partial}{\partial t}(\rho E) + \frac{\partial}{\partial x_i}[u_i(\rho E + p)] - \frac{1}{\text{RePr}}\frac{\partial^2 T}{\partial x_i \partial x_i} - \frac{\partial}{\partial x_i}(\tau_{ij}u_j), \quad (7.3)$$

where

$$\tau_{ij} = \frac{1}{\text{Re}}\left(\frac{\partial u_i}{\partial x_j} + \frac{\partial u_j}{\partial x_i} - \frac{2}{3}\frac{\partial u_k}{\partial x_k}\delta_{ij}\right).$$

For this demonstration simulation, the governing equations (7.3) are discretized on a grid with $N_1 \times N_2 \times N_3 = 680 \times 425 \times 168$ points in the streamwise (x_1), cross-stream (x_2) and spanwise (x_3) directions, respectively. The computational domain extends from $-1000\delta_m^0$ to $1000\delta_m^0$ in the streamwise and cross-stream directions, and from $-375\delta_m^0$ to $375\delta_m^0$ in the spanwise direction. The mesh is uniform in the x_1- and x_3-directions. The transformation between the physical and computational domains is

$$X_1(\boldsymbol{\xi}) = 2000\delta_m^0(\xi_1 - 0.5)$$

$$X_2(\boldsymbol{\xi}) = 1000\delta_m^0 g(\xi_2)/g(1)$$

$$X_3(\boldsymbol{\xi}) = 750\delta_m^0(\xi_3 - 0.5), \quad (7.4)$$

where

$$g(s) = (s - 0.5)(1 + 2b) + b\sigma\left(\int_{-\frac{c}{\sigma}}^{\frac{s-0.5-c}{\sigma}}\text{erf}(x)\,dx - \int_{\frac{c}{\sigma}}^{\frac{s-0.5+c}{\sigma}}\text{erf}(x)\,dx\right), \quad 0 \leq s \leq 1.$$

The parameters $b = 12$, $c = 0.6$ and $\sigma = 0.21$ give a minimum spacing $\Delta x_{2,\text{min}} = 2.29\delta_m^0$ and a maximum point-to-point relative change in spacing of 2% at $x_2 = \pm 578\delta_m^0$. Figure (7.2) shows the mesh spacing Δx_2 and its point-to-point relative change in percentage as a function of the computational coordinate ξ_2. Derivatives in the x_i-direction are computed as
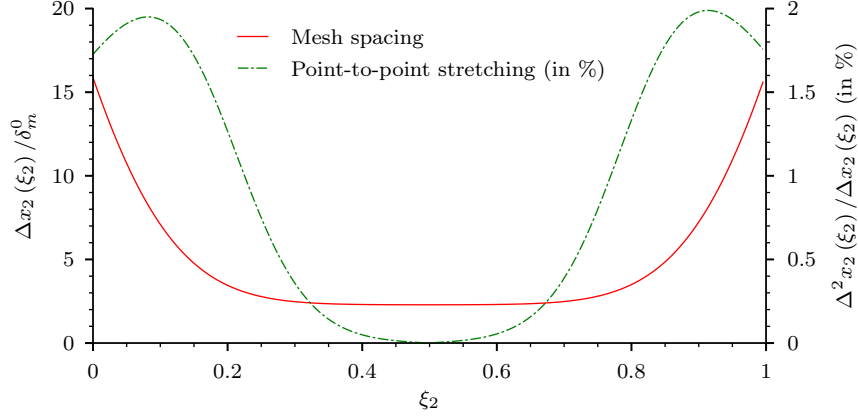
Figure 7.2: Mesh spacing $\Delta x_2 = x_{2,i+1} - x_{2,i}$ and its point-to-point relative change $\Delta^2 x_2 / \Delta x_2$ in the cross-stream direction for the three-dimensional temporally developing mixing layer.

$$\frac{\partial \varphi}{\partial x_i} = J \mathrm{M}_{ji} \frac{\partial \varphi}{\partial \xi_j}$$

$$\frac{\partial^2 \varphi}{\partial x_i \partial x_j} = J^2 \mathrm{M}_{li} \mathrm{M}_{kj} \frac{\partial^2 \varphi}{\partial \xi_l \partial \xi_k} + J \mathrm{M}_{li} \frac{\partial}{\partial \xi_l} \left(J \mathrm{M}_{kj} \right) \frac{\partial \varphi}{\partial \xi_k}. \tag{7.5}$$

Using (7.4) and (3.11), we can rewrite (7.5) as:

$$\frac{\partial \varphi}{\partial x_\alpha} = \begin{cases} \dfrac{1}{X'_\alpha} \dfrac{\partial \varphi}{\partial \xi_\alpha} & , \ \alpha = 2 \\[2ex] \dfrac{1}{h_\alpha} \dfrac{\partial \varphi}{\partial \xi_\alpha} & , \ \text{otherwise} \end{cases} \tag{7.6a}$$

$$\frac{\partial^2 \varphi}{\partial x_\alpha^2} = \begin{cases} \dfrac{1}{X'^2_\alpha} \dfrac{\partial^2 \varphi}{\partial \xi_\alpha^2} - \dfrac{X''_\alpha}{X'^3_\alpha} \dfrac{\partial \varphi}{\partial \xi_\alpha} & , \ \alpha = 2 \\[2ex] \dfrac{1}{h_\alpha^2} \dfrac{\partial^2 \varphi}{\partial \xi_\alpha^2} & , \ \text{otherwise} , \end{cases} \tag{7.6b}$$

respectively, where h_1 and h_3 are the (constant) mesh spacings in the ξ_1- and ξ_3-directions, respectively.

Explicit *narrow-stencil* SBP 3–6 finite-difference schemes are used to approximate first- and second-derivatives in the ξ_1- and ξ_2-directions. The schemes are fourth-order accurate with respect to a diagonal norm. The ξ_1-direction is periodic and therefore amenable to Fourier methods, but we use a finite-difference scheme to approximate derivatives along this direction because it facilitates efficient parallelization and better illustrates the methods as they would be used more generally. Mixed derivatvies are computed using a repeated application of two discrete first-derivative operators. The derivatives in the ξ_3-direction are computed using a Fourier transform. A Fourier filter removes the contribution of the highest 15% of wavenumbers in the ξ_3-direction to suppress aliasing errors. No other artificial dissipation such as discussed

in Section 3.2, or filtering is used.

Some additional definitions are required to construct the semi-discrete approximation of (7.3). Following the notation introduced in Section 3.1, we define

$$\hat{\mathbf{D}}_{ix_1} = D_{ix_1} \otimes I_{N_2} \otimes I_{N_3}$$

$$\hat{\mathbf{D}}_{ix_2} = I_{N_1} \otimes D_{ix_2} \otimes I_{N_3}$$

$$\hat{\mathbf{D}}_{ix_3} = I_{N_1} \otimes I_{N_2} \otimes D_{ix_3}, \tag{7.7}$$

for $i = 1, 2$, where D_{ix_α} approximates an i-th derivative along the x_α-direction, i.e., $\frac{\partial^i}{\partial x_\alpha^i}$ according to (7.6). Additionally, semi-discrete operators for a mixed derivative and a Laplacian are defined as

$$\hat{\mathbf{E}}_{ij} = \begin{cases} \hat{\mathbf{D}}_{1x_i} \hat{\mathbf{D}}_{1x_j} & , i \neq j \\ \hat{\mathbf{D}}_{2x_i} & , i = j, \end{cases}$$

and

$$\hat{\mathbf{L}} = \hat{\mathbf{D}}_{2x_1} + \hat{\mathbf{D}}_{2x_2} + \hat{\mathbf{D}}_{2x_3},$$

respectively. The semi-discrete approximation of (7.3) can be written as

$$\vec{\mathsf{N}}_1 \left[\vec{Q} \right](t) = \frac{d\vec{\rho}}{dt} + \hat{\mathbf{D}}_{1x_j} \overrightarrow{\rho u_j}$$

$$\vec{\mathsf{N}}_{i+1} \left[\vec{Q} \right](t) = \frac{d}{dt} \left(\overrightarrow{\rho u_i} \right) + \hat{\mathbf{D}}_{1x_j} \left(\overrightarrow{\rho u_i} \circ \vec{u}_j + \vec{p}\delta_{ij} \right) - \frac{1}{\mathrm{Re}} \left(\hat{\mathbf{L}}\vec{u}_i + \frac{1}{3}\hat{\mathbf{E}}_{ij}\vec{u}_j \right), \text{ for } i = 1, 2, 3,$$

$$\vec{\mathsf{N}}_5 \left[\vec{Q} \right](t) = \frac{d}{dt} \left(\overrightarrow{\rho E} \right) + \hat{\mathbf{D}}_{1x_j} \left[\vec{u}_j \circ \left(\overrightarrow{\rho E} + \vec{p} \right) \right] - \frac{1}{\mathrm{RePr}} \mathbf{L}\vec{T} - \frac{1}{\mathrm{Re}} \vec{u}_j \circ \left(\hat{\mathbf{L}}\vec{u}_j + \frac{1}{3}\hat{\mathbf{E}}_{jk}\vec{u}_k \right) - \frac{1}{\mathrm{Re}} \vec{\Phi},$$

where

$$\vec{\Phi} = \left(\mathbf{D}_{1x_j}\vec{u}_i \right) \circ \left(\mathbf{D}_{1x_1}\vec{u}_j \right) + \left(\mathbf{D}_{1x_i}\vec{u}_j \right) \circ \left(\mathbf{D}_{1x_1}\vec{u}_j \right) - \frac{2}{3} \left(\mathbf{D}_{1x_i}\vec{u}_i \right) \circ \left(\mathbf{D}_{1x_j}\vec{u}_j \right).$$

7.3 Initial and Boundary Conditions

To initialize the flow, the procedure described by Kleinman and Freund [39] is used, where an auxiliary simulation (denoted in that reference as "ML3") provides the initial condition for the present mixing layer. The auxiliary simulation is performed using the same physical domain discretized on a grid with $N_1 \times N_2 \times N_3 = 1710 \times 1043 \times 420$ in the streamwise (x_1), cross-stream (x_2) and spanwise (x_3) directions, respectively. Using the same analytical transformation (7.4) gives a minimum spacing $\Delta x_{2,\mathrm{min}} = 0.93\delta_m^0$ and a maximum

point-to-point relative change in spacing of 0.8% at $x_2 = \pm 580\delta_m^0$. The auxiliary simulation is initialized according to (7.1) and (7.2). To seed the turbulence, a velocity perturbation of the form:

$$u_1'\left(\mathbf{x}\right) = \sum_{i,j} \frac{\epsilon}{4\pi^2 k_{x_3}^j} e^{-\sigma x_2^2} \left(\sin x_2 + 2\sigma x_2 \cos x_2\right) \sin\left(k_{x_1}^i x_1 + \theta_1^i\right) \cos\left(k_{x_3}^j x_3 + \theta_3^j\right)$$

$$u_2'\left(\mathbf{x}\right) = -\sum_{i,j} \frac{\epsilon}{4\pi^2 k_{x_1}^i k_{x_3}^j} e^{-\sigma x_2^2} \cos x_2 \cos\left(k_{x_1}^i x_1 + \theta_1^i\right) \cos\left(k_{x_3}^j x_3 + \theta_3^j\right)$$

$$u_3'\left(\mathbf{x}\right) = \sum_{i,j} \frac{\epsilon}{4\pi^2 k_{x_1}^i} e^{-\sigma x_2^2} \left(\sin x_2 + 2\sigma x_2 \cos x_2\right) \cos\left(k_{x_1}^i x_1 + \theta_1^i\right) \sin\left(k_{x_3}^j x_3 + \theta_3^j\right),$$

is used, where $\epsilon = 0.05$, $\sigma = 1.125$, $k_{x_1}^i = 2\pi i/2000\delta_m^0$, $k_{x_3}^j = 2\pi j/750\delta_m^0$, and θ_1^i and θ_3^j are random phases in $[0, 2\pi)$, for $i = 333, \dots, 395$ and $j = 122, \dots, 182$. This corresponds to a longest wavelength of about $6\delta_m^0$ in the streamwise (x_1) direction and $6.15\delta_m^0$ in the spanwise (x_3) direction.

Starting from this initial condition, the auxiliary simulation was run from $t = 0$ to $t = 864\delta_m^0/\Delta U$. The solution from the auxiliary simulation is then interpolated onto the relatively coarser grid employed for the present mixing layer using a Fourier transform in the x_1- and x_3-directions, and cubic spline interpolation in the x_2-direction. To allow sufficient time for transients introduced due to the interpolation to exit the domain, the present mixing layer is simulated from $t = 0$ to $t = t_0 = 810\delta_m^0/\Delta U$, which corresponds to the control onset time (though the effect of the control on the sound field is delayed due to the finite speed of sound propagation). Starting from $t = t_0 = 810\delta_m^0/\Delta U$, the flow is simulated up to $t = t_1 = 2610\delta_m^0/\Delta U$.

The mixing layer grows linearly in time. The instantaneous vorticity thickness of the mixing layer is

$$\delta_w\left(t\right) = \frac{\Delta U}{\left|\partial \overline{u}_2/\partial x_2\right|_{\max}}.$$

Momentum and vorticity thickness growth for $t_0 \leq t \leq t_1$ are shown in Figure 7.3. During this interval, the momentum thickness increases from $\delta_m\left(t_0\right) = 19\delta_m^0$ to $\delta_m\left(t_1\right) = 53\delta_m^0$, or a factor of 2.8. The rate of growth of momentum thickness is $\dot{\delta}_m\left(t\right) = 0.019\Delta U$, which is identical to the value obtained by Kleinman [38].

7.4 Turbulence Statistics

Figure 7.4 shows a comparison of the mean streamwise velocity at $t = t_0$ with previous experiments and simulation. There is no laboratory equivalent of a temporally developing mixing layer. Hence, mean flow statistics are compared with expermients of spatially developing mixing layers. For a temporally developing mixing layer, the similarity variable is $x_2/\delta_w\left(t\right)$, where $\delta_w\left(t\right)$ is the instantaneous vorticity thickness.

(a) Momentum thickness

(b) Vorticity thickness
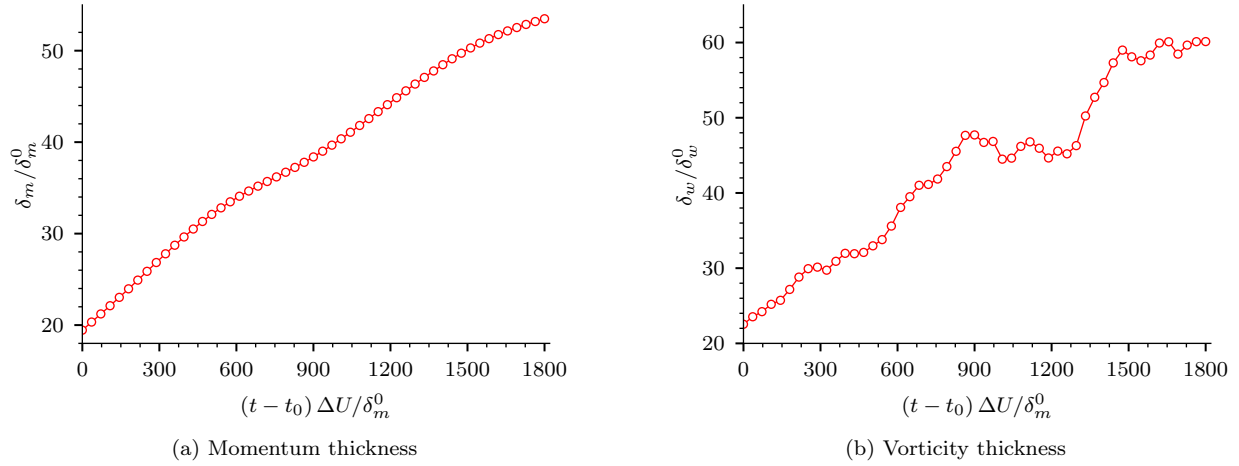
Figure 7.3: Evolution of momentum and vorticity thickness scaled by the initial thicknesses δ_m^0 and δ_w^0, respectively for the three-dimensional temporally developing mixing layer.
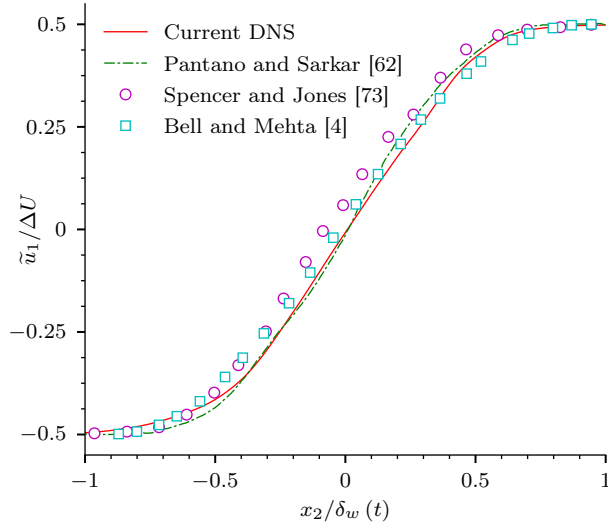
Figure 7.4: Comparison of Favre-averaged streamwise velocity versus cross-stream coordinate scaled by instantaneous vorticity thickness at $t = t_0$ with experiments [73, 4] and the DNS of Pantano and Sarkar [62].
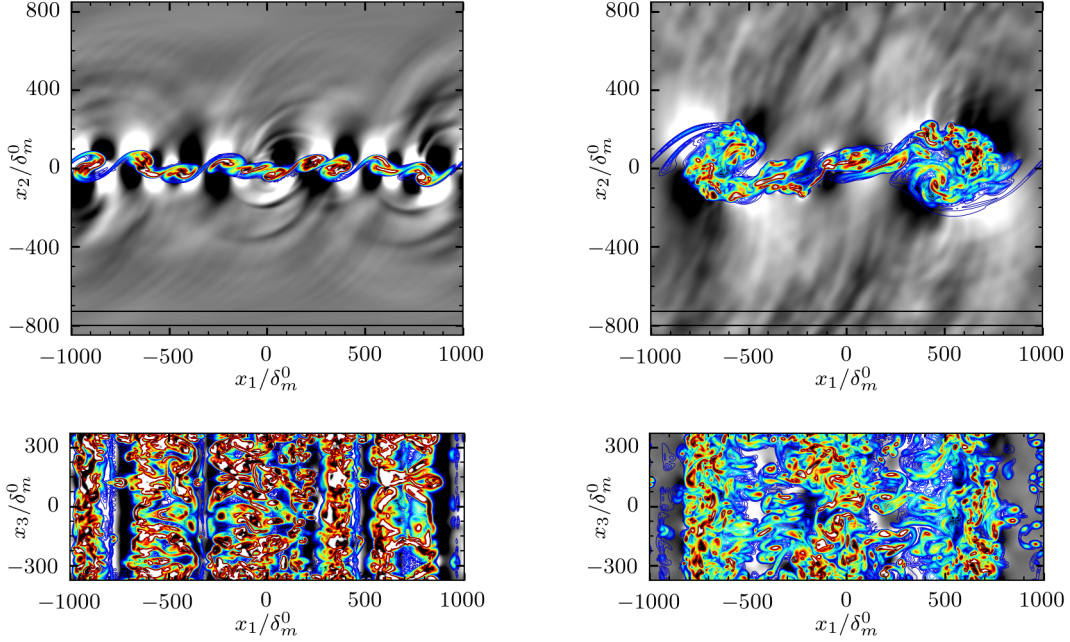
Figure 7.5: Visualization showing contours of vorticity magnitude and dilatation along $x_3/\delta_m^0 = 0$ (top) and $x_2/\delta_m^0 = 0$ (bottom) at $t = t_0$ (left) and $t = t_1$ (right) for the three-dimensional temporally developing mixing layer. The solid black lines are the boundaries of finite W_Ω defined in (7.9), where the radiated sound is measured.

Figure 7.5 visualizes the flow at $t = t_0$ and $t = t_1$. A realistic turbulence field appears to have developed by $t = t_0$. Reynolds stress statistics shown in Figure 7.6 support this, as do the turbulence spectra shown in Figures 7.7 and 7.8. The Reynolds stress profiles show a collapse in terms of the width, but a considerable disagreement exists between the peak values at various times. This is similar to the behavior observed by Kleinman [38], who suggested that the largest spatial structures may be influenced by the size of the computational domain at later times.

Figure 7.7 shows the one-dimensional kinetic energy and pressure spectra along the streamwise (x_1) direction during various times throughout the control horizon. Figure 7.8 shows the corresponding spectra along the spanwise (x_3) direction. Our goal was to challenge the control by applying it on a realistically broad-banded turbulent flow. The streamwise and spanwise spectra show significant energy over a broad range of wavenumbers, which drops at high wavenumbers due to viscosity, though a distinct $k \propto -5/3$ inertial range is not expected for $\text{Re}_{\delta_m(t_0)} = 926$. To assess the effect of the size of the computational domain, the correlations of velocity and pressure are shown in Figures 7.9 and 7.10. These are defined as

$$R_{\varphi'\varphi'}(x_2, t) = \int \varphi'(\mathbf{x}, t)\,\varphi'(\mathbf{x} + \overline{\mathbf{x}}, t)\,dx_1 dx_3,$$

63
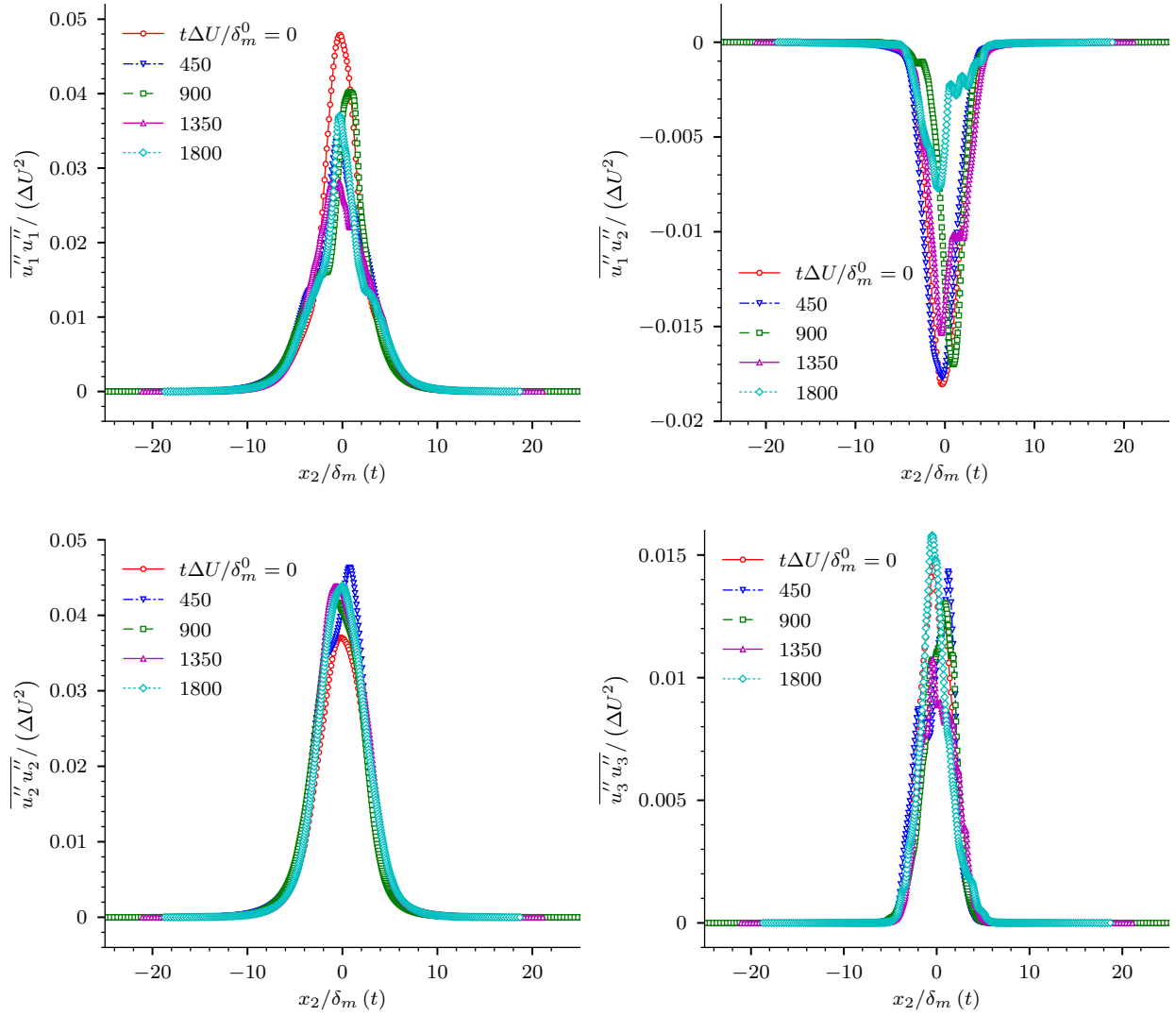
Figure 7.6: Reynolds stress profiles versus cross-stream coordinate scaled by instantaneous momentum thickness for the three-dimensional temporally developing mixing layer.
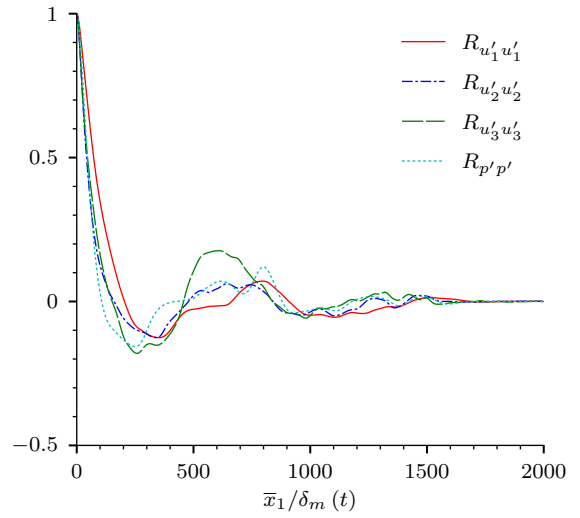
(a) $(t - t_0) \Delta U / \delta_m^0 = 0$

(b) $(t - t_0) \Delta U / \delta_m^0 = 594$
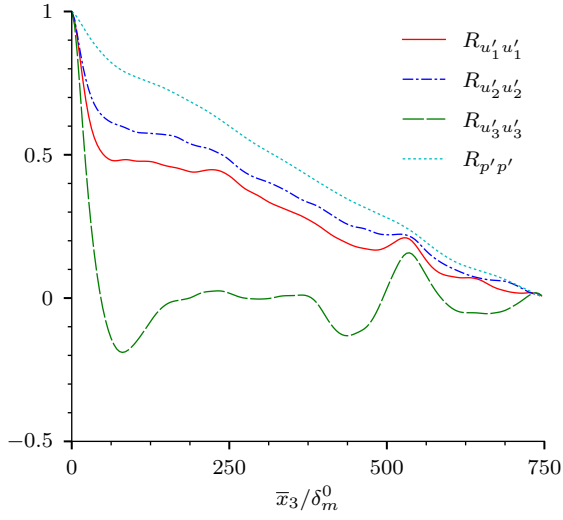
(c) $(t - t_0) \Delta U / \delta_m^0 = 1188$

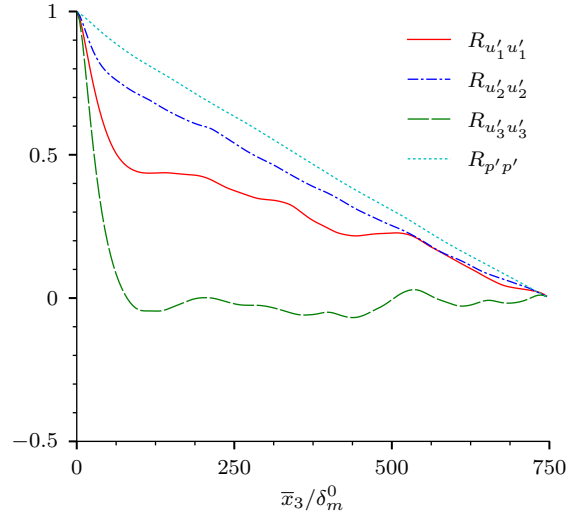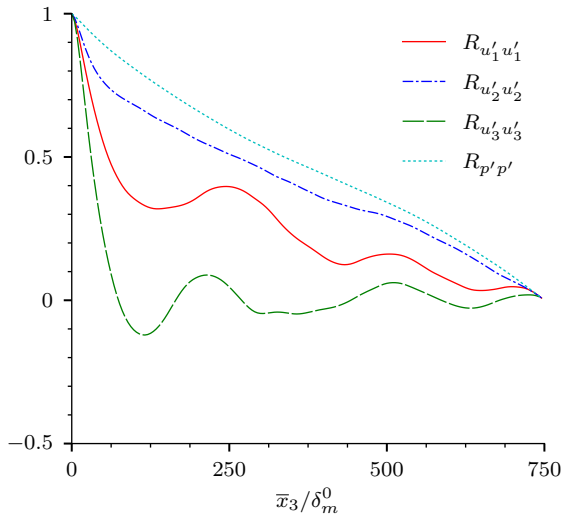(d) $(t - t_0) \Delta U / \delta_m^0 = 1782$
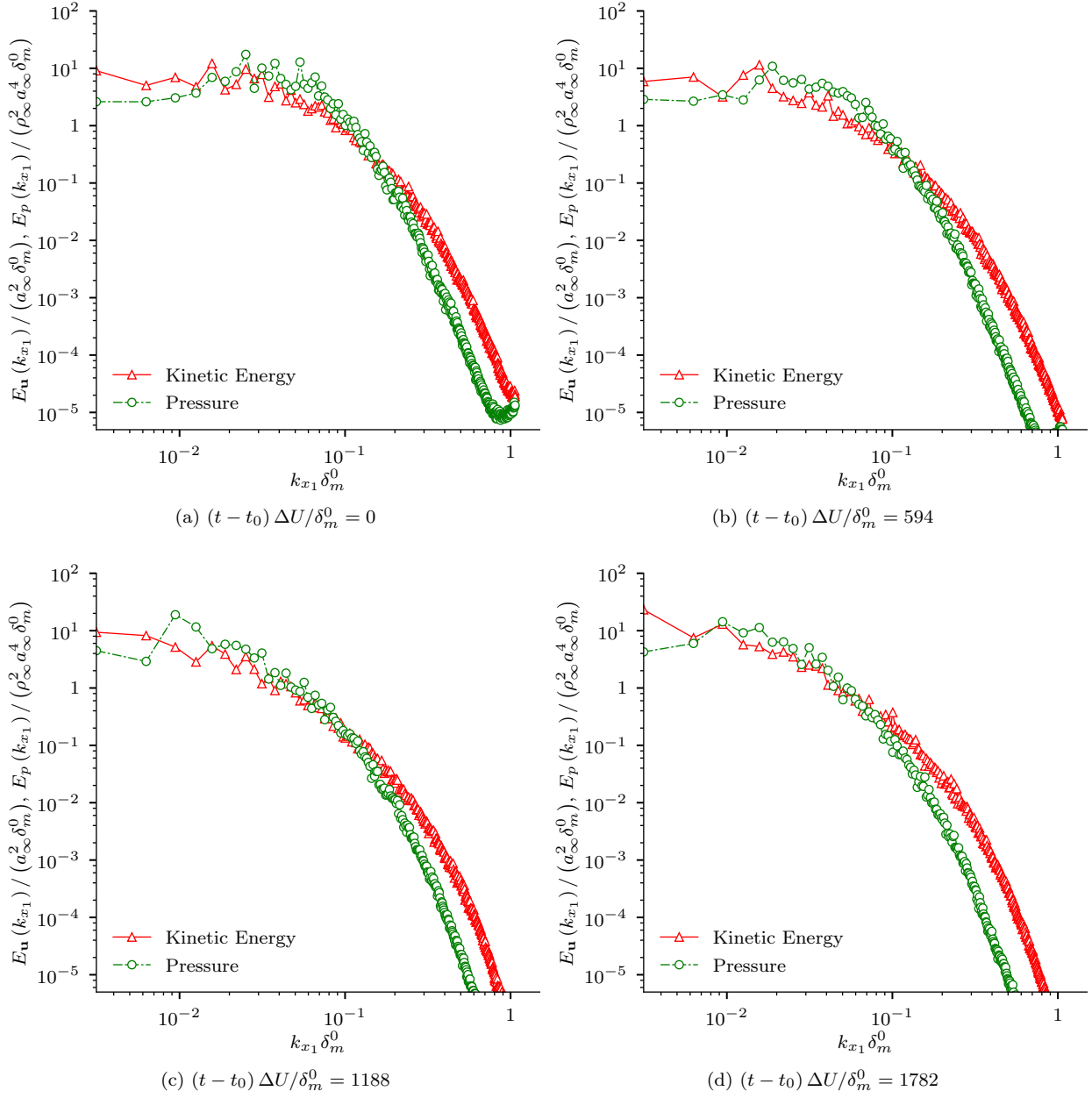
Figure 7.7: One-dimensional streamwise (x_1) kinetic energy and pressure spectra at $x_2/\delta_m^0 = 0$ for the three-dimensional temporally developing mixing layer.
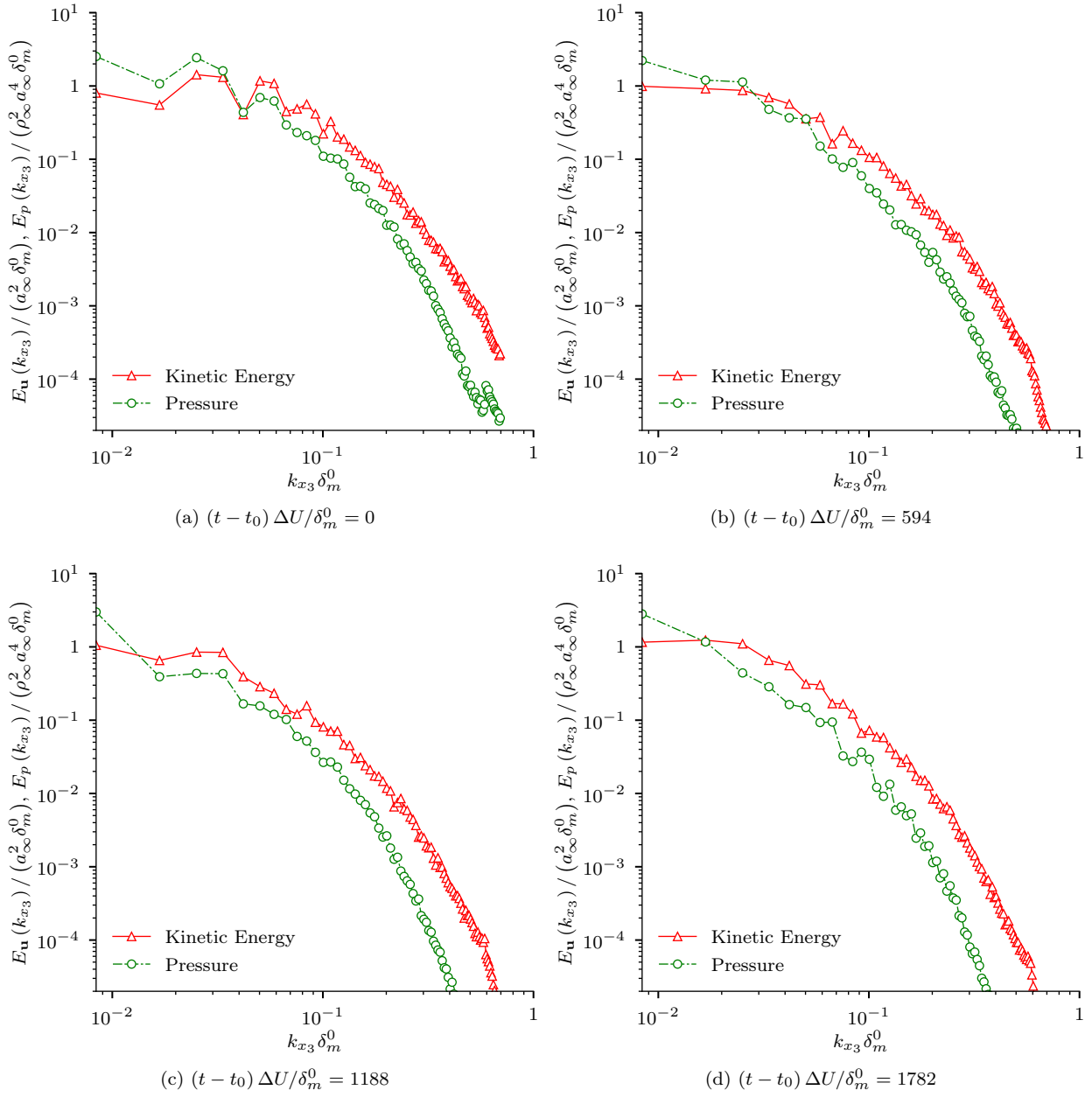
Figure 7.8: One-dimensional spanwise (x_1) kinetic energy and pressure spectra at $x_2/\delta_m^0 = 0$ for the three-dimensional temporally developing mixing layer.

where $\bar{x}_i = \bar{x}_1 \delta_{i1}$ for streamwise autocorrelations and $\bar{x}_i = \bar{x}_3 \delta_{i3}$ for spanwise autocorrelations. The correlations are normalized by their maximum values, which occurs for $\bar{\mathbf{x}} = 0$. For large $\bar{x}_1$, the streamwise correlations decay to zero, which indicates that the streamwise domain size is sufficient for simulating the present mixing layer. The spanwise correlations do not show the same decay and a finite, but a small correlation is observed even for $\bar{x}_3 \gtrsim 500 \delta_m^0$.

7.5   Control Implementation

The objective is to suppress the noise generated by the mixing layer, so the cost functional $\mathcal{J}[Q, f]$ is defined per (2.14) and (2.15). The target mollifying support function $W_\Omega(\boldsymbol{\xi}, t)$ in (2.14) is selected to have support in the target region shown in Figure 7.1. The specific form of $W_\Omega(\boldsymbol{\xi}, t)$ is such that

$$W_\Omega(\boldsymbol{\xi}, t) \sim B_{0,2}\left(x_2^\Omega\right) r_\Omega(t), \tag{7.9}$$

where

$$x_2^\Omega = \frac{1}{70\delta_m^0}\left(x_2 + 800\delta_m^0\right),$$

$$r_\Omega(t) = \frac{1}{2}\left[\tanh\left\{\frac{(t - t_0)/(t_1 - t_0) - 0.01}{0.001}\right\} + \tanh\left\{\frac{(t_1 - t)/(t_1 - t_0) - 0.01}{0.001}\right\}\right],$$

and $B_{0,2}$ is the B-spline basis function of degree 2

$$B_{0,2}(x) = \begin{cases} \frac{9}{2}x^2 & , \ 0 \le x \le \frac{1}{3} \\ -\frac{9}{2}x^2 + 9x - \frac{3}{2} & , \ \frac{1}{3} \le x \le \frac{2}{3} \\ \frac{9}{2}(1 - x)^2 & , \ \frac{2}{3} \le x \le 1 \\ 0 & , \ \text{otherwise.} \end{cases}$$

The B-spline basis function provides a compact support that blends smoothly to zero at the boundaries of the target region. To control radiated sound, the target region must be located in the acoustic field. To confirm that its support is sufficiently far from the turbulence to achieve this, the residual of the linearized Euler equations is computed for the uniform free-stream flow, which should become small in the acoustic field. Figure (7.11) shows this is so even at the control interval when the mixing layer has spread furthest. From its peak value at the mixing layer, the residual drops significantly suggesting that non-linearity is indeed negligible in the target region around $x_2 = -765\delta_m^0$.
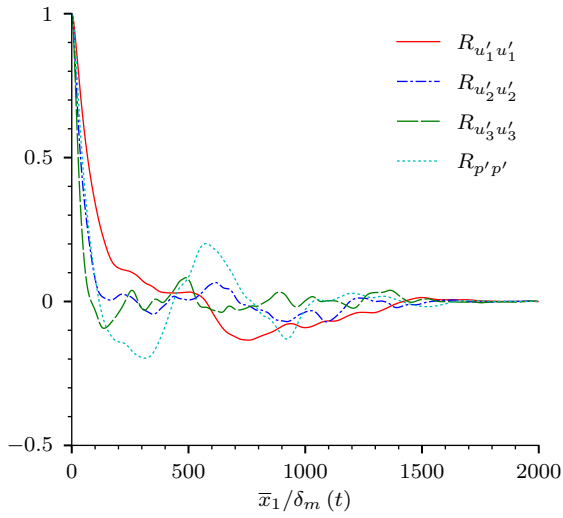
Figure 7.9: Normalized streamwise (x_1) autocorrelations of velocity and pressure at $x_2/\delta_m^0 = 0$ for the three-dimensional temporally developing mixing layer.
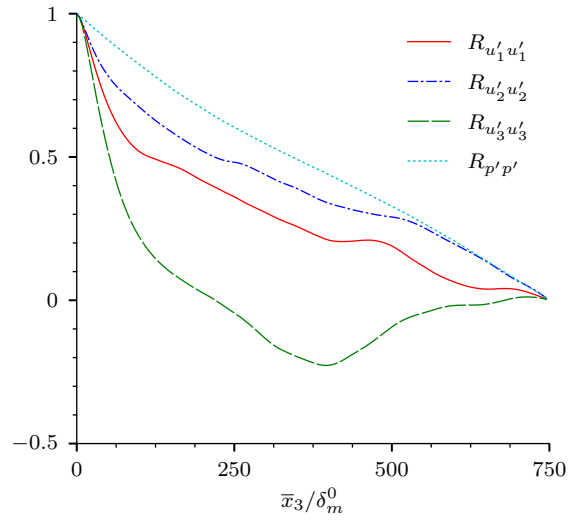
Figure 7.10: Normalized spanwise (x_3) autocorrelations of velocity and pressure at $x_2/\delta_m^0 = 0$ for the three-dimensional temporally developing mixing layer.
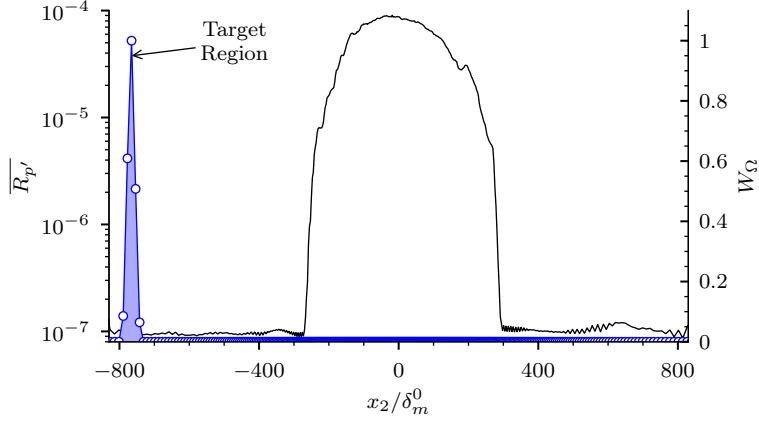
Figure 7.11: Residual of the linearized Euler equation applied to the pressure computed from the DNS data at $t = t_1$ for the three-dimensional temporally developing mixing layer. The target mollifying support $W_\Omega(\boldsymbol{\xi})$ is also shown.

The control for this demonstration is an energy source term with compact support in the control region shown in Figure 7.1. The control mollifying support function $W_\Gamma(\boldsymbol{\xi}, t)$ in (2.19) is selected to have support in the control region shown in Figure 7.1. The specific form of $W_\Gamma(\boldsymbol{\xi}, t)$ is such that

$$W_\Gamma(\boldsymbol{\xi}, t) \sim B_{0,2}\left(x_2^\Gamma\right) \left[\tanh\left\{60\left(x_1^\Gamma - 0.1\right)\right\} + \tanh\left\{60\left(0.9 - x_1^\Gamma\right)\right\}\right] r_\Gamma(t) \begin{bmatrix} 0 \\ 0 \\ 0 \\ 0 \\ 1 \end{bmatrix}, \qquad (7.10)$$

where

$$x_1^\Gamma = \frac{1}{800\delta_m^0}\left(x_1 + 400\delta_m^0\right)$$

$$x_2^\Gamma = \frac{1}{32\delta_m^0}\left(x_2 + 16\delta_m^0\right),$$

and $r_\Gamma(t) = r_\Omega(t)$. The mollifying support functions (7.9) and (7.10) are further scaled by the inverse of their norm based on the inner product (3.1). The target region extends fully across the computational domain in the periodic x_1- and x_3-directions. $r_\Gamma(t)$ and $r_\Omega(t)$ ensure that the control forcing in (2.19) and the target forcing in the adjoint equations increase gradually from zero. The control region is located in the shear layer, so that the control will alter the turbulence that makes the sound. Wei and Freund [90] explored different types of controls for a two-dimensional compressible mixing layer and achieved maximum

noise reduction using a thermal actuation, which is used for the present simulation.

7.6　The Adjoint and its Accuracy

Because a different semi-discrete approximation (7.8) is used to simulate the present mixing layer than the one for which the adjoint was formulated in Chapter 4, the corresponding semi-discrete adjoint operator is derived here. For subsequent comparisons and to provide context, we start with the continuous-adjoint equations. From the governing equations (7.3) and Definition 4.1, we get

$$
\begin{aligned}
\mathcal{N}_1^\dagger \left[Q, Q^\dagger \right] ={}& \frac{\partial Q_1^\dagger}{\partial t} + \frac{\gamma-1}{2} u_j u_j \frac{\partial Q_{i+1}^\dagger}{\partial x_i} - u_i u_j \frac{\partial Q_{i+1}^\dagger}{\partial x_j} + \left[\frac{\gamma-1}{2} u_i u_j u_j - \frac{u_i}{\rho}\left(\rho E + p \right) \right] \frac{\partial Q_5^\dagger}{\partial x_i} \\
& - \frac{1}{\mathrm{Re}} \left(\frac{u_i}{\rho} \frac{\partial^2 Q_{i+1}^\dagger}{\partial x_j \partial x_j} + \frac{1}{3} \frac{u_j}{\rho} \frac{\partial^2 Q_{i+1}^\dagger}{\partial x_i \partial x_j} \right) + \frac{u_j}{\rho} \tau_{ij} \frac{\partial Q_5^\dagger}{\partial x_i} \\
& - \frac{1}{\mathrm{Re}} \left[\frac{u_i}{\rho} \frac{\partial}{\partial x_j}\left(u_j \frac{\partial Q_5^\dagger}{\partial x_i} \right) + \frac{u_j}{\rho} \frac{\partial}{\partial x_i}\left(u_j \frac{\partial Q_5^\dagger}{\partial x_i} \right) \right] + \frac{2}{3\mathrm{Re}} \frac{u_j}{\rho} \frac{\partial}{\partial x_j}\left(u_i \frac{\partial Q_5^\dagger}{\partial x_i} \right) \\
& + \frac{\gamma}{\mathrm{RePr}\rho^2} \left(\frac{1}{2} \rho u_j u_j - \frac{p}{\gamma-1} \right) \frac{\partial^2 Q_5^\dagger}{\partial x_i \partial x_i}, \\
\mathcal{N}_{i+1}^\dagger \left[Q, Q^\dagger \right] ={}& \frac{\partial Q_{i+1}^\dagger}{\partial t} + \frac{\partial Q_1^\dagger}{\partial x_i} - \left(\gamma - 1 \right) u_i \frac{\partial Q_{j+1}^\dagger}{\partial x_j} + u_j \left(\frac{\partial Q_{j+1}^\dagger}{\partial x_i} + \frac{\partial Q_{i+1}^\dagger}{\partial x_j} \right) \\
& - \left(\gamma - 1 \right) u_i u_j \frac{\partial Q_5^\dagger}{\partial x_j} + \frac{1}{\rho}\left(\rho E + p \right) \frac{\partial Q_5^\dagger}{\partial x_i} + \frac{1}{\mathrm{Re}}\left(\frac{1}{\rho} \frac{\partial^2 Q_{i+1}^\dagger}{\partial x_j \partial x_j} + \frac{1}{\rho} \frac{\partial^2 Q_{j+1}^\dagger}{\partial x_i \partial x_j} \right) \\
& - \frac{2}{3\mathrm{Re}} \frac{1}{\rho} \frac{\partial^2 Q_{j+1}^\dagger}{\partial x_j \partial x_i} - \frac{1}{\rho} \tau_{ji} \frac{\partial Q_5^\dagger}{\partial x_j} + \frac{1}{\mathrm{Re}} \left[\frac{1}{\rho} \frac{\partial}{\partial x_j}\left(u_j \frac{\partial Q_5^\dagger}{\partial x_i} \right) + \frac{1}{\rho} \frac{\partial}{\partial x_j}\left(u_i \frac{\partial Q_5^\dagger}{\partial x_j} \right) \right] \\
& - \frac{2}{3\mathrm{Re}} \frac{1}{\rho} \frac{\partial}{\partial x_i}\left(u_j \frac{\partial Q_5^\dagger}{\partial x_j} \right) - \frac{\gamma u_i}{\mathrm{RePr}\rho} \frac{\partial^2 Q_5^\dagger}{\partial x_j \partial x_j}, \quad \text{for } i = 1, 2, 3, \\
\mathcal{N}_5^\dagger \left[Q, Q^\dagger \right] ={}& \frac{\partial Q_5^\dagger}{\partial t} + \left(\gamma - 1 \right) \frac{\partial Q_{i+1}^\dagger}{\partial x_i} + \gamma u_i \frac{\partial Q_5^\dagger}{\partial x_i} + \frac{\gamma}{\mathrm{RePr}} \frac{1}{\rho} \frac{\partial^2 Q_5^\dagger}{\partial x_i \partial x_i}.
\end{aligned}
\tag{7.11}
$$

These equations are identical to those reported by Kleinman [38], who report non-reflecting adjoint boundary conditions that are compatible with the radiation condition for the adjoint at the cross-stream boundaries. Although the formulation does not require this, to numerically solve (7.11), the derivatives are discretized using the same schemes as for the flow equations discussed in Section 7.2, including the same fourth-order Runge–Kutta scheme for time-integration. The boundary conditions for $Q^\dagger$ on the cross-stream boundaries $\boldsymbol{\xi} \in B_2^\pm$ are implemented using the SAT

$$
\vec{\mathsf{R}}_{\mathrm{SAT},2}^\pm \left[\vec{Q} \right] = \pm \sigma^I \boldsymbol{\Delta}_2^\pm \mathbf{A}_2^{I\pm} \left[\vec{Q}_t \right] \left(\vec{Q} - \vec{Q}_t \right).
$$

71

To derive the semi-discrete adjoint operator, we use the identity (4.11), which leads to

$$\vec{\mathsf{R}}^\dagger\left[\vec{Q},\vec{Q}^\dagger\right] = \vec{\mathsf{R}}^\dagger_{\text{interior}}\left[\vec{Q},\vec{Q}^\dagger\right] + \vec{\mathsf{R}}^\dagger_{\text{SAT}}\left[\vec{Q},\vec{Q}^\dagger\right] + \frac{\delta \mathsf{K}_v}{\delta \vec{Q}}\left[\vec{Q}\right],$$

where

$$
\begin{aligned}
\vec{\mathsf{R}}^\dagger_{\text{interior},1}\left[\vec{Q},\vec{Q}^\dagger\right] &= \left(\delta_{ij}\frac{\gamma-1}{2}\vec{u}_k\circ\vec{u}_k - \vec{u}_i\circ\vec{u}_j\right)\circ\left(\mathbf{D}^\dagger_{1x_j}\vec{Q}^\dagger_{i+1}\right) \\
&+ \left[\frac{\gamma-1}{2}\vec{u}_i\circ(\vec{u}_k\circ\vec{u}_k) - \frac{\vec{u}_i}{\vec{\rho}}\circ\left(\overrightarrow{\rho E}+\vec{p}\right)\right]\circ\left(\mathbf{D}^\dagger_{1x_i}\vec{Q}^\dagger_5\right) \\
&+ \frac{1}{\text{Re}}\frac{\vec{u}_i}{\vec{\rho}}\circ\left(\mathbf{L}^\dagger\vec{Q}^\dagger_{i+1}\right) + \frac{1}{3\text{Re}}\frac{\vec{u}_j}{\vec{\rho}}\circ\left(\mathbf{E}^\dagger_{ij}\vec{Q}^\dagger_{i+1}\right) + \frac{1}{\text{Re}}\frac{\vec{u}_i}{\vec{\rho}}\circ\left[\mathbf{L}^\dagger\left(\vec{u}_i\circ\vec{Q}^\dagger_5\right)\right] \\
&+ \frac{2}{\text{Re}}\frac{\vec{u}_i}{\vec{\rho}}\circ\left\{\mathbf{D}^\dagger_{1x_j}\left[(\mathbf{D}_{1x_i}\vec{u}_j + \mathbf{D}_{1x_j}\vec{u}_i)\circ\vec{Q}^\dagger_5\right]\right\} + \frac{1}{3\text{Re}}\frac{\vec{u}_j}{\vec{\rho}}\circ\left[\mathbf{E}^\dagger_{ij}\left(\vec{u}_i\circ\vec{Q}^\dagger_5\right)\right] \\
&- \frac{4}{3\text{Re}}\frac{\vec{u}_i}{\vec{\rho}}\circ\left\{\mathbf{D}^\dagger_{1x_i}\left[(\mathbf{D}_{1x_j}\vec{u}_j)\circ\vec{Q}^\dagger_5\right]\right\} - \frac{\gamma}{\text{RePr}\,(\gamma-1)}\left(\frac{\gamma-1}{2}\frac{\vec{u}_k\circ\vec{u}_k}{\vec{\rho}} - \frac{\vec{p}}{\vec{\rho}^2}\right)\circ\left(\mathbf{L}^\dagger\vec{Q}^\dagger_5\right) \\
&+ \frac{1}{\text{Re}}\frac{\vec{u}_i}{\vec{\rho}}\circ\left[\left(\mathbf{L}\vec{u}_i + \frac{1}{3}\mathbf{E}_{ij}\vec{u}_j\right)\circ\vec{Q}^\dagger_5\right] \\
\vec{\mathsf{R}}^\dagger_{\text{interior},i+1}\left[\vec{Q},\vec{Q}^\dagger\right] &= \mathbf{D}^\dagger_{1x_i}\vec{Q}^\dagger_1 - (\gamma-1)\,\vec{u}_i\circ\left(\mathbf{D}^\dagger_{1x_j}\vec{Q}^\dagger_{j+1}\right) + \vec{u}_j\circ\left(\mathbf{D}^\dagger_{1x_i}\vec{Q}^\dagger_{j+1} + \mathbf{D}^\dagger_{1x_j}\vec{Q}^\dagger_{i+1}\right) \\
&+ \frac{\overrightarrow{\rho E}+\vec{p}}{\vec{\rho}}\circ\left(\mathbf{D}^\dagger_{1x_i}\vec{Q}^\dagger_5\right) - (\gamma-1)\,(\vec{u}_i\circ\vec{u}_j)\circ\left(\mathbf{D}^\dagger_{1x_j}\vec{Q}^\dagger_5\right) - \frac{1}{\text{Re}}\frac{\mathbf{L}^\dagger\left(\vec{Q}^\dagger_{i+1} - \vec{u}_i\circ\vec{Q}^\dagger_5\right)}{\vec{\rho}} \\
&+ \frac{\gamma}{\text{RePr}}\frac{\vec{u}_i}{\vec{\rho}}\circ\left(\mathbf{L}^\dagger\vec{Q}^\dagger_5\right) - \frac{1}{\text{Re}}\left(\frac{\mathbf{L}\vec{u}_i + \frac{1}{3}\mathbf{E}_{ij}\vec{u}_j}{\vec{\rho}}\right)\circ\vec{Q}^\dagger_5 - \frac{1}{3\text{Re}}\frac{\mathbf{E}^\dagger_{ji}\left(\vec{Q}^\dagger_{j+1} + \vec{u}_j\circ\vec{Q}^\dagger_5\right)}{\vec{\rho}} \\
&+ \frac{4}{3\text{Re}}\frac{\mathbf{D}^\dagger_{1x_i}\left[(\mathbf{D}_{1x_j}\vec{u}_j)\circ\vec{Q}^\dagger_5\right]}{\vec{\rho}} - \frac{2}{\text{Re}}\frac{\mathbf{D}^\dagger_{1x_j}\left[(\mathbf{D}_{1x_i}\vec{u}_j + \mathbf{D}_{1x_j}\vec{u}_i)\circ\vec{Q}^\dagger_5\right]}{\vec{\rho}}, \quad\text{for } i=1,2,3, \\
\vec{\mathsf{R}}^\dagger_{\text{interior},5}\left[\vec{Q},\vec{Q}^\dagger\right] &= (\gamma-1)\,\mathbf{D}^\dagger_{1x_i}\vec{Q}^\dagger_{i+1} + \gamma\vec{u}_i\circ\left(\mathbf{D}^\dagger_{1x_i}\vec{Q}^\dagger_5\right) - \frac{\gamma}{\text{RePr}}\frac{\mathbf{L}^\dagger\vec{Q}^\dagger_5}{\vec{\rho}}, \quad\quad\quad\quad\quad (7.12)
\end{aligned}
$$

with the following notation for adjoint discrete derivative operators:

$$\mathbf{D}^\dagger_{ix_j} = \mathbf{P}^{-1}\mathbf{D}^\mathrm{T}_{ix_j}\mathbf{P}$$

$$\mathbf{L}^\dagger = \mathbf{P}^{-1}\mathbf{L}^\mathrm{T}\mathbf{P}$$

$$\mathbf{E}^\dagger_{ij} = \mathbf{P}^{-1}\mathbf{E}^\mathrm{T}_{ij}\mathbf{P}.$$

The computational cost of the fully discrete adjoint method is connected to the choice of discretization of the forward model. Our fully discrete adjoint method is modestly more computationally expensive than the continuous-adjoint method, which we quantify for discussion here based upon the number of field derivatives, since these constitute most of the computational effort. For a three-dimensional problem, there are 72

derivative operators in (7.12), compared to the discretization of (7.11), which requires only 54. The additional terms are not in the corresponding continuous formulation because continuous first- and second-derivative operators are skew-Hermitian and Hermitian, respectively, which affords cancellation of certain combinations of terms that result from the integration-by-parts procedure. The same cancellation is not exact for discrete operators, which leads to (7.12), and a modest increase in required operations. The expression has been simplified to exploit the linearity and distributive properties of the adjoint discrete derivative operators. It can be further simplified in some obvious ways to exploit the properties of SBP operators, but we do not pursue this in detail since we wish to retain the generality of (7.12) for a broader class of explicit finite-difference operators.

Figures 7.12 to 7.16 show visualizations of the fully discrete adjoint fields. The adjoint equations are forced in the target region, which is in the acoustic field. Since the flow equations are self-adjoint in the acousic limit, these quantities are expected to behave approximately like a sound wave until they interact with the mixing layer.
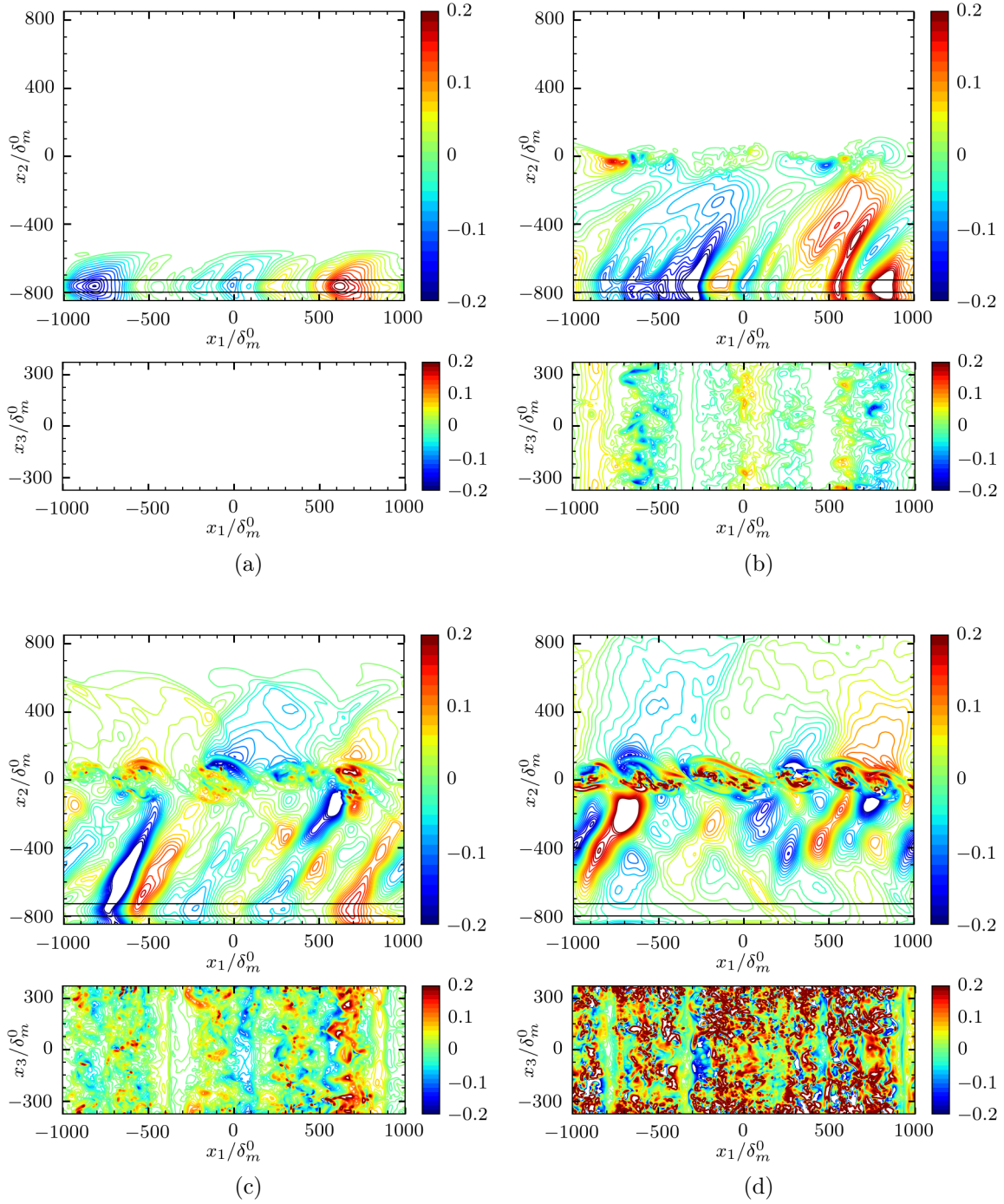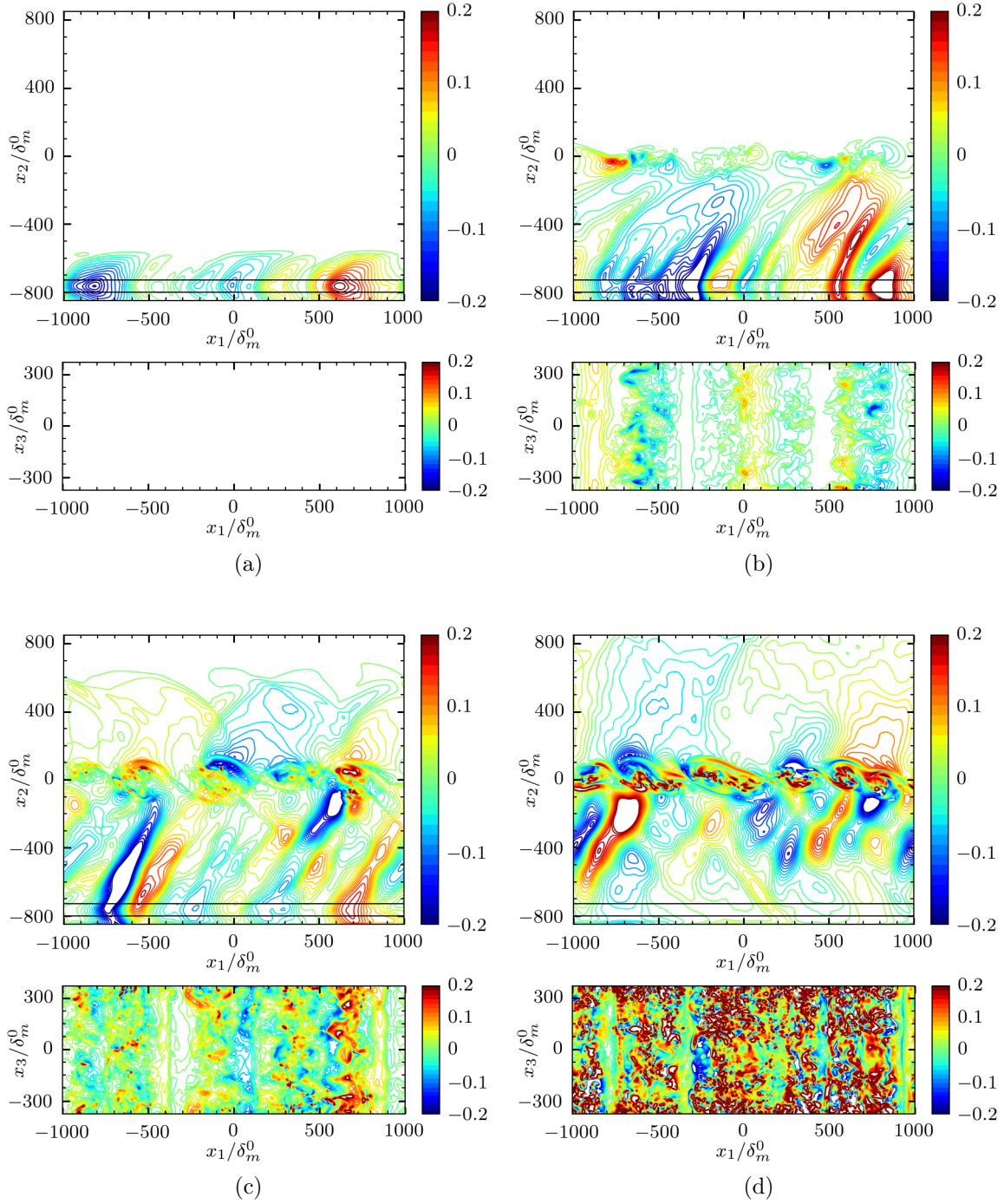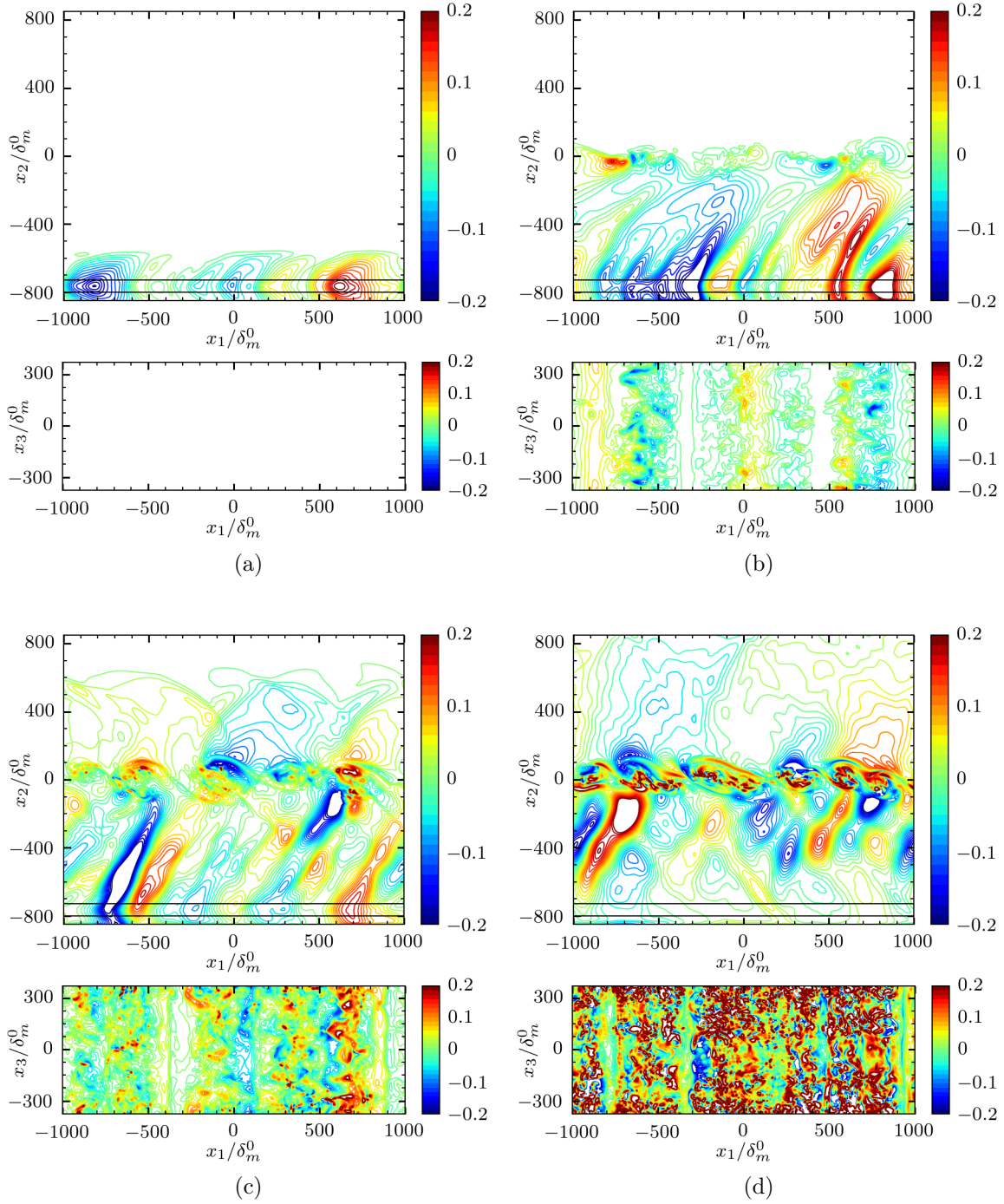
Figure 7.12: Visualization of $Q_1^\dagger(\boldsymbol{\xi}, t)$ from the fully discrete adjoint method along $x_3/\delta_m^0 = 0$ (top) and $x_2/\delta_m^0 = 0$ (bottom) at times (a) $(t - t_0)\,\Delta U/\delta_m^0 = 1620$, (b) $(t - t_0)\,\Delta U/\delta_m^0 = 1080$, (c) $(t - t_0)\,\Delta U/\delta_m^0 = 540$, and (d) $(t - t_0)\,\Delta U/\delta_m^0 = 0$. The solid black lines are the boundaries of finite W_Ω defined in (7.9), where the otherwise homogeneous adjoint equations are forced.
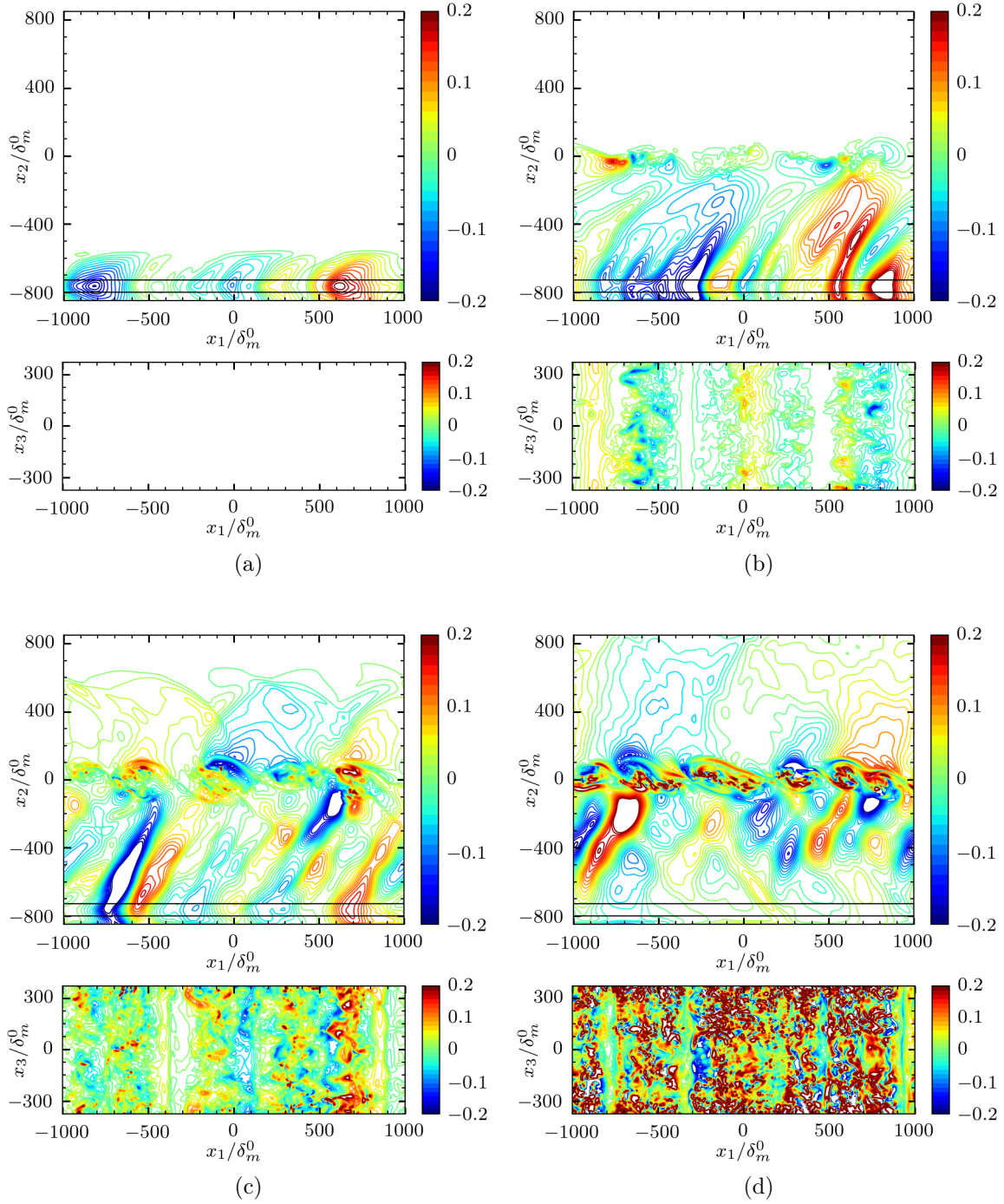
74

Figure 7.13: Visualization of $Q_2^\dagger(\boldsymbol{\xi}, t)$ from the fully discrete adjoint method along $x_3/\delta_m^0 = 0$ (top) and $x_2/\delta_m^0 = 0$ (bottom) at times (a) $(t - t_0)\,\Delta U/\delta_m^0 = 1620$, (b) $(t - t_0)\,\Delta U/\delta_m^0 = 1080$, (c) $(t - t_0)\,\Delta U/\delta_m^0 = 540$, and (d) $(t - t_0)\,\Delta U/\delta_m^0 = 0$. The solid black lines are the boundaries of finite W_Ω defined in (7.9), where the otherwise homogeneous adjoint equations are forced.

Figure 7.14: Visualization of $Q_3^\dagger(\boldsymbol{\xi}, t)$ from the fully discrete adjoint method along $x_3/\delta_m^0 = 0$ (top) and $x_2/\delta_m^0 = 0$ (bottom) at times (a) $(t - t_0)\,\Delta U/\delta_m^0 = 1620$, (b) $(t - t_0)\,\Delta U/\delta_m^0 = 1080$, (c) $(t - t_0)\,\Delta U/\delta_m^0 = 540$, and (d) $(t - t_0)\,\Delta U/\delta_m^0 = 0$. The solid black lines are the boundaries of finite W_Ω defined in (7.9), where the otherwise homogeneous adjoint equations are forced.
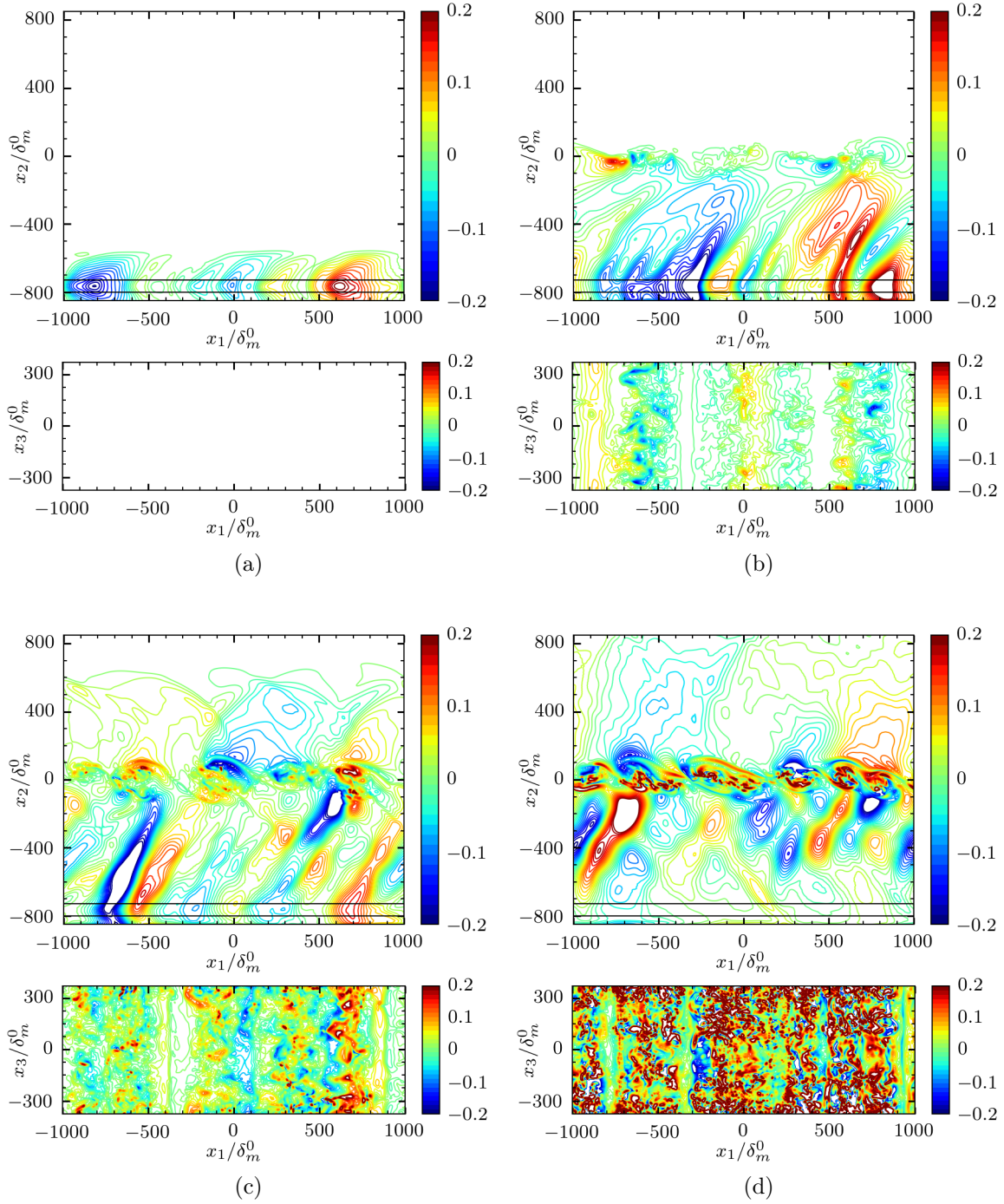
Figure 7.15: Visualization of $Q_4^\dagger(\boldsymbol{\xi}, t)$ from the fully discrete adjoint method along $x_3/\delta_m^0 = 0$ (top) and $x_2/\delta_m^0 = 0$ (bottom) at times (a) $(t - t_0)\,\Delta U/\delta_m^0 = 1620$, (b) $(t - t_0)\,\Delta U/\delta_m^0 = 1080$, (c) $(t - t_0)\,\Delta U/\delta_m^0 = 540$, and (d) $(t - t_0)\,\Delta U/\delta_m^0 = 0$. The solid black lines are the boundaries of finite W_Ω defined in (7.9), where the otherwise homogeneous adjoint equations are forced.
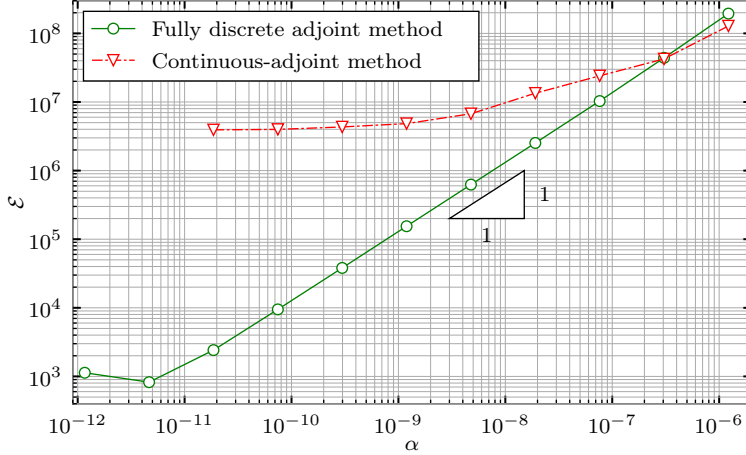
77

Figure 7.16: Visualization of $Q_5^\dagger(\boldsymbol{\xi}, t)$ from the fully discrete adjoint method along $x_3/\delta_m^0 = 0$ (top) and $x_2/\delta_m^0 = 0$ (bottom) at times (a) $(t - t_0)\,\Delta U/\delta_m^0 = 1620$, (b) $(t - t_0)\,\Delta U/\delta_m^0 = 1080$, (c) $(t - t_0)\,\Delta U/\delta_m^0 = 540$, and (d) $(t - t_0)\,\Delta U/\delta_m^0 = 0$. The solid black lines are the boundaries of finite W_Ω defined in (7.9), where the otherwise homogeneous adjoint equations are forced.

78

Figure 7.17: Comparison of gradient accuracy from the continuous and fully discrete adjoint formulations for the three-dimensional temporally developing mixing layer.

We now make an assessment based on the procedure described in Section 2.4 of the accuracy of the continuous and fully discrete formulations. Figure 7.17 shows the gradient error $\mathcal{E}$ from (2.22) for the three-dimensional temporally developing mixing layer. As $\alpha \to 0$, the continuous-adjoint formulation leads to an approximately constant $\mathcal{E}$, indicating that the dominant contribution to the gradient error is the $\mathcal{O}\left(\frac{1}{N_i^a}, \Delta t^b\right)$ term for the selected resolution. For the fully discrete adjoint simulation, $\mathcal{E} = \mathcal{O}\left(\alpha\right)$ up to an apparent round-off level. Based upon validation for a two-dimensional spatially developing mixing layer presented in Section 1, we can anticipate that the full discrete adjoint provides accuracy up to the point where finite-precision effects become important. Though such discrepancies are expected to grow relatively slowly for the relatively deterministic two-dimensional flow, a precise assessment of this is not possible.

Given that the shape of the cost functional in the control variable space is in general unknown, it is difficult to anticipate in detail the implications of an erroneous gradient for the convergence to the correct optimal control of the discrete model system. At best, errors will slow convergence by providing an erroneous amplitude in approximately the correct direction, but in general they will lead to the wrong optimal solution, which is more consequential. Thus, the error in gradient direction is specifically assessed via

$$\varphi\left(t\right) = \cos^{-1}\left(\frac{\left\langle \text{proj}\left(\mathcal{G}\left[Q_c^\dagger\right]\right), \vec{\mathsf{G}}\left[\vec{Q}_d^\dagger\right]\right\rangle_{\mathbf{P}}}{\left\|\text{proj}\left(\mathcal{G}\left[Q_c^\dagger\right]\right)\right\|_{\mathbf{P}} \left\|\vec{\mathsf{G}}\left[\vec{Q}_d^\dagger\right]\right\|_{\mathbf{P}}}\right), \tag{7.13}$$

where $\text{proj}\left(\mathcal{G}\left[Q_c^\dagger\right]\right)$ is the projection of the continuous-adjoint based sensitivity gradient on to the computional domain, and $\vec{\mathsf{G}}\left[\vec{Q}_d^\dagger\right]$ is the full discrete adjoint-based sensitivity gradient (evaluated at the discrete sub-steps). Figure 7.18 shows a plot of this angle as a function of time. At around $\left(t - t_0\right)\Delta U/\delta_m^0 = 1000$,
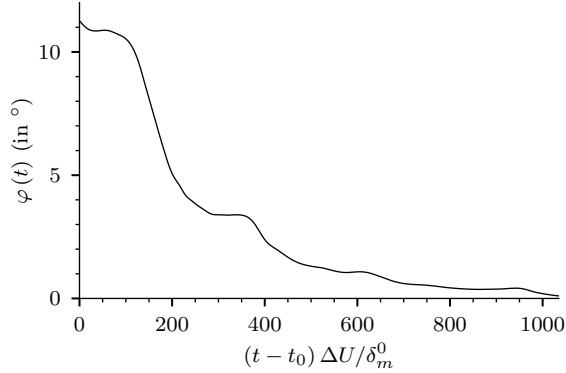
79

Figure 7.18: Time-dependent gradient direction error (7.13) for the three-dimensional temporally developing mixing layer.

the adjoint encounters the mixing layer and excites instabilities. Until this time, the magnitude of the sensitivity gradient, which has support in the control region located in the mixing layer, is trivially small. For $(t - t_0) \Delta U/\delta_m^0 < 1000$, the error in the direction of the continuous-adjoint based sensitivity gradient increases until it reaches its maximum value of about $10°$ at $t = t_0$., For the two-dimensional mixing spatially developing mixing layer demonstration in Section 1, the maximum value of $\varphi(t)$ was determined to be $1.2°$, which supports the rapid convergence of the continuous-adjoint based noise optimization achieved for that flow by Wei and Freund [90].

It is expected that any gradient errors will increase in time due to the usual sensitivity to initial conditions of a chaotic system. However, just how this occurs and how it affects the utility of any formulation for optimal flow control is unclear. Sound generation is primarily by the energetic large scales in a flow, and controlling these can be anticipated to be most important for its mitigation. So a gradient that is accurate for only low wavenumbers might still be able to provide the essential information for control optimization. Without a fundamental theory of turbulence, it is unlikely that general conclusions can be drawn in this regard, but an empirical assessment can be made for our model turbulent flow. Since $\mathrm{proj}\left(\mathcal{G}\left[Q_c^\dagger\right]\right)$ is obtained from an accurate discretization of (7.11), errors will be most pronounced at small scales. By comparison with the exact adjoint of the discretized system $\vec{\mathsf{G}}\left[\vec{Q}_d^\dagger\right]$, we can measure how these grow in time, as expected for a chaotic flow, and more importantly how they affect the accuracy of the arguably more important large-scale components of the gradient. Of course, this is an exercise rather than a direct concern since the fully discrete adjoint method we have derived will be preferable for this flow. However, not all models will be so amenable to a fully discrete adjoint formulation, so this specific question may be a practical concern in some circumstances. It is unclear, for example, that a general sub-grid-scale model of viscous dissipation or scalar transport for large-eddy simulation will necessarily be so easily expressed such that its discrete-
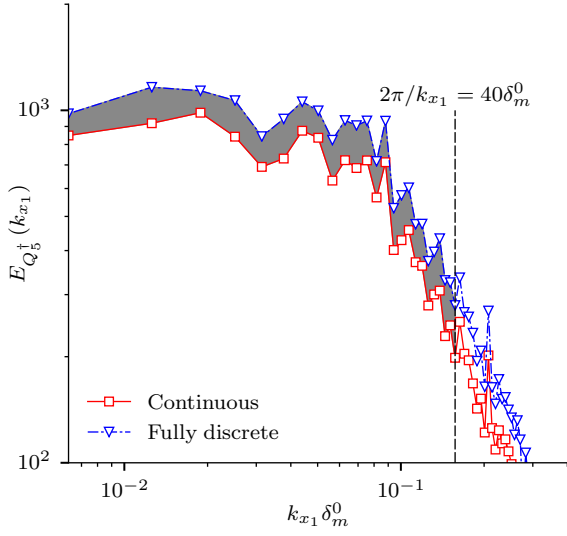
(a) Comparison of one-dimensional streamwise (x_1) energy spectra of $Q_5^\dagger(\boldsymbol{\xi}, t_0)$ at $x_2/\delta_m^0 = 0$ obtained from the continuous and fully discrete adjoint methods.
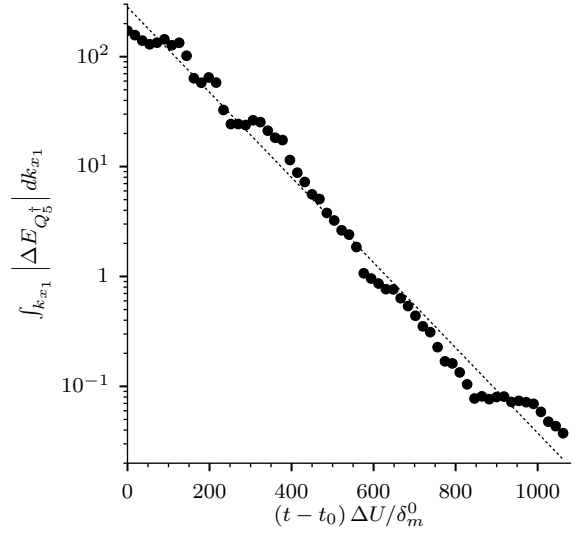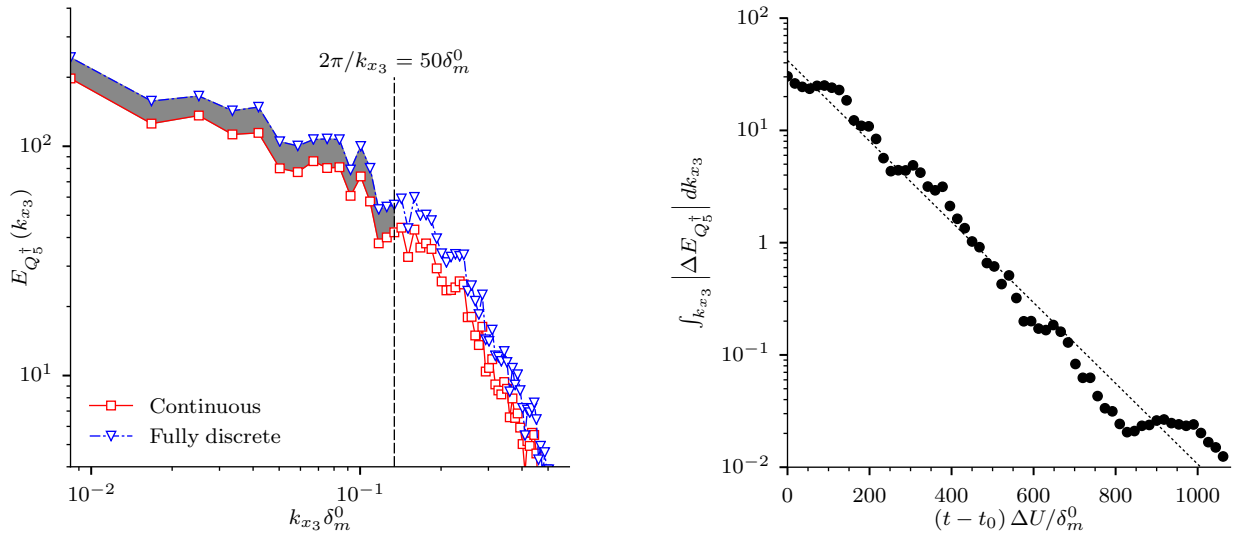
(b) Temporal evolution of the difference shown by the shaded region in (a) integrated with respect to the streamwise wavenumber k_{x_1}.

Figure 7.19: Streamwise wavenumber distribution of the error in the continuous-adjoint based sensitivity gradient and its exponential growth in reverse-time.

adjoint is efficient or even tractable. Thus, the accuracy of the continuous-adjoint is evaluated against the discrete-adjoint to anticipate challenges when the discrete-adjoint is unavailable.

To quantify the scale-dependence of the adjoint solution errors, the one-dimensional streamwise and spanwise energy spectra of the continuous and fully discrete adjoint fields $Q_5^\dagger(\boldsymbol{\xi}, t)$ are shown in Figure 7.19a and 7.20a, respectively. The magnitude of this difference averaged between the largest wavenumber and $k_{x_1} = 2\pi/40\delta_m^0$ in the streamwise direction, and $k_{x_3} = 2\pi/50\delta_m^0$ in the spanwise direction, are shown in Figures 7.19b and 7.20b, respectively. This quantity increases exponentially in reverse-time. It is clear that despite the initiation of errors at small scales, over the course of this simulation forcing of even the largest turbulence scales would be affected by continuous-adjoint errors (note that based on Figure 7.17, the error in the discrete-adjoint should be significantly smaller than any discretization errors). By separating turbulent fluctuations in flow quantities in (7.11) from their mean values, it can be shown that adjoint variables are transported like a passive scalar by the turbulent mean flow. This suggests the existence of an energy cascade mechanism for the energy norm for $Q_5^\dagger$, which is transported by the mean flow velocity. Since the adjoint equations are integrated in reverse-time, we should expect the cascade to transport energy from small to large spatial scales as the adjoint simulation proceeds. This is evident from Figures 7.19a and 7.20a, which show that the energy norm for the discrete-adjoint $Q_5^\dagger$ is consistently higher than the continuous-adjoint, and the difference is significant even at the largest spatial scales, against the nominal expectation that the exact

(a) Comparison of one-dimensional spanwise (x_3) energy spectra of $Q_5^\dagger(\boldsymbol{\xi}, t_0)$ at $x_2/\delta_m^0 = 0$ obtained from the continuous and fully discrete adjoint methods.

(b) Temporal evolution of the difference shown by the shaded region in (a) integrated with respect to the spanwise wavenumber k_{x_3}.

Figure 7.20: Spanwise wavenumber distribution of the error in the continuous-adjoint based sensitivity gradient and its exponential growth in reverse-time.

sensitivity of the largest spatial scales are accurately captured by the continuous-adjoint method. Thus, even if the sound generation and its control is expected to be relatively large-scale, the accumulation of discretization errors will potentially hinder efficacy. For longer simulation times, finite numerical precision errors are also anticipated to similarly propagate to all scales, though this would require longer simulation times than this particular flow is set up for.

7.7 Controlled Mixing Layer

Though the continuous-adjoint is clearly less accurate, the consequences of its errors cannot be completely anticipated because of the complexity of the turbulence. We therefore also analyze the beginning of a control optimization. A steepest descent line-search was performed with the sensitivity gradient obtained from the continuous- and discrete-adjoint methods to determine the effect of the error in sensitivity gradient on noise reduction. To find the local minimum along the descent direction, a minimum bracket is evaluated followed by a modification of Brent's method [64] that uses derivatives to isolate the minimum to a fractional precision of 0.01. Table 7.1 shows the values of the baseline cost functional, and the cost functional with a control corresponding to the local minimum obtained using this procedure with the continuous- and discrete-adjoint methods for one line-search. The gradient errors previously quantified are indeed important by this measure.

	$\mathcal{J} \times 10^5$ from (2.15)
Baseline (no control)	11.0
Continuous-adjoint control	10.2
Discrete-adjoint control	9.23

Table 7.1: Noise reduction for the turbulent temporally developing mixing layer after one line search based upon a single gradient.

The discrete-adjoint method achieves more than twice the reduction.

Chapter 8

Turbulent Jet Noise Control

To demonstrate the utility of the proposed dual-consistent formulation for high-fidelity discretizations, we now examine its application to turbulence control. We consider active control of the noise radiated by a Mach 1.3 turbulent jet using a thermal actuation. Figure 8.1 shows a schematic of the jet. Kim et al. [37] reduced the noise for an LES of this configuration by 3.5 dB in a loudest direction using a continuous-adjoint approach. Though this is a relatively modest reduction compared to what has been achieved for a two-dimensional mixing layer [90], it is understood that the chaotic nature of turbulence diminishes its controllability using even a flexible nozzle actuation. Moreover, adjoint-field errors due to the incompatibility of a continuous-adjoint with the discretization can potentially slow convergence to the optimal control, and more importantly, misdirect gradient-based optimizations [83]. It is not clear whether a space–time discrete-exact adjoint can provide better guidance, or by doing so, lead to greater reductions — developing and demonstrating the methods required for addressing this is the main objective of the current study.

8.1 Discretization

The computational domain for the jet simulation is divided into 5 non-overlapping blocks. Each block is discretized using a structured curvilinear mesh such that the grid lines are C^0 continuous across the interface between blocks. The computational grid is generated by extrusion of the two-dimensional section shown in Figure 8.2, along the x_3-direction. In total, there are 8 pairs of computational boundaries on which the interface condition described in Section 5.4 is enforced. We use an explicit RK4 scheme (3.16) for integrating the flow equations in time, for which the maximum allowed time step size is restricted by the maximum value of the local CFL number

$$\text{CFL} = J\Delta t \left(\sum_{i=1}^{3} |\hat{u}_i| + a\sqrt{\sum_{i=1}^{3} \tilde{\text{M}}_i^2} \right).$$
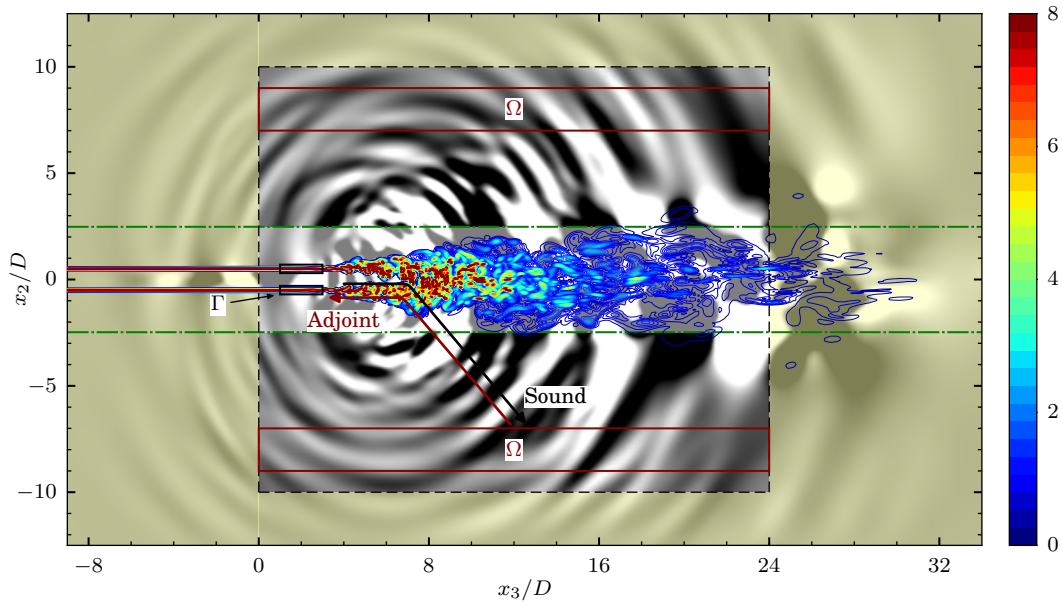
Figure 8.1: The Mach 1.3 turbulent jet with visualized using contours of vorticity magnitude and on the $x_1/D = 0$ plane. The target region Ω and control region Γ are the supports of $W_\Omega(\boldsymbol{\xi})$ and $W_\Gamma(\boldsymbol{\xi})$ defined in (8.5) and (8.6), respectively.
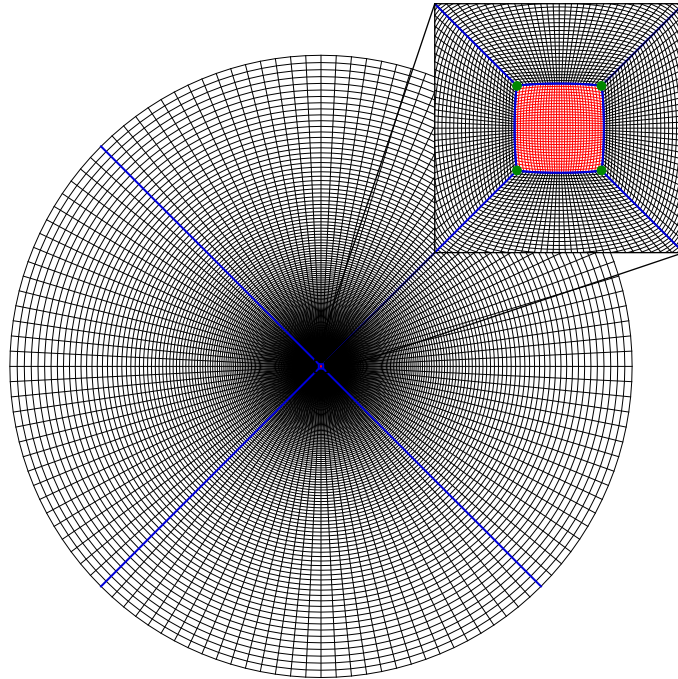

Figure 8.2: Axial cross-section of the computational grid used for the jet simulation. The interfaces between the blocks are shown (——). The maximum CFL number occurs on the 4 corners (●), where nodes from three blocks are duplicated.
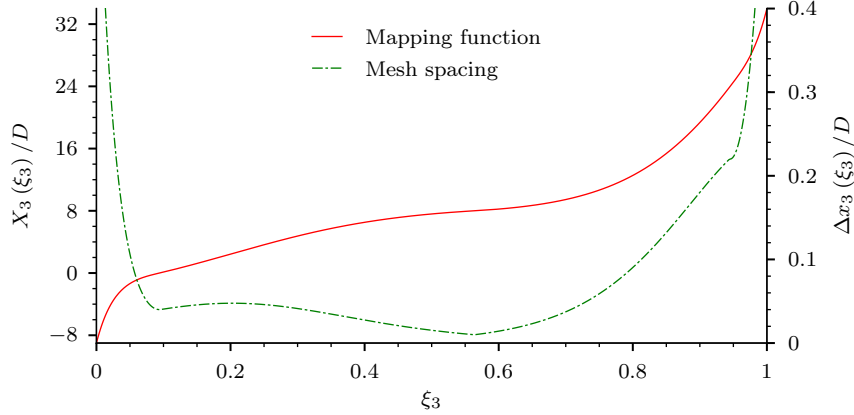
Figure 8.3: Mapping function for the axial coordinate $X_3(\xi_3)/D$ and axial mesh spacing $\Delta x_3(\xi_3)/D$ for the computational grid employed for the jet simulation.

For our desired distribution of grid points, this typically occurs at the intersection of three blocks shown in Figure 8.2. To permit greater flexibility in designing the grid, the interface between the "inner" block, which contains the centerline of the jet, and the remaining "outer" blocks is prescribed as

$$r\left(|\cos\theta|^p + |\sin\theta|^p\right)^{1/p} = 0.12D, \ -9D \le x_3 \le 34D, \tag{8.1}$$

where $r = |x_1 + ix_2|$ and $\theta = \arg(x_1 + ix_2)$ are the radial and azimuthal coordinates, respectively, and $p = 1.086$ is set heuristically to limit sharp changes in the CFL number across the block interfaces. This justifies the selection of a constant time step size for integrating the equations on all blocks. Each block is discretized using 512 points in the x_3-direction, with the mesh spacing and mapping function shown in Figure (8.3). The minimum spacing in this direction is $\Delta x_3 = 0.01D$ at $x_3 \approx 8D$. The outer blocks are each discretized using $N_r \times N_\theta = 256 \times 33$ points in the radial and azimuthal directions, respectively. Grid points are distributed uniformly in the azimuthal direction, and the grid lines in this direction satisfy (8.1), where p varies smoothly from 1.086 at the interface with the inner block, to 2 at $r = 0.5D$. For $r \ge 0.5D$, the grid lines are concentric circular arcs, so designed to facilitate post-processing. Within the inner block, 33×33 grid points are distributed smoothly by solving a Laplace equation for the transformation functions $X_i(\xi_1, \xi_2)$ using a second-order central-difference approximation, for $i = 1, 2$. In total, the computational grid consists of approximately 18 million points.

An SBP 2–4 scheme is employed for the spatial discretization per (3.12). Mild artificial dissipation is included per (3.12) and (3.7) with $\sigma_{\text{diss.}} = 0.1$. The Reynolds number based on the nozzle exit velocity is $\text{Re}_j = \rho_j U_j D/\mu_j = 1 \times 10^6$, and the Prandtl number is 0.72.

8.2 Simulation Details

In the axial direction, inflow/outflow boundary conditions are enforced on the computational domain boundaries at $x_3/D = -9$ and $x_3/D = 34$ using the procedure described in Section (5.1). A damping term per (5.7) with strength $\sigma_{\text{sponge}} = 0.5$ has support in sponge zones: $-9 \leq x_3/D \leq 0$ (inflow) and $24 \leq x_3/D \leq 34$ (outflow). In the radial direction, the computational domain boundary at $r/D = 12.5$ is treated using the same procedure with a damping term with identical strength that has support in a sponge zone $10 \leq r/D \leq 12.5$. The target state for the damping term is

$$u_1 = u_2 = 0$$

$$u_3 = \frac{1}{2} U_0 \left\{ 1 + \tanh \left[\frac{1}{4\theta_0} \left(\frac{r}{r_0} - \frac{r_0}{r} \right) \right] \right\}$$

$$\rho = \rho_\infty \left[\frac{\gamma - 1}{2} \frac{u_3}{a_\infty} \left(\frac{U_0 - u_3}{a_\infty} \right) \frac{T_\infty}{T_0} + \frac{u_3}{U_0} + \frac{T_\infty}{T_0} \left(1 - \frac{u_3}{U_0} \right) \right]^{-1}, \tag{8.2}$$

where density is related to streamwise velocity through the Crocco–Busemann relation. In (8.2), U_0, T_0, θ_0 and r_0 are empirical functions of the axial coordinate x_3/D, obtained by a least-squares curve-fit of the Reynolds-averaged Navier–Stokes (RANS) solution from Kim et al. [37], which explicitly includes the nozzle. This is prefered to directly interpolating the RANS solution onto the present computational grid since the RANS solution is available at a significantly coarser resolution. The specific form of these empricial functions

are:

$$U_0 = \begin{cases} U_j, & -9 \leq x_3/D \leq 2.65 \\ U_j \exp\left[-\left(\frac{x_3/D-2.65}{25}\right)\right], & 2.65 \leq x_3/D \leq 34 \end{cases}$$

$$\theta_0/D = \begin{cases} 0.04, & -9 \leq x_3/D \leq 0 \\ 0.04 + 0.46 x_3/24D, & 0 \leq x_3/D \leq 24 \\ 0.5, & 24 \leq x_3/D \leq 34 \end{cases}$$

$$r_0/D = \begin{cases} 0.5, & -9 \leq x_3/D \leq 0 \\ 0.5 + 0.04125 x_3/D, & 0 \leq x_3/D \leq 24 \\ 0.075 x_3/D - 0.31, & 24 \leq x_3/D \leq 34 \end{cases}$$

$$T_\infty/T_0 = \begin{cases} 1 + \frac{\gamma-1}{2}\text{Ma}^2, & -9 \leq x_3/D \leq 0 \\ 1 + \frac{\gamma-1}{2}\text{Ma}^2 \exp\left(-0.078 x_3/D\right), & 0 \leq x_3/D \leq 34, \end{cases}$$

where U_j is the streamwise nozzle-exit velocity and $\text{Ma} = 1.3$.

To achieve realistic transition to turbulence, we add small-amplitude instability modes of the form $Q'\left(\mathbf{x}, t\right) = \hat{Q}\left(r\right)\exp\left[i\left(\alpha x_3 + n\theta - \omega t + \phi\right)\right]$ in the inflow sponge zone. The procedure for doing this is documented in detail by Kim et al. [37]. Figure 8.4 shows the dispersion relations for the instability modes used.

8.3 Uncontrolled Jet Validation

Starting from an initial condition identical to the target state (8.2), the semi-discrete form of the governing equations (3.15) are advanced using the RK4 scheme (3.16) from $ta_\infty/D = 0$ to $ta_\infty/D = 480$. This corresponds to $20\times$ the time taken for acoustic waves to travel across the streamwise length of the domain. We use a constant time step size $\Delta t a_\infty/D = 1.2 \times 10^{-3}$, which results in a maximum CFL number of approximately 0.5. By $ta_\infty/D = 480$, the jet has reached a statistically stationary state. Statistics are then collected from $ta_\infty/D = 480$ to $ta_\infty/D = 1320$ at a frequency $\text{St}_D \approx 21.4$, which provides sufficiently high temporal resolution for resolving the jet turbulence [37]. Overall, 20000 samples are collected.

The Reynolds average of a quantity $\varphi\left(\boldsymbol{\xi}, t\right)$ is denoted as $\overline{\varphi}\left(\boldsymbol{\xi}\right)$. For $r < 0.5D$, it is obtained by averaging
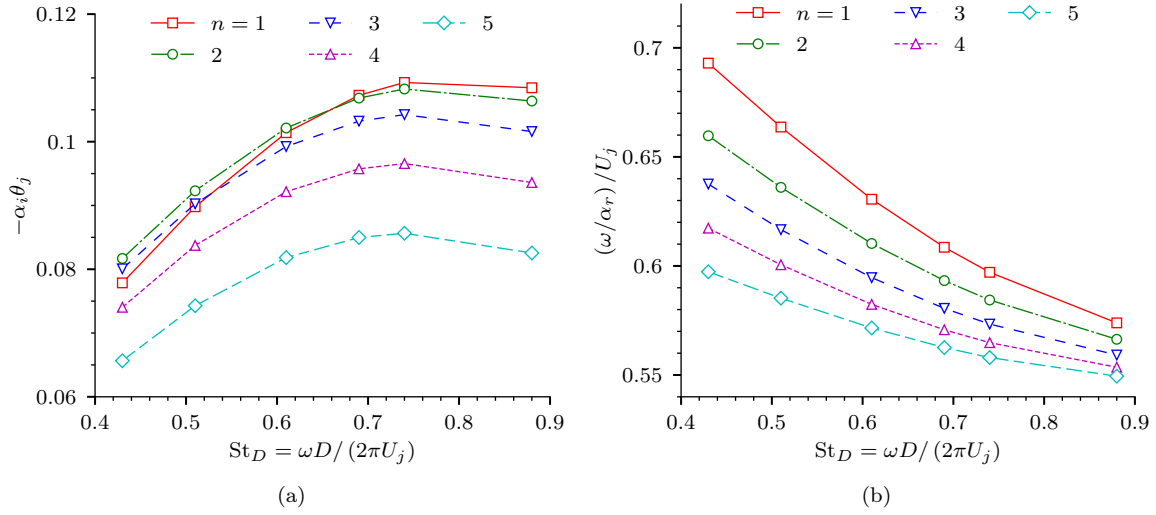
88

Figure 8.4: (a) Streamwise growth rate $-\alpha_i \theta_j$ and (b) phase speed $(\omega/\alpha_r)/U_j$ of instability modes. α_r and α_i are the real and imaginary parts of the complex streamwise wavenumber α, respectively, and $\theta_j = 0.04D$ is the momentum thickness.

only in time. For $r \geq 0.5D$, the grid lines form concentric circles with uniform mesh spacing in the azimuthal direction. Hence, the Reynolds average for $r \geq 0.5D$ is obtained by averaging both in time and the azimuthal coordinate θ. The Favre average is $\widetilde{\phi} = \overline{\rho\phi}/\overline{\rho}$.
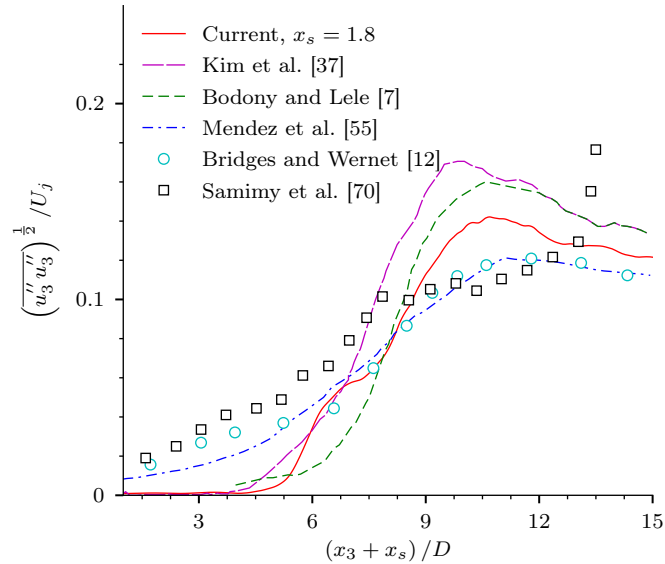
Figure 8.5 shows a comparison of centerline statistics with other numerical and experimental data for similar jet conditions. Since our simulation does not employ a nozzle, an approximate nozzle exit location is determined by shifting the axial coordinate such that the jet potential core length, defined by the axial location where the mean streamwise velocity is $0.95U_j$, matches the value $x_3/D \approx 8.5$ measured by Samimy et al. [70]. The resulting shifting distance is $x_s/D = 1.8$. Figure 8.5a shows excellent agreement between the Favre-averaged centerline streamwise velocity for the present jet with experimental data [70]. Root-mean-square fluctuations of the streamwise velocity along the centerline are shown in Figure 8.5b. Reasonable agreement is observed as is typical for simulations that do not include a nozzle [7, 11, 37], but instead the inflow excitation is modeled using instability waves.

Figure 8.6 shows a comparison of $\widetilde{u}_3$ along the $r/D = 0.5$ nozzle lipline. The agreement with experimental data is imperfect in the potential core region, presumably due to the fact the prescribed inflow disturbances do not precisely represent the behavior of an actual nozzle. However, the agreement improves considerably downstream suggesting that this is a sufficiently realistic model for the important downstream turbulence.

Before using the proposed adjoint formulation for suppressing jet noise, it is important to validate the predictive model. We do this by comparing far-field sound spectra with experiment for the baseline jet simulated without any control forcing. The acoustic field of the jet, where the decay of acoustic intensity
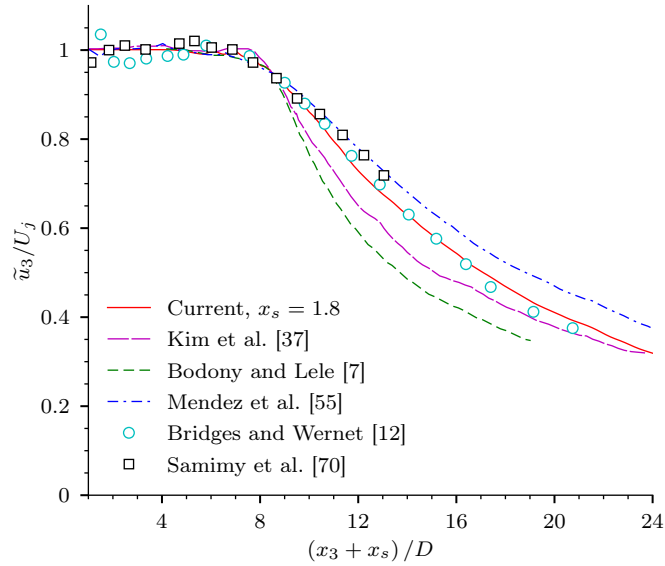
Figure 8.5: Comparison of centerline turbulence statistics: (a) Favre-averaged streamwise velocity $\tilde{u}_3 = \overline{\rho u_3}/\overline{\rho}$, and (b) root-mean-square of fluctuations $u_3^{''} = u_3 - \tilde{u}_3$, for the current simulation (——) with Kim et al. [37] (———), Bodony and Lele [7] (-- --), Mendez et al. [55] (-·-·-), Bridges and Wernet [12] (○), and Samimy et al. [70] (□), where $x_s/D = 1.8$ for the current simulation, 2.3 for Kim et al. [37], and 4.0 for Bodony and Lele [7].
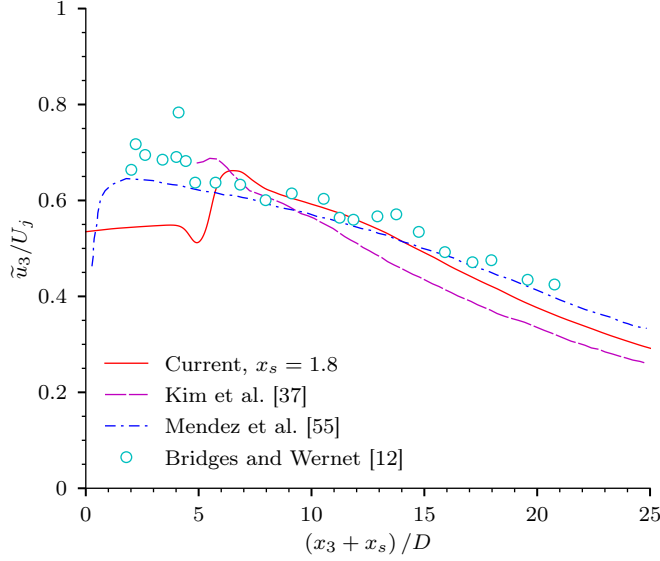
Figure 8.6: Comparison of Favre-averaged streamwise velocity $\tilde{u}_3 = \overline{\rho u_3}/\overline{\rho}$ on the $r/D = 0.5$ nozzle lipline for the current simulation (——) with Kim et al. [37] (———), Mendez et al. [55] (–·–·–), and Bridges and Wernet [12] (○), where $x_s/D = 1.8$ for the current simulation, 2.3 for Kim et al. [37], and 4.0 for Bodony and Lele [7].

follows an inverse-square law, is located outside our finite-size simulation domain. The location of the experimental measurements of sound spectra from Samimy et al. [70] are also well beyond the radial extent of the domain $r/D = 10$. Far-field sound outside the computational domain can be measured from near-field simulation data using the Ffowcs-Williams-Hawkings (FWH) integral surface method. The method and its application to this jet are documented in detail by Kim [36]. The present implementation of the FWH method has been verified by reproducing the far-field pressure fluctuation and sound pressure level (SPL) for point monopole and dipole sources (not shown here). The SPL for the present jet is

$$\text{SPL (dB)} = 10 \log_{10} \frac{\hat{p}\hat{p}^*}{p_{\text{ref}}^2} - 10 \log_{10} \left(\frac{d_e}{d}\right)^2 - 10n \log_{10} \left(\frac{U_j}{a_\infty}\right) + 10 \log_{10} \Delta f, \tag{8.3}$$

where $\hat{p}$ is the Fourier transform of the far-field pressure fluctuation obtained using the FWH method and $\hat{p}^*$ is its complex conjugate; $p_{\text{ref}} = p_{\text{ref}}^\star/\rho_\infty^\star a_\infty^{\star 2}$, where $p_{\text{ref}}^\star = 20\,\mu\text{Pa}$ is the usual reference pressure corresponding to the acoustic pressure audible to the human ear; $d_e = 80D$ is a common measurement location used for scaling the SPL for different directivity angles ϕ; $d = 94D$ for $\phi = 30°$ and $d = 44D$ for $\phi = 90°$ are the distances from the nozzle exit to the location of the microphones used in the experiment; $n = 8$ is the exponent of velocity in Lighthill's U_j^8 law for acoustic intensity, which normalizes the effect of different jet velocities; and Δf is the sampling frequency $f \approx 23.8a_\infty/D$ divided by the number of samples ($= 20000$).

Figure 8.7 shows a comparison of the SPL (8.3) for the present simulation with the experiment of Samimy

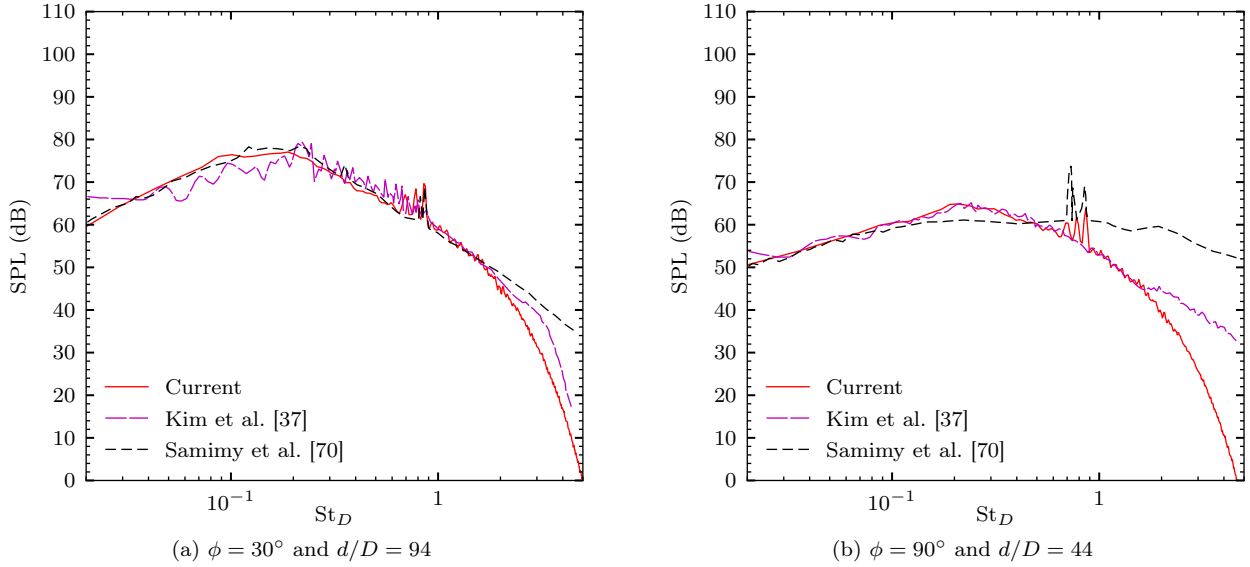(a) $\phi = 30°$ and $d/D = 94$ (b) $\phi = 90°$ and $d/D = 44$

Figure 8.7: Sound pressure level for the perfectly-expanded Mach 1.3 jet. Spectra are projected to a common distance $80D$.

et al. [70] and the LES of Kim et al. [37]. The agreement for $\phi = 30°$ is within 1 dB for up to $\text{St}_D \approx 2$ beyond which it falls off due to the finite temporal resolution of the measurement. Similarly, good agreement is obtained for $\phi = 90°$, for which the present method correctly predicts the peak at $\text{St}_D \approx 0.8$. These results and the agreement of turbulence statistics shown earlier indicate that the predictive model (3.12) is a high-fidelity representation of the jet's turbulence and is able to accurately predict its far-field sound.

8.4 Cost Functional and Control Implementation

A cost functional that measures the radiated jet noise from (2.14) and (2.15) is

$$\mathcal{J}[Q] = \int_{t=t_0}^{t_1} \int_{\boldsymbol{\xi} \in \mathbb{D}} |p(\boldsymbol{\xi}, t) - \bar{p}(\boldsymbol{\xi})|^2 \, W_\Omega(\boldsymbol{\xi}) \, \frac{1}{J(\boldsymbol{\xi})} d^3\boldsymbol{\xi} dt, \tag{8.4}$$

where $\bar{p}(\boldsymbol{\xi})$ is the time-averaged pressure, and the control time horizon extends from $t_0 a_\infty / D = 1140$ to $t_1 a_\infty / D = 1190.4$. During this time horizon, acoustic waves can travel across the streamwise length of the domain twice, and between the control and target regions 4 times. This is long enough to include about 12 jet column mode periods [16], but a relatively small interval compared to the one used by Kim et al. [37]. Figure 8.8 visualizes the jet using contours of vorticity magnitude and dilatation along a longitudinal section of the cylindrical computational domain at the beginning and end of the control horizon. In (8.4),
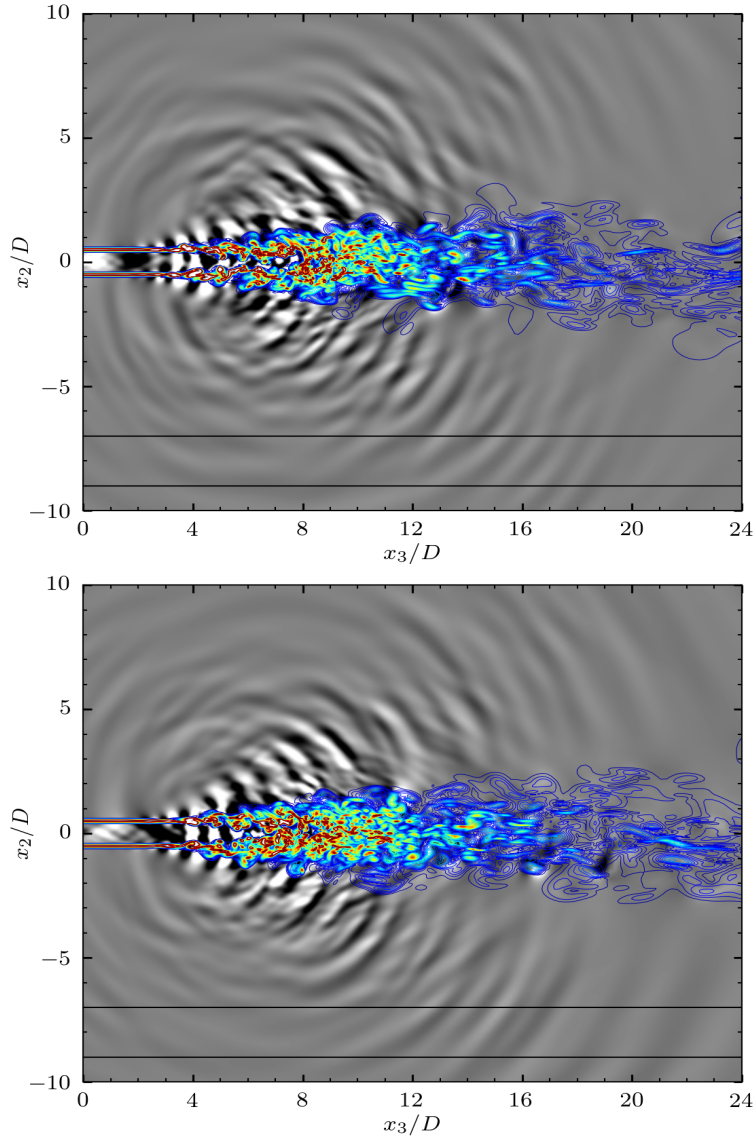
Figure 8.8: Visualization showing contours of vorticity magnitude and dilatation along $x_1/D = 0$ at $t = t_0 = 1140D/a_\infty$ (top) and $t = t_1 = 1190.4D/a_\infty$ (bottom) for the Mach 1.3 perfectly-expanded jet. The solid black lines are the boundaries of finite W_Ω defined in (8.5), where the radiated sound is measured.

the target mollifying support function $W_\Omega (\boldsymbol{\xi})$ is

$$W_\Omega (\boldsymbol{\xi}) \sim B_{0,2} \left(r^\Omega\right) \left\{\tanh\left[80\left(x_3^\Omega - 0.05\right)\right] - \tanh\left[80\left(x_3^\Omega - 0.95\right)\right]\right\}, \tag{8.5}$$

where

$$r^\Omega = \begin{cases} \frac{1}{2}\left(\frac{r}{D} - 7\right), & \left|\frac{r}{D} - 8\right| \leq 1 \\ 0, & \text{otherwise}, \end{cases}$$

$$x_3^\Omega = \begin{cases} \frac{x_3}{24D}, & \left|\frac{x_3}{D} - 12\right| \leq 12 \\ 0, & \text{otherwise}, \end{cases}$$

and $\int_{\boldsymbol{\xi} \in \mathbb{D}} W_\Omega (\boldsymbol{\xi}) \frac{1}{J(\boldsymbol{\xi})} d^3\boldsymbol{\xi} = 1$.

The control for this demonstration is a thermal actuation that appears on the RHS of the governing equations (2.19). The control mollifying support function is

$$W_\Gamma (\boldsymbol{\xi}) \sim \left\{\tanh\left[40\left(r^\Gamma - 0.05\right)\right] - \tanh\left[40\left(r^\Gamma - 0.95\right)\right]\right\} \left\{\tanh\left[32\left(x_3^\Gamma - 0.05\right)\right] - \tanh\left[32\left(x_3^\Gamma - 0.95\right)\right]\right\}, \tag{8.6}$$

where

$$r^\Gamma = \begin{cases} \frac{1}{0.4}\left(\frac{r}{D} - 0.3\right), & \left|\frac{r}{D} - 0.5\right| \leq 0.2 \\ 0, & \text{otherwise}, \end{cases}$$

$$x_3^\Gamma = \begin{cases} \frac{1}{2}\left(\frac{x_3}{D} - 1\right), & \left|\frac{x_3}{D} - 2\right| \leq 1 \\ 0, & \text{otherwise}, \end{cases}$$

and $\int_{\boldsymbol{\xi} \in \mathbb{D}} W_\Gamma (\boldsymbol{\xi}) \frac{1}{J(\boldsymbol{\xi})} d^3\boldsymbol{\xi} = 1$. Overall, the control region spans about 4.2×10^5 grid points across all the blocks. The total number of independent control parameters is about 71 billion. Some grid points on the control region lie on the interfaces between blocks, and thus, are duplicated. We do not explicitly constrain the control forcing on the duplicated nodes to be equal — aside from the interface adjoint conditions imposed weakly by the adjoint SAT (4.13).

For convenience in documenting results, we define the instantaneous cost functional

$$\mathcal{I}[Q](t) = \int_{\boldsymbol{\xi} \in \mathbb{D}} \left|p(\boldsymbol{\xi}, t) - \bar{p}(\boldsymbol{\xi})\right|^2 W_\Omega (\boldsymbol{\xi}) \frac{1}{J(\boldsymbol{\xi})} d^3\boldsymbol{\xi}, \tag{8.7}$$

so that (8.4) is $\mathcal{J}[Q] = \int_{t=t_0}^{t_1} \mathcal{I}[Q](t)$, which is the area under the $\mathcal{I}[Q](t)$ versus t curve between $t = t_0$
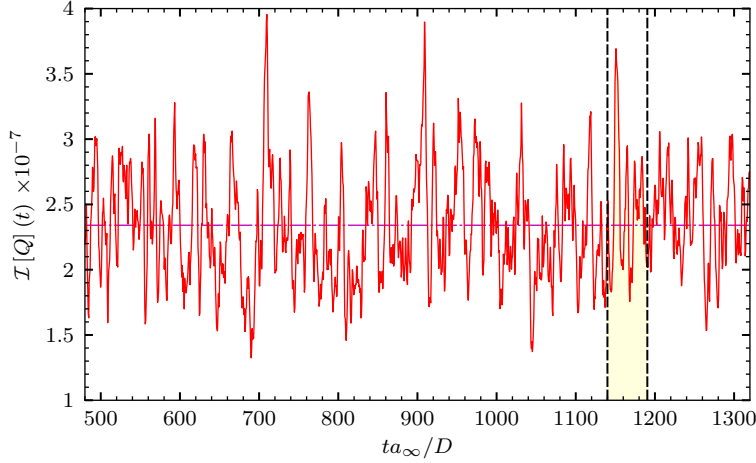
Figure 8.9: Instantaneous cost functional $\mathcal{I}[Q]$ (8.7) versus time for the entire simulation history for the turbulent jet. The horizontal dash-dot line indicates the mean value of $\mathcal{I}[Q]$.
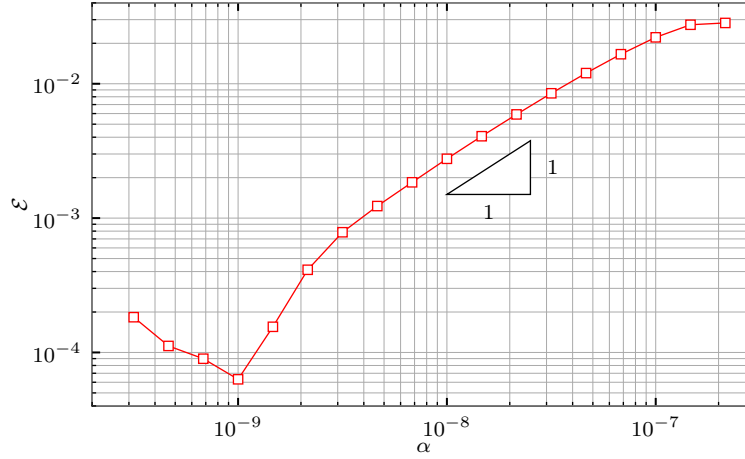
Figure 8.10: Gradient accuracy based on (2.22) for the jet simulation using a discrete-exact and consistent formulation.

and $t = t_1$. Figure 8.9 shows the instantaneous cost functional versus time for the entire simulation, where the area under the shaded region gives the value of $\mathcal{J}[Q]$. The profile is characterized by intermittent peaks of high acoustic intensity with periods of relatively low acoustic energy. This observation is consistent with previous studies [37, 7].

8.5   Gradient Accuracy

We assess the accuracy of the gradient using the error $\mathcal{E}$ introduced in Section 2.4. Figure 8.10 shows a plot of $\mathcal{E}$ versus α for the present jet. For the highest value of α shown, the amplitude of the control forcing is

Figure 8.11: Comparison of gradient accuracy based on (2.22) for the two-dimensional mixing layer schematically shown in Figure (7.1). The multi-block grid is obtained by splitting along the $x_1/\delta_w^0 = 50$ line the grid used for the single-block simulation.

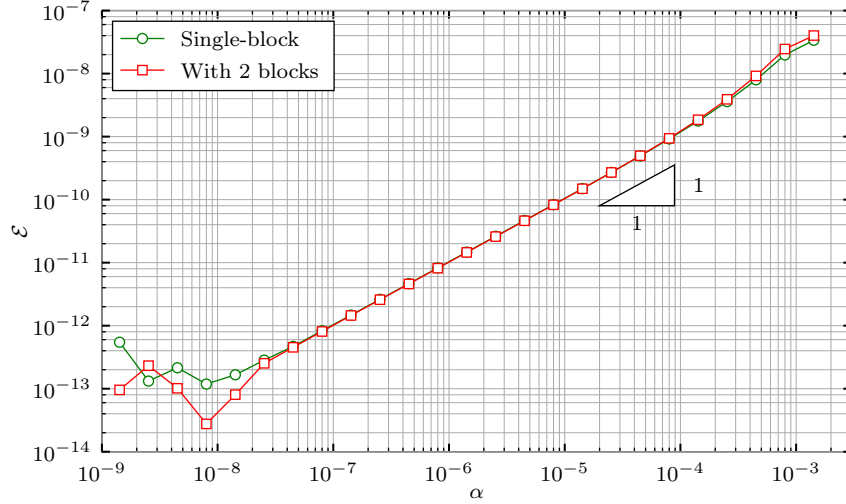presumably too high for the asymptotic expansion (2.21) to hold. This is followed by about three decades of change in α where $\mathcal{E} = \mathcal{O}(\alpha)$ until an apparent roundoff limit is reached. Without significantly more computational effort, it is difficult to establish this precisely as discussed in Section 6.2.

The quadruple-precision result for the unsteady simulation of a two-dimensional mixing layer shown in Figure 6.8 tests the same numerical solver for correctness including nonlinear terms and transient behavior, but excluding the interface SAT (5.21). We therefore repeated that simulation using a grid consisting of two blocks and an interface along the $x_1/\delta_w^0 = 50$ line, with otherwise the same setup shown in Figure 7.1. At the interface, the SAT (5.21) enforces conservation. Figure 8.11 shows the gradient error $\mathcal{E}$ (2.22) for the simulation performed using 64-bit (double-precision) arithmetic. For comparison, the gradient error for the single-block simulation using the same configuration is also shown. The results indicate that the formulation including the interface penalty SAT yields a discrete-exact gradient as expected for a multi-block problem.

Chapter 9

Conclusions

The potential advantages of a discrete-adjoint formulation for the three-dimensional compressible flow equations were well understood at the outset. The advance of our new formulation is that it provides the exact (precision-limited) gradient for the same highly accurate workhorse methods commonly used for simulating compressible turbulence, particularly in aeroacoustics simulations. The formulation is crafted such that it exploits the properties of adjoint discrete derivative operators in algebraic combinations that produce an efficient computational code. Such opportunities are generally missed by current automatic differentiation tools because they involve combinations that are not easy for such tools to identify based upon a numerical implementation. At the same time, the operations mirror those that would be followed for a comparable discretization of the continuous-adjoint equations, and thus do not demand any intricate operations beyond those already available for the flow solution or its adjoint if a discretization of it is already available. Although our demonstrations are oriented around aeroacoustics applications, the utility of the adjoint formulation presented in Chapter 4 extends to other high-fidelity applications, since it is independent of the choice of cost functional.

The dual-consistent discretization we have designed leads to a smooth discrete-exact adjoint field because its discrete-adjoint is consistent with the adjoint of the continuous system. In addition, it conserves global quantities including the total mass, momentum and energy of the system up to the order of accuracy of the interior stencil of the discrete derivative operators. Many industrial codes that solve the compressible flow equations choose to employ finite-volume methods, mainly because of their ability to exactly preserve conserved quantities in a global sense. Our dual-consistent formulation offers the traditional advantages of a finite-difference method, including low dispersion errors, and relatively easy, efficient and scalable implementation, while simultaneously offering high-order approximation of the *integral* form of the conservation laws. The SBP property we require for the discrete derivative operators is key to this result and is sufficient for periodic domains, but we have shown how to achieve this through dual-consistent SATs derived in Chapter 5 that weakly enforce boundary conditions most commonly used for simulations of compressible flows.

To be useful for DNS of turbulence, the discretization (3.12) must be modified to employ a narrow-stencil

second-derivative approximation, which damps the highest wavenumber mode supported by the computational grid. An example of such a discretization is given in Section 7.2 and has been demonstrated for a turbulent mixing layer, but it is not dual-consistent. Mattsson [52] recently proposed SBP operators that approximate second derivatives with variable coefficients and efficiently damp the highest wavenumber modes. Thus, they can be used for discretizing the viscous term in (3.12) without the addition of artificial dissipation. Their SBP property and Lemma 5.2 ensure that the dual-consistency conditions derived for the SATs in Chapter 5 hold, and the SATs we derived may be used in conjunction with a discretization based on these narrow-stencil operators.

Our dual-consistent formulation is valid for multi-block structured grids that intersect on a C^0-interface. The main advantage of such grids is that they require minimal communication of data between blocks and can be efficiently parallelized. The interface SAT (5.21) only requires data from the duplicate nodes shown in Figure 5.1. However, generating such grids can be challenging because the resolution of different blocks cannot be specified independently. An overset grid approach [5], also known as a Chimera approach, can address this by allowing multiple overlapping structured grids, whose resolution can be optimized independently. Communication between grids is handled through interpolation using coefficients that, for stationary grids, can be computed as a preprocessing step. This, however, is based on the injection method, and is not guaranteed to preserve the energy estimate of the discrete problem [76]. For strictly hyperbolic systems, Bodony et al. [8] developed a stable and accurate interpolation scheme using the overset grid approach, including examples of moving grids. Our formulation is readily extensible to overset grids, since stability requirements dictate that the interpolation operator must be based on the projection method and will appear as an SAT on the RHS of (3.12). The conditions for dual-consistency derived in Chapter 5 for commonly used boundary conditions are independent of this. However, corresponding conditions for dual-consistency will impose conditions on parameters in the interpolation penalty term, and must be established by proving Lemma 5.2 for the interpolation operator. Crafting such provably stable interpolation operators for incompletely parabolic IBVPs, e.g., the compressible flow equations, is a subject of ongoing research.

The fully discrete adjoint method we have derived is compatible with flexible multi-stage temporal discretizations of the flow equations (3.16), such as the fourth-order Runge–Kutta scheme we employ in our demonstrations. de Pando et al. [17] proposed a modular procedure for the evaluation of the semi-discrete-adjoint, which is advantageous for application to different governing equations, though it does not seem so easily extendable to include time discretization. The present formulation is time-exact, though more tied to the specific flow equations.

In Chapter 7, we presented a fully discrete adjoint method for a workhorse discretization of the com-

pressible flow equations by contrasting it with a discretization of the continuous-adjoint method to highlight the fact that it can be practically implemented with only a few changes. Though not dual-consistent, the formulation is modestly ($\sim 1.5 \times$) computationally more expensive than the continuous-adjoint method, and more effective in controlling aeroacoustic noise ($\sim 2.2 \times$ for our model mixing layer flow). It is similarly only $\sim 1.85\times$ more expensive than computing the flow solution. Practical implementation of this discrete-adjoint formulation relies on the fact that the discrete operators in (7.8) are local, and the bandwidth of the interior stencils do not change when transposed as in (7.12). The discrete-Fourier operators we use in x_3 are an exception, since their transpose yields also a discrete-Fourier operator. Thus (7.12) is useful for finite-differences, artificial dissipation based on high-order even derivatives, polynomial interpolation between overset grids and so on. However, spatially nonlocal operators such as dynamic large-eddy simulation (LES) models are not of this form. In this case, (7.12) will be most useful in a hybrid adjoint approach [80], in which a continuous formulation can be used for nonlocal operators, while retaining the discrete approach for the remaining terms in lieu of its compatibility with the discretized flow equations. Such an implementation would be straightforward since our choice of coefficients $\beta^{n,s}$ in (4.17) provide a fully-discrete adjoint (4.19) that is consistent with an RK4 discretization of the continuous-adjoint equations (4.20). Alternatively, for complicated nonlinear but relatively local operations, (7.12) can be used effectively in conjunction with automatic differentiation, which is less burdensome for such small sub-problems.

The error in the sensitivity gradient predicted by the adjoint formulations has been assessed in three different ways. First, we defined an error measure $\mathcal{E}$ (2.22) that quantifies the difference between the sensitivity gradient predicted by our adjoint methods and a finite-difference approximation of it. As $\alpha \to 0$, we observed that the gradient error $\mathcal{E} \to \mathcal{O}(\alpha)$ up to round-off errors using the discrete-adjoint method, which is the expected behavior for the exact sensitivity gradient. The actual error is the result of finite computing precision plus a degree of amplification via the nonlinearity in the chaotic flow. However, its sensitivity to arithmetic precision was ascertained in the case of a two-dimensional shear layer, for which case the gradient accuracy was shown to be proportional to the precision of the underlying arithmetic.

Second, we quantified the error of the continuous-adjoint method in a generalized gradient direction φ, which is anticipated to be particularly important for seeking a local optimum. In our compressible turbulent mixing layer demonstration, we showed that φ increases throughout the duration of the control interval for which the adjoint $Q_5^\dagger$ waves interact with the mixing layer, and reaches a maximum value of about $10°$ for the time simulated. This time horizon was practical for our turbulence simulation since it corresponds to the time over which the turbulence could be realistically simulated in the computational box. For longer simulations of other flows, there is every expectation that this error would continue to increase due to the

chaotic character of the flow.

Finally, we considered the spatial scales of the error. The difference between the discrete- and continuous-adjoint formulations is of the order of the truncation error of the numerical approximation, and will therefore for any particular field be larger for shorter and therefore more challenging-to-resolve wavelengths. However, our results for the evolution equations show that the error in the sensitivity gradient becomes large across the entire range of scales. The broad-banded difference is not a direct consequence of nonlinearity, since the adjoint equations are linear, but is a manifestation of the nonlinearity of the flow equations, which appears in the adjoint as space and time dependent coefficients with a similar effect of coupling the adjoint solution across all scales. Further, the difference grows exponentially in reverse-time. Many efforts in optimal flow control have focused on laminar flows or two-dimensional flows, where high accuracy is relatively easy to achieve and the flows are often relatively deterministic because they lack of all the mechanical features of true three-dimensional turbulence. How such errors in a continuous-adjoint formulation contaminate the large-scale components of the gradient is important for two reasons. The first is physical: the large scales are the more likely points of flow control. The second involves modeling and the challenge of developing sub-grid-scale (or other) turbulence models for which practical exact adjoints are available. If errors are incurred, say, by using a hybrid formulation [80], they can be anticipated to contaminate the solution at many scales. This study shows what effects might be anticipated by the inherent approximations.

Our results have implications for some recent flow control simulations. Using a continuous-adjoint formulation, Kim et al. [37] found that even with a general control, the overall noise reduction achieved for a turbulent Mach 1.3 jet was significantly lower than in a previous two-dimensional study [90]. Taking our plane, temporally developing turbulent mixing layer as a model for the initial shear layers of a turbulent jet, we can estimate the deleterious effects of the continuous-adjoint used in that study. We see a significant error for the continuous formulation as the momentum thickness increases from about $19\delta_m^0$ to $53\delta_m^0$, a factor of 2.8, during the control interval. This growth is comparable to the momentum thickness growth of $2.75\times$ along the potential core length of their simulated turbulent jet. This suggests that the instantaneous continuous-adjoint-based sensitivity for a nozzle control will entail a similar $10°$ error by $x/D \sim 6$, which is the region of peak noise generation. Given the reduced effectiveness even in the present simpler flow, we can anticipate that the errors in the gradient might be more significant in the jet.

It should also be noted that convergence was slow and not pursued through to completion by Kim et al. [37]. Significant slowing of convergence, relative to the earlier two-dimensional flows [90], might have also masked the potential success of the control. To assess this, at least indirectly, we have applied a dual-consistent discrete-exact formulation to this flow configuration for demonstration and verification of the

multi-block interface dual-consistency condition derived in Theorem 5.7. The discrete-adjoint is smooth with no apparent artifacts due to discretization near the interfaces between blocks, where it would be expected in a dual-inconsistent formulation. In addition, the gradient error $\mathcal{E}$ defined in (2.22) converges to $\mathcal{O}(\alpha)$ upto an apparent roundoff limit. The norm of adjoint quantities grow exponentially in reverse time, which has been previously observed for a chaotic Lorenz system [44], and indicates the sensitivity to initial condition of turbulence. We have not quantified the rate of this exponential growth, though it appears to be related to the first Lyapunov exponent as shown for the drag-adjoint field of a circular cylinder wake by Wang and Gao [87]. The discrete-adjoint-based gradient leads to an 8% reduction in the cost functional based on (2.14) and (2.15), but it is unclear whether the mechanism for control suggested by our numerical simulation can be applied to design realistic actuators, and if so whether they would lead to similar reductions.

An important result here is that the discrete-adjoint formulation was found to be sufficiently accurate (e.g., Figure 7.17) for the control horizons needed for our aeroacoustic objectives. However, for longer times the fidelity would eventually succumb to the accumulation of round-off errors, amplified by the chaotic character of the turbulence. The amplification of the difference between the discrete- and continuous-adjoints in Figures 7.19b and 7.20b shows how this will occur. These round-off errors are complicated functions of the coefficients of our finite-difference schemes and the adjoint coefficient matrix, and are neither uncorrelated, nor uniformly distributed on either side of zero on the real line. However, they are roughly proportional to the number of floating point operations and will undoubtedly accumulate to the point of overwhelming the exactness of the discrete formulation for sufficiently long times. Estimating or designing numerical methods to reduce or eliminate such round-off errors is beyond the scope of this work.

Appendix A

Linearization of the Compressible Flow Equations

Recall the compressible flow equations (2.6):

$$\frac{\partial Q}{\partial t} + J \frac{\partial}{\partial \xi_i} \left[\mathrm{M}_{ij} \left(F_j^I - F_j^V \right) \right] = 0, \ \boldsymbol{\xi} \in \mathbb{D}, \ t_0 \leq t \leq t_1,$$

and the corresponding operator (2.11):

$$\mathcal{R}\left[Q\right] = -J \frac{\partial}{\partial \xi_i} \left[\mathrm{M}_{ij} \left(\mathcal{F}_j^I\left[Q\right] - \mathcal{F}_j^V\left[Q\right] \right) \right].$$

Here, we will derive the Fréchet derivative of $\mathcal{R}\left[Q\right]$ as defined in (2.12). The result is derived for a three-dimensional problem, with straightforward extension to one and two dimensions. We assume the constitutive relations (2.8) for the fluid, and a power law dependence of the coefficients of viscosity on the temperature as per (2.9).

First, we express the inviscid fluxes defined in (2.7) as

$$\mathcal{F}_i^I\left[Q\right] = \rho u_i \begin{bmatrix} 1 \\ u_1 \\ u_2 \\ u_3 \\ h \end{bmatrix} + \left(\rho h - \rho E\right) \begin{bmatrix} 0 \\ \delta_{i1} \\ \delta_{i2} \\ \delta_{i3} \\ 0 \end{bmatrix},$$

where $h = \frac{\rho E + p}{\rho}$ is the enthalpy. To derive the Fréchet derivative of $\mathcal{F}_i^I\left[Q\right]$, we will employ the following expressions for the linearization of the velocity and enthalpy with respect to the state variable:

$$\delta u_i = \frac{1}{\rho} \begin{bmatrix} -u_i & \delta_{i1} & \delta_{i2} & \delta_{i3} & 0 \end{bmatrix} \delta Q$$

$$\delta h = \frac{1}{\rho} \begin{bmatrix} \phi^2 - h & (\gamma - 1) u_1 \delta_{i1} & (\gamma - 1) u_2 \delta_{i2} & (\gamma - 1) u_3 \delta_{i3} & \gamma \end{bmatrix} \delta Q,$$

102

where $\phi^2 = \frac{\gamma-1}{2} u_i u_i$. Retaining only terms up to $\mathcal{O}\left(\|\delta Q\|\right)$, we obtain the result

$$\delta \mathcal{F}_i^I \left[Q; \delta Q\right] = \widehat{\mathcal{A}}_i^I \left[Q\right] \delta Q, \tag{A.1}$$

where

$$\widehat{\mathcal{A}}_i^I \left[Q\right] = \begin{bmatrix} 0 & \delta_{i1} & \delta_{i2} \\ \phi^2 \delta_{i1} - u_1 u_i & u_i - (\gamma - 2) u_1 \delta_{i1} & u_1 \delta_{i2} - (\gamma - 1) u_2 \delta_{i1} \\ \phi^2 \delta_{i2} - u_2 u_i & u_2 \delta_{i1} - (\gamma - 1) u_1 \delta_{i2} & u_i - (\gamma - 2) u_2 \delta_{i2} \\ \phi^2 \delta_{i3} - u_3 u_i & u_3 \delta_{i1} - (\gamma - 1) u_1 \delta_{i3} & u_3 \delta_{i2} - (\gamma - 1) u_2 \delta_{i3} \\ u_i \left(\phi^2 - h\right) & h \delta_{i1} - (\gamma - 1) u_1 u_i & h \delta_{i2} - (\gamma - 1) u_2 u_i \end{bmatrix}$$

$$\begin{bmatrix} \delta_{i3} & 0 \\ u_1 \delta_{i3} - (\gamma - 1) u_3 \delta_{i1} & (\gamma - 1) \delta_{i1} \\ u_2 \delta_{i3} - (\gamma - 1) u_3 \delta_{i2} & (\gamma - 1) \delta_{i2} \\ u_i - (\gamma - 2) u_3 \delta_{i3} & (\gamma - 1) \delta_{i3} \\ h \delta_{i3} - (\gamma - 1) u_3 u_i & \gamma u_i \end{bmatrix}$$

is the Jacobian of the inviscid fluxes with respect to the state variable.

To linearize $\mathcal{F}_i^V \left[Q\right]$, we first consider the primitive variables

$$Q_p = \begin{bmatrix} \rho & u_1 & u_2 & u_3 & T \end{bmatrix}^{\mathrm{T}}.$$

The Jacobian of the primitive variables with respect to the conservative variables is defined as

$$\mathcal{C}\left[Q\right] \equiv \frac{\partial Q_p}{\partial Q},$$

and will be expanded shortly. The viscous fluxes defined in (2.7) can be written as

$$\mathcal{F}_i^V \left[Q_p\right] = \frac{J\mathrm{M}_{jk}}{\mathrm{Re}} \left\{ \mu \begin{bmatrix} 0 \\ \delta_{ki} \frac{\partial u_1}{\partial \xi_j} + \delta_{k1} \frac{\partial u_i}{\partial \xi_j} \\ \delta_{ki} \frac{\partial u_2}{\partial \xi_j} + \delta_{k2} \frac{\partial u_i}{\partial \xi_j} \\ \delta_{ki} \frac{\partial u_3}{\partial \xi_j} + \delta_{k3} \frac{\partial u_i}{\partial \xi_j} \\ u_l \left(\delta_{ki} \frac{\partial u_l}{\partial \xi_j} + \delta_{kl} \frac{\partial u_i}{\partial \xi_j} \right) + \frac{1}{\mathrm{Pr}} \delta_{ki} \frac{\partial T}{\partial \xi_j} \end{bmatrix} + \lambda \frac{\partial u_k}{\partial \xi_j} \begin{bmatrix} 0 \\ \delta_{1i} \\ \delta_{2i} \\ \delta_{3i} \\ u_i \end{bmatrix} \right\}.$$

Our strategy will be to derive the Fréchet derivative of $\mathcal{F}_i^V \left[Q_p\right]$ with respect to the primitive variables

and use the chain rule of Gâteaux differentiation for functionals: $\delta\mathcal{F}_i^V[Q;\delta Q] = \delta\mathcal{F}_i^V[Q_p;\mathcal{C}[Q]\,\delta Q]$. The coefficients of viscosity are temperature-dependent, and can be linearized as

$$\delta\mu = \frac{n\mu}{T}\delta T, \quad \delta\lambda = \frac{n\lambda}{T}\delta T,$$

respectively. In deriving the Fréchet derivative of $\mathcal{F}_i^V[Q_p]$, we will deliberately refrain from combining terms using the product rule of differentiation for partial derivatives in ξ_1, ξ_2, and ξ_3. This allows us to re-use the result with discrete derivative operators, which are not guaranteed to mimic the product rule (locally). After some algebra, we obtain

$$\delta\mathcal{F}_i^V[Q_p;\delta Q_p] = \begin{bmatrix} 0 & 0 & 0 & 0 & 0 \\ 0 & 0 & 0 & 0 & \frac{n\tau_{1i}}{T} \\ 0 & 0 & 0 & 0 & \frac{n\tau_{2i}}{T} \\ 0 & 0 & 0 & 0 & \frac{n\tau_{3i}}{T} \\ 0 & \tau_{1i} & \tau_{2i} & \tau_{3i} & \frac{1}{T}\left(u_j\tau_{ji} - q_i\right) \end{bmatrix} \delta Q_p + \widehat{\mathcal{B}}_{ij}[Q_p]\frac{\partial}{\partial\xi_j}(\delta Q_p), \tag{A.2}$$

where

$$\widehat{\mathcal{B}}_{ij}[Q_p] = \frac{J\mathrm{M}_{jk}}{\mathrm{Re}}\begin{bmatrix} 0 & 0 & 0 \\ 0 & \mu\delta_{ki}+(\mu+\lambda)\,\delta_{k1}\delta_{i1} & \mu\delta_{k1}\delta_{i2}+\lambda\delta_{k2}\delta_{i1} \\ 0 & \mu\delta_{k2}\delta_{i1}+\lambda\delta_{k1}\delta_{i2} & \mu\delta_{ki}+(\mu+\lambda)\,\delta_{k2}\delta_{i2} \\ 0 & \mu\delta_{k3}\delta_{i1}+\lambda\delta_{k1}\delta_{i3} & \mu\delta_{k3}\delta_{i2}+\lambda\delta_{k2}\delta_{i3} \\ 0 & \mu u_1\delta_{ki}+\mu u_k\delta_{i1}+\lambda u_i\delta_{k1} & \mu u_2\delta_{ki}+\mu u_k\delta_{i2}+\lambda u_i\delta_{k2} \end{bmatrix}$$

$$\begin{bmatrix} 0 & 0 \\ \mu\delta_{k1}\delta_{i3}+\lambda\delta_{k3}\delta_{i1} & 0 \\ \mu\delta_{k2}\delta_{i3}+\lambda\delta_{k3}\delta_{i2} & 0 \\ \mu\delta_{ki}+(\mu+\lambda)\,\delta_{k2}\delta_{i2} & 0 \\ \mu u_3\delta_{ki}+\mu u_k\delta_{i3}+\lambda u_i\delta_{k3} & \frac{\mu}{\mathrm{Pr}}\delta_{ki} \end{bmatrix}.$$

Using A.1 and A.2, we can now write the Fréchet derivative of $\mathcal{R}[Q]$ as

$$\delta\mathcal{R}[Q;\delta Q] = -J\frac{\partial}{\partial\xi_i}\left\{\left(\mathcal{A}_i^I[Q]-\mathcal{A}_i^V[Q]\right)\delta Q - \mathcal{B}_{ij}[Q]\frac{\partial}{\partial\xi_j}\left(\mathcal{C}[Q]\,\delta Q\right)\right\}, \tag{A.3}$$

104

where

$$
\mathcal{A}_i^I\left[Q\right] =
\begin{bmatrix}
0 & \mathrm{M}_{i1} & \mathrm{M}_{i2} \\[4pt]
\phi^2 \mathrm{M}_{i1} - u_1 \hat{u}_i & \hat{u}_i - (\gamma-2)\, u_1 \mathrm{M}_{i1} & u_1 \mathrm{M}_{i2} - (\gamma-1)\, u_2 \mathrm{M}_{i1} \\[4pt]
\phi^2 \mathrm{M}_{i2} - u_2 \hat{u}_i & u_2 \mathrm{M}_{i1} - (\gamma-1)\, u_1 \mathrm{M}_{i2} & \hat{u}_i - (\gamma-2)\, u_2 \mathrm{M}_{i2} \\[4pt]
\phi^2 \mathrm{M}_{i3} - u_3 \hat{u}_i & u_3 \mathrm{M}_{i1} - (\gamma-1)\, u_1 \mathrm{M}_{i3} & u_3 \mathrm{M}_{i2} - (\gamma-1)\, u_2 \mathrm{M}_{i3} \\[4pt]
\hat{u}_i\left(\phi^2 - h\right) & h \mathrm{M}_{i1} - (\gamma-1)\, u_1 \hat{u}_i & h \mathrm{M}_{i2} - (\gamma-1)\, u_2 \hat{u}_i
\end{bmatrix}
$$

$$
\begin{bmatrix}
\mathrm{M}_{i3} & 0 \\[4pt]
u_1 \mathrm{M}_{i3} - (\gamma-1)\, u_3 \mathrm{M}_{i1} & (\gamma-1)\, \mathrm{M}_{i1} \\[4pt]
u_2 \mathrm{M}_{i3} - (\gamma-1)\, u_3 \mathrm{M}_{i2} & (\gamma-1)\, \mathrm{M}_{i2} \\[4pt]
\hat{u}_i - (\gamma-2)\, u_3 \mathrm{M}_{i3} & (\gamma-1)\, \mathrm{M}_{i3} \\[4pt]
h \mathrm{M}_{i3} - (\gamma-1)\, u_3 \hat{u}_i & \gamma \hat{u}_i
\end{bmatrix} , \tag{A.4a}
$$

$$
\mathcal{A}_i^V\left[Q\right] = \frac{1}{\rho}
\begin{bmatrix}
0 & 0 \\[4pt]
\frac{n\gamma}{T}\left(\frac{\phi^2}{\gamma-1} - \frac{T}{\gamma}\right)\hat{\tau}_{i1} & -\frac{n\gamma}{T} u_1 \hat{\tau}_{i1} \\[6pt]
\frac{n\gamma}{T}\left(\frac{\phi^2}{\gamma-1} - \frac{T}{\gamma}\right)\hat{\tau}_{i2} & -\frac{n\gamma}{T} u_1 \hat{\tau}_{i2} \\[6pt]
\frac{n\gamma}{T}\left(\frac{\phi^2}{\gamma-1} - \frac{T}{\gamma}\right)\hat{\tau}_{i3} & -\frac{n\gamma}{T} u_1 \hat{\tau}_{i3} \\[6pt]
\frac{n\gamma}{T}\left(\frac{\phi^2}{\gamma-1} - \frac{T}{\gamma}\right)\left(u_k \hat{\tau}_{ik} - \hat{q}_i\right) - u_k \hat{\tau}_{ik} & \hat{\tau}_{i1} - \frac{n\gamma}{T} u_1\left(u_k \hat{\tau}_{ik} - \hat{q}_i\right)
\end{bmatrix}
$$

$$
\begin{bmatrix}
0 & 0 & 0 \\[4pt]
-\frac{n\gamma}{T} u_2 \hat{\tau}_{i1} & -\frac{n\gamma}{T} u_3 \hat{\tau}_{i1} & \frac{n\gamma}{T} \hat{\tau}_{i1} \\[6pt]
-\frac{n\gamma}{T} u_2 \hat{\tau}_{i2} & -\frac{n\gamma}{T} u_3 \hat{\tau}_{i2} & \frac{n\gamma}{T} \hat{\tau}_{i2} \\[6pt]
-\frac{n\gamma}{T} u_2 \hat{\tau}_{i3} & -\frac{n\gamma}{T} u_3 \hat{\tau}_{i3} & \frac{n\gamma}{T} \hat{\tau}_{i3} \\[6pt]
\hat{\tau}_{i2} - \frac{n\gamma}{T} u_2\left(u_k \hat{\tau}_{ik} - \hat{q}_i\right) & \hat{\tau}_{i3} - \frac{n\gamma}{T} u_3\left(u_k \hat{\tau}_{ik} - \hat{q}_i\right) & \frac{n\gamma}{T}\left(u_k \hat{\tau}_{ik} - \hat{q}_i\right)
\end{bmatrix} , \tag{A.4b}
$$

$$
\mathcal{B}_{ij}\left[Q\right] = \frac{J}{\mathrm{Re}}
\begin{bmatrix}
0 & 0 & 0 \\[4pt]
0 & \mu \mathrm{M}_{ik}\mathrm{M}_{jk} + (\mu+\lambda)\,\mathrm{M}_{i1}\mathrm{M}_{j1} & \mu \mathrm{M}_{i2}\mathrm{M}_{j1} + \lambda \mathrm{M}_{i1}\mathrm{M}_{j2} \\[4pt]
0 & \mu \mathrm{M}_{i1}\mathrm{M}_{j2} + \lambda \mathrm{M}_{i2}\mathrm{M}_{j1} & \mu \mathrm{M}_{ik}\mathrm{M}_{jk} + (\mu+\lambda)\,\mathrm{M}_{i2}\mathrm{M}_{j2} \\[4pt]
0 & \mu \mathrm{M}_{i1}\mathrm{M}_{j3} + \lambda \mathrm{M}_{i3}\mathrm{M}_{j1} & \mu \mathrm{M}_{i2}\mathrm{M}_{j3} + \lambda \mathrm{M}_{i3}\mathrm{M}_{j2} \\[4pt]
0 & \mu u_1 \mathrm{M}_{ik}\mathrm{M}_{jk} + \mu \hat{u}_j \mathrm{M}_{i1} + \lambda \hat{u}_i \mathrm{M}_{j1} & \mu u_2 \mathrm{M}_{ik}\mathrm{M}_{jk} + \mu \hat{u}_j \mathrm{M}_{i2} + \lambda \hat{u}_i \mathrm{M}_{j2}
\end{bmatrix}
$$

105

$$
\left.
\begin{array}{cc}
0 & 0 \\
\mu M_{i3} M_{j1} + \lambda M_{i1} M_{j3} & 0 \\
\mu M_{i3} M_{j2} + \lambda M_{i2} M_{j3} & 0 \\
\mu M_{ik} M_{jk} + (\mu + \lambda) M_{i3} M_{j3} & 0 \\
\mu u_3 M_{ik} M_{jk} + \mu \hat{u}_j M_{i3} + \lambda \hat{u}_i M_{j3} & \frac{1}{\Pr} \mu M_{ik} M_{jk}
\end{array}
\right], \tag{A.4c}
$$

$$
\mathcal{C}[Q] = \frac{1}{\rho}
\begin{bmatrix}
\rho & 0 & 0 & 0 & 0 \\
-u_1 & 1 & 0 & 0 & 0 \\
-u_2 & 0 & 1 & 0 & 0 \\
-u_3 & 0 & 0 & 1 & 0 \\
\frac{\gamma \phi^2}{\gamma-1} - T & -\gamma u_1 & -\gamma u_2 & -\gamma u_3 & \gamma
\end{bmatrix}, \tag{A.4d}
$$

where $\hat{u}_i = M_{ij} u_j$ are the components of the contravariant velocity, $\hat{q}_i = M_{ij} q_j$, and $\hat{\tau}_{ij} = M_{ik} \tau_{kj}$. The operators $\mathcal{A}_i^I[Q]$ and $\mathcal{B}_{ij}[Q]$ are related to $\widehat{\mathcal{A}}_i^I[Q]$ and $\widehat{\mathcal{B}}_{ij}[Q]$ as $\mathcal{A}_i^I[Q] = M_{ij} \widehat{\mathcal{A}}_j^I[Q]$, and $\mathcal{B}_{ij}[Q] = M_{ik} \widehat{\mathcal{B}}_{kj}^I[Q]$, respectively.

Bibliography

[1] IEEE Standard for Floating-Point Arithmetic. *IEEE Std 754-2008*, pages 1–70, 2008. doi:`10.1109/IEEESTD.2008.4610935`.

[2] W. K. Anderson and V. Venkatakrishnan. Aerodynamic design optimization on unstructured grids with a continuous adjoint formulation. *Computers & Fluids*, 28:443–480, 1999. doi:`10.1016/S0045-7930(98)00041-3`.

[3] R. Becker and R. Rannacher. A feed-back approach to error control in finite element methods: Basic analysis and examples. *East–West Journal of Numerical Mathematics*, 4:237–264, 1996.

[4] J. H. Bell and R. D. Mehta. Development of a two-stream mixing layer from tripped and untripped boundary layers. *AIAA Journal*, 28:2034–2042, 1990. doi:`10.2514/3.10519`.

[5] J. Benek, P. G. Buning, and J. L. Steger. A 3-D chimera grid embedding technique. In *7th AIAA Computational Physics Conference*, 1985. doi:`10.2514/6.1985-1523`.

[6] T. R. Bewley, P. Moin, and R. Temam. DNS-based predictive control of turbulence: an optimal benchmark for feedback algorithms. *Journal of Fluid Mechanics*, 447:179–225, 2001. doi:`10.1017/S0022112001005821`.

[7] D. J. Bodony and S. K. Lele. On using large-eddy simulation for the prediction of noise from cold and heated turbulent jets. *Physics of Fluids*, 17:085103, 2005. doi:`10.1063/1.2001689`.

[8] D. J. Bodony, G. Zagaris, A. Reichert, and Q. Zhang. Provably stable overset grid methods for computational aeroacoustics. *Journal of Sound and Vibration*, 330:4161–4179, 2011. doi:`10.1016/j.jsv.2011.02.010`.

[9] C. Bogey and C. Bailly. A family of low dispersive and low dissipative explicit schemes for flow and noise computations. *Journal of Computational Physics*, 194:194–214, 2004. doi:`10.1016/j.jcp.2003.09.003`.

[10] C. Bogey and C. Bailly. Computation of a high reynolds number jet and its radiated noise using large eddy simulation based on explicit filtering. *Computers & Fluids*, 35:1344–1358, 2006. doi:`10.1016/j.compfluid.2005.04.008`.

[11] C. Bogey and C. Bailly. Large eddy simulations of round free jets using explicit filtering with/without dynamic smagorinsky model. *International Journal of Heat and Fluid Flow*, 27:603–610, 2006. doi:`10.1016/j.ijheatfluidflow.2006.02.008`.

[12] J. Bridges and M. P. Wernet. Turbulence associated with broadband shock noise in hot jets. In *14th AIAA/CEAS Aeroacoustics Conference (29th AIAA Aeroacoustics Conference)*, 2008. doi:`10.2514/6.2008-2834`.

[13] A. Carnarius, F. Thiele, E. Özkaya, and N. R. Gauger. Adjoint approaches for optimal flow control. In *5th Flow Control Conference*, 2010. doi:`10.2514/6.2010-5088`.

[14] T. Colonius. Modeling artificial boundary conditions for compressible flow. *Annual Review of Fluid Mechanics*, 36:315–345, 2004. doi:10.1146/annurev.fluid.36.050802.121930.

[15] T. Colonius and S. K. Lele. Computational aeroacoustics: progress on nonlinear problems of sound generation. *Progress in Aerospace Sciences*, 40:345–416, 2004. doi:10.1016/j.paerosci.2004.09.001.

[16] S. C. Crow and F. H. Champagne. Orderly structure in jet turbulence. *Journal of Fluid Mechanics*, 48: 547–591, 1971. doi:10.1017/S0022112071001745.

[17] M. F. de Pando, D. Sipp, and P. J. Schmid. Efficient evaluation of the direct and adjoint linearized dynamics from compressible flow solvers. *Journal of Computational Physics*, 231:7739–7755, 2012. doi:10.1016/j.jcp.2012.06.038.

[18] M. F. de Pando, P. J. Schmid, and D. Sipp. A global analysis of tonal noise in flows around aerofoils. *Journal of Fluid Mechanics*, 754:5–38, 2014. doi:10.1017/jfm.2014.356.

[19] P. Diener, E. N. Dorband, E. Schnetter, and M. Tiglio. Optimized high-order derivative and dissipation operators satisfying summation by parts, and applications in three-dimensional multi-block evolutions. *Journal of Scientific Computing*, 32:109–145, 2007. doi:10.1007/s10915-006-9123-7.

[20] K. Duraisamy and J. Alonso. Adjoint based techniques for uncertainty quantification in turbulent flows with combustion. In *42nd AIAA Fluid Dynamics Conference and Exhibit*, 2012. doi:10.2514/6.2012-2711.

[21] T. C. Fisher, M. H. Carpenter, J. Nordström, N. K. Yamaleev, and C. Swanson. Discretely conservative finite-difference formulations for nonlinear conservation laws in split form: Theory and boundary conditions. *Journal of Computational Physics*, 234:353–375, 2013. doi:10.1016/j.jcp.2012.09.026.

[22] J. B. Freund. Proposed inflow/outflow boundary condition for direct computation of aerodynamic sound. *AIAA Journal*, 35:740–742, 1997. doi:10.2514/2.167.

[23] J. B. Freund. Adjoint-based optimization for understanding and suppressing jet noise. *Journal of Sound and Vibration*, 330:4114–4122, 2011. doi:10.1016/j.jsv.2011.02.009.

[24] J. B. Freund, S. K. Lele, and P. Moin. Numerical simulation of a Mach 1.92 turbulent jet and its sound field. *AIAA Journal*, 38:2023–2031, 2000. doi:10.2514/2.889.

[25] M. B. Giles, M. C. Duta, J.-D. Müller, and N. A. Pierce. Algorithm developments for discrete adjoint methods. *AIAA Journal*, 41:198–205, 2003. doi:10.2514/2.1961.

[26] A. Griewank and G. F. Corliss, editors. *Automatic Differentiation of Algorithms: Theory, Implementation and Application*. SIAM Proceedings Series, Society for Industrial and Applied Mathematics, 1991.

[27] K. Harriman, D. Gavaghan, and E. Süli. The importance of adjoint consistency in the approximation of linear functionals using the discontinuous Galerkin finite element method. Technical report, Oxford University Computing Laboratory, 2004.

[28] E. R. Hawkes, R. Sankaran, J. C. Sutherland, and J. H. Chen. Direct numerical simulation of turbulent combustion: fundamental insights towards predictive models. *Journal of Physics: Conference Series*, 16:65–79, 2005. doi:10.1088/1742-6596/16/1/009.

[29] J. E. Hicken and D. W. Zingg. Superconvergent functional estimates from summation-by-parts finite-difference discretizations. *SIAM Journal on Scientific Computing*, 33:893–922, 2011. doi:10.1137/100790987.

[30] J. E. Hicken and D. W. Zingg. Summation-by-parts operators and high-order quadrature. *Journal of Computational and Applied Mathematics*, 237:111–125, 2013. doi:10.1016/j.cam.2012.07.015.

[31] J. E. Hicken and D. W. Zingg. Dual consistency and functional accuracy: a finite-difference perspective. *Journal of Computational Physics*, 256:161–182, 2014. doi:`10.1016/j.jcp.2013.08.014`.

[32] D. C. Hill. Adjoint systems and their role in the receptivity problem for boundary layers. *Journal of Fluid Mechanics*, 292:183–204, 1995. doi:`10.1017/S0022112095001480`.

[33] A. Jameson, L. Martinelli, and N. A. Pierce. Optimum aerodynamic design using the Navier–Stokes equations. *Theoretical and Computational Fluid Dynamics*, 10:213–237, 1998. doi:`10.1007/s001620050060`.

[34] S. Johansson. High order finite difference operators with the summation by parts property based on DRP schemes. Technical report, Uppsala University, 2004.

[35] J. Katz and B. Maskew. Unsteady low-speed aerodynamic model for complete aircraft configurations. *Journal of Aircraft*, 24:302–310, 1988. doi:`10.2514/3.45564`.

[36] J. Kim. *Adjoint-based control of turbulent jet noise*. PhD thesis, University of Illinois at Urbana–Champaign, 2012.

[37] J. Kim, D. J. Bodony, and J. B. Freund. Adjoint-based control of loud events in a turbulent jet. *Journal of Fluid Mechanics*, 741:28–59, 2014. doi:`10.1017/jfm.2013.654`.

[38] R. R. Kleinman. *On the turbulence-generated sound and control of compressible mixing layers*. PhD thesis, University of Illinois at Urbana–Champaign, 2010.

[39] R. R. Kleinman and J. B. Freund. The sound from mixing layers simulated with different ranges of turbulence scales. *Physics of Fluids*, 20:101503, 2008. doi:`10.1063/1.3005823`.

[40] H.-O. Kreiss. Initial boundary value problems for hyperbolic systems. *Communications on Pure and Applied Mathematics*, 23:277–298, 1970. doi:`10.1002/cpa.3160230304`.

[41] H.-O. Kreiss and G. Scherer. Finite element and finite difference methods for hyperbolic partial differential equations. In *Mathematical Aspects of Finite Elements in Partial Differential Equations*, pages 195–212. Academic Press, 1974. doi:`10.1016/B978-0-12-208350-1.50012-1`.

[42] C. L. Ladson, A. S. Hill, and Jr. W. G. Johnson. Pressure distributions from high reynolds number transonic tests of an NACA 0012 airfoil in the Langley 0.3-meter transonic cryogenic tunnel. Technical report, National Aeronautics and Space Administration, 1987.

[43] C. Lanczos. *Linear differential operators*. D. Van Nostrand Company, Limited, 1961. doi:`10.1137/1.9781611971187`.

[44] D. J. Lea, M. R. Allen, and T. W. N. Haine. Sensitivity analysis of the climate of a chaotic system. *Tellus A*, 52:523–532, 2000. doi:`10.1034/j.1600-0870.2000.01137.x`.

[45] S. K. Lele. Compact finite difference schemes with spectral-like resolution. *Journal of Computational Physics*, 103:16–42, 1992. doi:`10.1016/0021-9991(92)90324-R`.

[46] S. K. Lele. Compressibility effects on turbulence. *Annual Review of Fluid Mechanics*, 26:211–254, 1994. doi:`10.1146/annurev.fl.26.010194.001235`.

[47] R. Li, A. C. Reynolds, and D. S. Oliver. History matching of three-phase flow production data. *SPE Journal*, 8:SPE–87336–PA, 2003. doi:`10.2118/87336-PA`.

[48] B. Lockwood and D. Mavriplis. Gradient-based methods for uncertainty quantification in hypersonic flows. *Computers & Fluids*, 85:27–38, 2013. doi:`10.1016/j.compfluid.2012.09.003`.

[49] P. Luchini and A. Bottaro. Adjoint equations in stability analysis. *Annual Review of Fluid Mechanics*, 46:493–517, 2014. doi:`10.1146/annurev-fluid-010313-141253`.

[50] C. A. Mader, J. R. R. A. Martins, J. J. Alonso, and E. van der Weide. ADjoint: An approach for the rapid development of discrete adjoint solvers. *AIAA Journal*, 46:863–873, 2008. doi:`10.2514/1.29123`.

[51] J. R. R. A. Martins, J. J. Alonso, and J. J. Reuther. High-fidelity aerostructural design optimization of a supersonic business jet. *Journal of Aircraft*, 41:523–530, 2004. doi:`10.2514/1.11478`.

[52] K. Mattsson. Summation by parts operators for finite difference approximations of second-derivatives with variable coefficients. *Journal of Scientific Computing*, 51:650–682, 2012. doi:`10.1007/s10915-011-9525-z`.

[53] K. Mattsson and J. Nordström. Summation by parts operators for finite difference approximations of second derivatives. *Journal of Computational Physics*, 199:503–540, 2004. doi:`10.1016/j.jcp.2004.03.001`.

[54] K. Mattsson, M. Svärd, and J. Nordström. Stable and accurate artificial dissipation. *Journal of Scientific Computing*, 21:57–79, 2004. doi:`10.1023/B:JOMP.0000027955.75872.3f`.

[55] S. Mendez, M. Shoeybi, A. Sharma, F. E. Ham, S. K. Lele, and P. Moin. Large-eddy simulations of perfectly-expanded supersonic jets: Quality assessment and validation. In *48th AIAA Aerospace Sciences Meeting Including the New Horizons Forum and Aerospace Exposition*, 2010. doi:`10.2514/6.2010-271`.

[56] S. Nadarajah and A. Jameson. Studies of the continuous and discrete adjoint approaches to viscous automatic aerodynamic shape optimization. In *15th AIAA Computational Fluid Dynamics Conference*, 2001. doi:`10.2514/6.2001-2530`.

[57] M. Nemec and M. J. Aftosmis. Adjoint error estimation and adaptive refinement for embedded-boundary Cartesian meshes. In *18th AIAA Computational Fluid Dynamics Conference*, 2007. doi:`10.2514/6.2007-4187`.

[58] E. J. Nielsen and B. Diskin. Discrete adjoint-based design for unsteady turbulent flows on dynamic overset unstructured grids. *AIAA Journal*, 51:1355–1373, 2013. doi:`10.2514/1.J051859`.

[59] J. Nordström and T. Lundquist. Summation-by-parts in time. *Journal of Computational Physics*, 251:487–499, 2013. doi:`10.1016/j.jcp.2013.05.042`.

[60] J. Nordström, J. Gong, E. van der Weide, and M. Svärd. A stable and conservative high order multi-block method for the compressible navier-stokes equations. *Journal of Computational Physics*, 228:9020–9035, 2009. doi:`10.1016/j.jcp.2009.09.005`.

[61] P. Olsson. Summation by parts, projections and stability. i. *Mathematics of Computation*, 64:1035–1065, 1995.

[62] C. Pantano and S. Sarkar. A study of compressibility effects in the high-speed turbulent shear layer using direct simulation. *Journal of Fluid Mechanics*, 451:329–371, 2002. doi:`10.1017/S0022112001006978`.

[63] T. J. Poinsot and S. K. Lele. Boundary conditions for direct simulations of compressible viscous flows. *Journal of Computational Physics*, 101:104–129, 1992. doi:`10.1016/0021-9991(92)90046-2`.

[64] W. H. Press, S. A. Teukolsky, W. T. Vetterling, and B. P. Flannery. *Numerical Recipes: The Art of Scientific Computing*. Cambridge University Press, 2007.

[65] T. H. Pulliam and D. S. Chaussee. A diagonal form of an implicit approximate-factorization algorithm. *Journal of Computational Physics*, 39:347–363, 1981. doi:`10.1016/0021-9991(81)90156-X`.

[66] P. L. Roe and J. Pike. Efficient construction and utilisation of approximate Riemann solutions. In *6th International Symposium on Computing Methods in Applied Sciences and Engineering*, 1984.

[67] R. Roth and S. Ulbrich. A discrete adjoint approach for the optimization of unsteady turbulent flows. *Flow, Turbulence and Combustion*, 90:763–783, 2013. doi:`10.1007/s10494-012-9439-3`.

[68] M. Rumpfkeil and D. Zingg. Unsteady optimization using a discrete adjoint approach applied to aeroacoustic shape design. In *45th AIAA Aerospace Sciences Meeting and Exhibit*, 2007. doi: 10.2514/6.2007-1128.

[69] M. Samimy, I. Adamovich, B. Webb, J. Kastner, J. Hileman, S. Keshav, and P. Palm. Development and characterization of plasma actuators for high-speed jet control. *Experiments in Fluids*, 37:577–588, 2004. doi:10.1007/s00348-004-0854-7.

[70] M. Samimy, J.-H. Kim, J. Kastner, I. Adamovich, and Y. Utkin. Active control of high-speed and high-Reynolds-number jets using plasma actuators. *Journal of Fluid Mechanics*, 578:305–330, 2007. doi:10.1017/S0022112007004867.

[71] N. L. Sankar, J. B. Malone, and Y. Tassa. An implicit conservative algorithm for steady and unsteady three-dimensional transonic potential flows. In *5th AIAA Computational Fluid Dynamics Conference*, 1981. doi:10.2514/6.1981-1016.

[72] Z. Sirkes and E. Tziperman. Finite difference of adjoint or adjoint of finite difference? *Monthly Weather Review*, 125:3373–3378, 1997. doi:10.1175/1520-0493(1997)125<3373:FDOAOA>2.0.CO;2.

[73] B. W. Spencer and B. G. Jones. Statistical investigation of pressure and velocity fields in the turbulent two-stream mixing layer. In *4th AIAA Fluid and Plasma Dynamics Conference*, 1971. doi:10.2514/6.1971-613.

[74] J. P. Steinbrenner, J. R. Chawner, and C. L. Fouts. The GRIDGEN 3D multiple block grid generation system. Technical Report WRDC-TR-90-3022, Wright Research and Development Center, October 1989.

[75] B. Strand. Summation by parts for finite difference approximations for d/dx. *Journal of Computational Physics*, 110:47–67, 1994. doi:10.1006/jcph.1994.1005.

[76] B. Strand. *High-Order Difference Approximations for Hyperbolic Initial Boundary Value Problems*. PhD thesis, Uppsala University, 1996.

[77] M. Svärd. On coordinate transformation for summation-by-parts operators. *Journal of Scientific Computing*, 20:29–42, 2004. doi:10.1023/A:1025881528802.

[78] M. Svärd and J. Nordström. A stable high-order finite difference scheme for the compressible Navier–Stokes equations: no-slip wall boundary conditions. *Journal of Computational Physics*, 227:4805–4824, 2008.

[79] M. Svärd, M. H. Carpenter, and J. Nordström. A stable high-order finite difference scheme for the compressible Navier–Stokes equations, far-field boundary conditions. *Journal of Computational Physics*, 225:1020–1038, 2007. doi:10.1016/j.jcp.2007.01.023.

[80] T. W. R. Taylor, F. Palacios, K. Duraisamy, and J. J. Alonso. A hybrid adjoint approach applied to turbulent flow simulations. In *21st AIAA Computational Fluid Dynamics Conference*, 2013. doi: 10.2514/6.2013-2452.

[81] P. D. Thomas and C. K. Lombard. Geometric conservation law and its application to flow computations on moving grids. *AIAA Journal*, 17:1030–1037, 1979. doi:10.2514/3.61273.

[82] C. F. van Loan. The ubiquitous kronecker product. *Journal of Computational and Applied Mathematics*, 123:85–100, 2000. doi:10.1016/S0377-0427(00)00393-9.

[83] R. Vishnampet, D. J. Bodony, and J. B. Freund. A practical discrete-adjoint method for high-fidelity compressible turbulence simulations. *Journal of Computational Physics*, 2015.

[84] L. Wang, D. Mavriplis, and K. Anderson. Unsteady discrete adjoint formulation for high-order discontinuous Galerkin discretizations in time-dependent flow problems. In *48th AIAA Aerospace Sciences Meeting Including the New Horizons Forum and Aerospace Exposition*, 2010. doi:10.2514/6.2010-367.

[85] M. Wang, J. B. Freund, and S. K. Lele. Computational prediction of flow-generated sound. *Annual Review of Fluid Mechanics*, 38:483–512, 2006. doi:`10.1146/annurev.fluid.38.050304.092036`.

[86] Q. Wang. Forward and adjoint sensitivity computation of chaotic dynamical systems. *Journal of Computational Physics*, 235:1–13, 2013. doi:`10.1016/j.jcp.2012.09.007`.

[87] Q. Wang and J.-H. Gao. The drag-adjoint field of a circular cylinder wake at reynolds numbers 20, 100 and 500. *Journal of Fluid Mechanics*, 730:145–161, 2013. doi:`10.1017/jfm.2013.323`.

[88] Q. Wang, P. Moin, and G. Iaccarino. Minimal repetition dynamic checkpointing algorithm for unsteady adjoint calculation. *SIAM Journal on Scientific Computing*, 31:2549–2567, 2009. doi:`10.1137/080727890`.

[89] M. Wei. *Jet Noise Control by Adjoint-Based Optimization*. PhD thesis, University of Illinois at Urbana–Champaign, 2004.

[90] M. Wei and J. B. Freund. A noise-controlled free shear flow. *Journal of Fluid Mechanics*, 546:123–152, 2006. doi:`10.1017/S0022112005007093`.

[91] N. Yamaleev, B. Diskin, and E. Nielsen. Adjoint-based methodology for time-dependent optimization. In *12th AIAA/ISSMO Multidisciplinary Analysis and Optimization Conference*, 2008. doi:`10.2514/6.2008-5857`.

[92] X. Zhong. High-order finite-difference schemes for numerical simulation of hypersonic boundary-layer transition. *Journal of Computational Physics*, 144:662–709, 1998. doi:`10.1006/jcph.1998.6010`.